

Analysis and Modelling of TTL ice crystals based on in-situ light scattering patterns

by

Elizabeth Reeja Mathen

Submitted to the University of Hertfordshire in partial fulfilment of
the requirement of the degree of PhD

July 2023

Abstract

Even though there are numerous studies on cirrus clouds and its influence on climate, lack of detailed information on its microphysical properties like ice crystal geometry, still exists. Challenges like instrumental limitations and scarcity of observational data could be the reasons behind it. But this knowledge gap has only heightened the error in climate model predictions. Therefore, this study is focused on the Tropical Tropopause Layer (TTL), where cirrus clouds can be seen, and the temperature bias is higher. Since the shape and surface geometry of ice crystals greatly influence the temperature, a detailed understanding of these ice crystals is necessary. So, this paper will look in-depth on finding the morphology of different types of ice crystals in the TTL.

The primary objective of this research is to analyse the scattering patterns of ice crystals in the TTL cirrus and find their characteristics like shape and size distributions. As cirrus is a high cloud, it plays a crucial role in the Earth-atmosphere radiation balance and by knowing the scattering properties of ice crystals, their impact on the radiative balance can be estimated. This research further helps to broaden the understanding of the general scattering properties of TTL ice crystals, to support climate modelling and contribute towards more accurate climate prediction.

An investigation into the light scattering data is presented. The data consist of 2D scattering patterns of ice crystals of size 1-100 μm captured by the Aerosol Ice Interface Transition Spectrometer (AIITS) between the scattering angles 6° and 25° at the wavelength of 532nm. The images were taken during the NERC and NASA Co-ordinated Airborne Studies in the Tropics and Airborne Tropical Tropopause Experiment (known as the CAST-ATTREX campaign) on 5th March 2015 at an altitude between 15-16km over the Eastern Pacific.

The features in the scattering patterns are analysed to identify the crystal habit, as they vary with the geometry of the crystal. After the analysis phase, the model crystals of specific types and sizes are generated using an appropriate computer program. The scattering data of the model crystals are then simulated using a Beam Tracing Model (BTM) based on physical optics, as geometric optics doesn't produce the required information and exact methods (like T-matrix or Discrete Dipole Approximation) are either unsuitable for large size parameters or time-consuming. The simulated scattering pattern of a model crystal is then compared against that of the AIITS to find the characteristics like shape, surface texture and size of the ice crystals. By successive testing and further analysis, the crystal sizes are estimated. Since the manual analysis of scattering patterns is time-consuming, a pilot study on Deep Learning Network has been undertaken to classify the scattering patterns.

Previous studies have shown that there are high concentrations of small ice crystals in TTL cirrus. However, these crystals, especially $<30\mu\text{m}$, are often misclassified due to the limited resolution of the imaging instruments, or even considered as shattered ice. Through this research it was possible to explore both the crystal habit and its surface texture with greater accuracy as the scattering patterns captured by the AIITS are analysed instead of crystal images. It was found that most of the crystals are quasi-spheroidal in shape and that there is indeed an abundance of smaller crystals $<30\mu\text{m}$. It was also found that over a quarter of the crystal population has rough surfaces.

Acknowledgement

I owe my deepest gratitude to my supervisors, Dr Evelyn Hesse, and Dr Richard Greenaway, for their guidance and invaluable supervision throughout this research. I cannot think of better supervisors and without their continuous help, this dissertation would not have been possible.

Also, my special thanks to Dr Chris Stopford for helpful discussions on the AIITS instrument, Dr Anthony J Baran and the OBR group at the Met Office for their insightful comments, Dr Sarah Woods at SPEC Inc and ThaoPaul Bui at NASA for all their support regarding the 2015 ATTREX MMS data.

My appreciation also goes out to my friends.

I would also like to thank my family for their inspiration and unwavering support.

Above all, I am extremely grateful to Almighty God, who enabled me to complete this research.

I would also like to acknowledge the following organisations for the awards:

- ❖ Collaborative Awards in Science and Engineering (CASE): Met Office, UK
- ❖ Bell Burnell Graduate Scholarship Fund (BBGSF): Institute of Physics, UK

CONTENTS

1. Introduction	7
2. Ice crystals, cirrus clouds and light scattering – an overview	9
2.1 Ice crystals	9
2.1.1 Ice crystal habits	10
2.1.2 Orientation of crystals	11
2.2 Cirrus clouds	12
2.2.1 Microphysical properties of cirrus clouds and its impact on climate	14
2.2.2 Previous studies on cirrus clouds	15
2.3 The process of scattering and related terminology	17
2.3.1 Scattering pattern	18
2.3.2 Single scattering and its properties	19
2.3.2.1 Cross-sections and efficiencies	19
2.3.2.2 Single scattering albedo	19
2.3.2.3 Phase function	19
2.3.2.4 Asymmetry Parameter	20
3. Light Scattering Data	21
3.1 Airborne Tropical Tropopause Experiment (ATTREX)	21
3.1.1 ATTREX 2015	23
3.2 Measurement Probes	25
3.2.1 Fast Cloud Droplet Probe (FCDP)	25
3.2.2 Two-Dimensional Stereo (2D-S)	26
3.2.3 Hawkeye	26
3.2.4 Aerosol Ice Interface Transition Spectrometer (AIITS)	27
3.3 Images taken by the CPI	29
4. Methodologies	30
4.1 Terminology	30
4.1.1 Euler angles	30
4.1.2 Aspect Ratio	31
4.1.3 Size Parameter	31
4.2 Features of different types of crystals and their scattering patterns	32
4.3 Methods for simulating light scattering patterns	33
4.3.1 The Beam Tracing Model (BTM)	33
4.4 Estimating the shape and size of crystals	34

4.5 Estimating the size and roughness of rough crystals.....	34
4.5.1 Speckle Analysis.....	35
4.5.1.1 Testing the Speckle Analysis code using simulated scattering images.....	37
4.5.2 Combined Roughness.....	41
4.5.2.1 Grey Level Co-occurrence Matrix (GLCM).....	41
4.6 Dealing with weak images.....	46
5. Modelling different types of crystals to approximate AIITS scattering patterns.....	48
5.1 Plates.....	48
5.1.1 Pristine, smooth hexagonal plates.....	48
5.1.2 Hexagonal plates with rounded edges.....	50
5.1.3 Scalene plates.....	54
5.1.4 Droxtals.....	59
5.2 Columns.....	62
5.2.1 Smooth solid columns.....	62
5.2.2 Rough solid columns.....	63
5.2.3 Needles.....	64
5.3 Quasi-spheroids.....	66
5.4 Rough crystals.....	69
5.4.1 Testing the Speckle Analysis code using AIITS images.....	71
6. Results and Discussion.....	74
6.1 AIITS results from the 2015 ATTREX mission and their interpretation.....	74
6.1.1 Very small crystals.....	74
6.1.2 Columns.....	75
6.1.3 Plates.....	77
6.1.4 Rough crystals.....	79
6.1.5 Quasi-spheroids.....	81
6.2 Imaging parameters which might have affected the particle classification results.....	87
6.3 Results from NASA probes.....	89
6.3.1 Particle size comparison between AIITS and NASA probes' measurements.....	90
6.3.2 Temperature and supersaturation.....	93
6.4 Results from related studies.....	93
7. Pattern classification using Deep Learning Network.....	95
7.1 Deep Learning Network.....	95
7.2 Data pre-processing.....	95
7.3 Network Framework and Training.....	98
7.3.1 Overcoming the data challenge.....	98

7.3.2 Training dataset	98
7.3.3 Designing the Network.....	99
7.4 Assessing the Networks' prediction.....	102
7.4.1 Test dataset	102
7.4.2 The Networks' prediction.....	102
7.5 Testing the trained networks with PPD2 images.....	105
7.6 Discussion of the results	106
8. Conclusions and Future work.....	108
9. Bibliography	112
10. Acronyms	117
11. Appendix	119
11.1 Speckle Analysis.....	119
11.2 Combined Roughness.....	122
11.3 Date Time UTC Conversion.....	124
11.4 Data pre-processing	125
11.5 Deep Learning Network	129
11.6 Poster	133

1. INTRODUCTION

Ice crystals can produce spectacular displays in the sky. Depending on the angle of incident light as well as the geometry and orientation of the ice crystals, these displays vary. Optical phenomena like halos and light pillars are results of refraction and reflection of light through ice crystals.

Clouds can be seen in different levels of the atmosphere – high, middle, or low. Compared to low and middle clouds, high clouds like cirrus varies significantly in terms of their radiative properties due to their position in the atmosphere as well as the complex microphysical properties of ice crystals in them (*Kokhanovsky 2006*). The ice crystals in cirrus clouds vary in shape and size depending on their growth conditions such as temperature and humidity in the atmosphere. Their size ranges from $<10\mu\text{m}$ to many thousands of microns (*Baran 2012*). Cirrus clouds are commonly seen in the upper troposphere and lower stratosphere, a layer called tropopause layer. In the tropics, this layer is known as the tropical tropopause layer (TTL). Studies show that the cirrus cloud coverage is higher in the tropics than in the mid-latitudes (*Baran 2012, Lloyd et al. 2021*). The impact of TTL cirrus on climate is huge and several studies have been conducted to understand their microphysical and macrophysical properties (see Section 2.2.2). The microphysical properties (shape and size distribution etc.) of crystals, play a key role as they can ultimately affect the cloud radiative forcing (*Zhang et al. 1999*). Therefore, it is crucial to know the physical and scattering properties of ice crystals in TTL clouds and by knowing them, radiative transfer and climate model simulations can be done much more accurately.

There are several airborne instruments which are used for imaging ice crystals directly and indirectly. Direct imaging simply means taking images of a crystal directly, while the detection of light scattered by a crystal is called indirect imaging. The primary advantage of indirect imaging is that it can be used for imaging small crystals. Small crystals $<100\mu\text{m}$, due to their size, are often not classified accurately by direct imaging instruments, limited by their resolving power. Also, it is hard to predict whether the crystal surface is smooth or rough by analysing their direct images.

In this research, properties of individual ice crystals in 1-100 μm size range are investigated by analysing their scattering patterns. This helps not only to classify the crystal habits, but also to identify their surface texture. Different types of crystals exhibit different properties in their scattering patterns. The scattering pattern will often contain prominent features like speckles, rings, arcs, or bands (maxima and minima) resulting from constructive and destructive interference. The pattern depends on the wavelength of the incident light as well as the geometry (shape, surface roughness and orientation) and refractive index of the particle. For example, the scattering pattern obtained from a pristine plate crystal differs from that of a scalene plate crystal in many ways (see Section 5.1). By successive testing and closely studying these features, the crystal sizes and shapes can be estimated.

In Chapter 2, the properties of ice crystals like their structure, habits, and orientation are discussed, followed by the types of cirrus clouds and the importance of understanding their microphysical properties as well as previous studies conducted in them. In the later sections, the scattering process and related terminology are briefly described.

This study is focusing on a database of 2D light scattering images taken by the Aerosol Ice Interface Transition Spectrometer (AIITS) at the wavelength of 532nm over the angular range of 6°-25°. These images were taken during the NERC and NASA Co-ordinated Airborne Studies in the Tropics and Airborne Tropical Tropopause Experiment (known as the CAST-ATTREX campaign) on 5th March 2015. Details of the ATTREX mission as well as some of the instruments used for the mission are discussed in Chapter 3.

Since the data are indirect images of crystals, an investigation is needed to identify the crystal shapes and sizes. This is done using a combination of analysis and computer modelling techniques detailed in Chapter 4. On analysing the features in the scattering pattern, it is possible to identify the general shape of the crystal, as the features vary depending on the geometry (and surface texture) of the crystal. Additional steps are followed to accurately estimate the shape, size, and surface texture of the crystals. Once the crystal habit is found, a model of that crystal is generated using a specific algorithm and its scattering pattern is simulated using a technique called the Beam Tracing Model (*Taylor 2016, Hesse et al. 2018*). Investigations are carried out using crystal models of different sizes and orientations until the scattering pattern matches with the AIITS images. If the AIITS images only contain speckle-like features indicating rough crystals, the crystal habit identification is not possible. The size and roughness of rough crystals are calculated using two different computer programmes. The features of different types of crystals and their scattering patterns as well as the process of estimating the shapes, sizes and roughness of crystals are described in Chapter 4. The simulated scattering patterns of different types of modelled crystals compared to the AIITS images are detailed in Chapter 5 using a variety of examples.

The findings of the current investigation are summarized in Chapter 6. These are also compared with the results from other NASA probes during the same flight as well as results from previous studies conducted in TTL cirrus clouds.

Finally, a pilot study on a Deep Learning neural network that helps to classify the crystals based on the scattering pattern is discussed. To speed up the process, the Transfer Learning method is implemented using two pre-trained networks (GoogLeNet and ResNet-50) for image classification and their prediction accuracies are analysed. Transfer Learning is particularly useful when limited data is available. Another advantage of using a pre-trained network is that the network can transfer the knowledge it gained from a larger dataset it has been trained with, to the new smaller dataset. This reduces the training time and the need to design a network from scratch. By replacing the final few layers of the pre-trained network, it can be used alongside the new dataset.

As with all neural networks, the first step is data pre-processing. This process is described in detail in Chapter 7. The pre-trained networks are then trained with a limited number of AIITS images belonging to five categories (Blank images, Columns, Patterned, Plates, and Rounded) as this is a pilot study. There are two versions of the program: one for testing individual images and another for testing a folder of images. In the first version, on testing a single image, the probability of the crystal type is predicted in the form of a bar chart in descending order. In the second, the probability of the crystal type is predicted based on a folder of test images and the predictions with highest score (probability) are written to a file. The first program will be useful for individual inspection of images and predictions, while the second one is aimed at an image database for a faster comparison of results and for checking the overall prediction accuracies of the networks. In addition, to check the usability of the trained networks on light scattering images taken by other instruments, images from the Particle Phase Discriminator version 2 (PPD2) are used as another test set. Finally, the prediction accuracies of both GoogLeNet and ResNet-50 are evaluated based on two test datasets.

2. ICE CRYSTALS, CIRRUS CLOUDS AND LIGHT SCATTERING – AN OVERVIEW

2.1 Ice crystals

Ice crystals are simply water in a solid state. At visible wavelengths, ice appears transparent in its purest form and somewhat opaque in the presence of impurities like tiny air bubbles or dust particles. Ice crystals are formed by homogeneous or heterogeneous nucleation. While the former occurs below -38°C (Atlas *et al.* 2022), the latter, which is observed frequently (Carslaw 2009), occurs below 0°C . Homogeneous nucleation refers to the spontaneous freezing of liquid water, and heterogeneous nucleation refers to the nucleation process involving an ice nucleating particle like mineral dust, volcanic ash, pollen, soot etc. In heterogeneous nucleation, the nucleating particle usually has a crystal lattice structure that closely resembles that of ice.

Depending on temperature and pressure, ice can take on different crystalline structures. Among them, the most common types are hexagonal ice (I_h) and cubic ice (I_c), both having a structure of tessellating hexagonal rings of oxygen atoms linked by hydrogen bonds. The two types differ on how their layers are stacked. Fig. 2.1 (a) shows a layer of water ice with red spheres representing oxygen atoms connected by hydrogen bonds (hydrogen atoms are omitted for clarity). Fig. 2.1 (b) shows hexagonal ice (I_h) with the same layer format repeating in successive layers, while in cubic ice (I_c) Fig. 2.1 (c), the successive layers are displaced by half the diameter of the hexagonal ring in the previous layer. A possible structure of a combination of hexagonal ice (I_h) and cubic ice (I_c) termed as ‘stacking disordered ice’ (I_{sd}) is shown in Fig. 2.1 (d) (Murray *et al.* 2015).

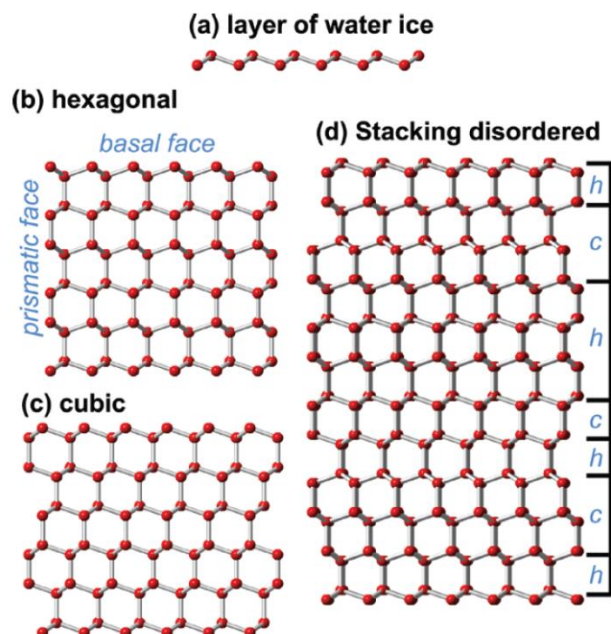


Fig. 2.1: Different crystal structures of ice; (a) layer of water ice, (b) hexagonal ice, (c) cubic ice and (d) stacking disordered ice. Taken from Murray *et al.* (2015).

2.1.1 Ice crystal habits

The shape of the ice crystal varies from pristine hexagonal prism (2 basal and 6 prism facets) to complex structures. Both the crystal shape and its growth are very much determined by the temperature and ice supersaturation. Nevertheless, the underlying crystal structure can also determine the crystal's shape (Murray *et al.* 2015). For example, hexagonal plates and columns are likely to originate from hexagonal ice (I_h), cubes, octahedra and cubo-octahedra from cubic ice (I_c), and trigonal crystals from 'stacking disordered ice' (I_{sd}) (Murray *et al.* 2015).

"The ice elements formed in natural clouds are of three main types: individual ice crystals (or groups of crystals having a common nucleus), snowflakes and hailstones." (Mason and Ludlam 1951). There are 80 types of snow crystals based on meteorological classification (Lee and Magono 1966); a further improvement from 36 types based on Nakaya's general classification of snow crystals. Though widely used, the authors of Kikuchi *et al.* (2013) point out that these classifications are based on observations in Japan and do not include observations from polar regions. The new classification system, named 'global classification', is based on observations from several sites in Japan as well as northern and southern hemisphere polar regions. It presents 121 types of snow crystals, ice crystals and solid precipitation particles with microscope images and schematic drawings alongside their characteristics. The solid precipitation particles include sleet, hail, and ice pellets (Kikuchi *et al.* 2013).

Bailey and Hallett (2009) provide a comprehensive habit diagram as a function of temperature and ice supersaturation, which is shown in Fig. 2.2. The figure consists of both textual (top) and pictorial format (bottom) of ice crystal habits formed between 0°-70°C, based on field studies and laboratory results.

In general, single crystals dominate above -20°C, while polycrystalline structures dominate between -20°C and -70°C. Among the latter, a plate-like regime is evident from -20°C to -40°C and column-like regime between -40° and -70°C. Most of the thin columns can be seen between -10°C and 0°C below 30% ice supersaturation. Most of the simple hexagonal crystals are found at low ice supersaturation and crystal complexity increases with supersaturation. Stellar crystals or dendrites are formed at a temperature range of -8°C and -18°C. On the other hand, bullet rosettes can be seen at temperatures below -40°C at higher supersaturation values. At lower saturation (below 10%), small crystals of size <50 µm can be seen (Bailey and Hallett 2009).

Mason and Ludlam (1951) state that *"...skeletal or dendritic crystals forms are the consequence of high ice-supersaturations, while complete crystals of simple geometrical shape are produced at low supersaturations"*. This agrees with Fig. 2.2, where dendritic crystals are found at between 20-60% ice supersaturation and hexagonal crystals at below 10% ice supersaturation.

Depending on temperature and ice supersaturation, the crystal habit can shift substantially due to their fall in the atmosphere. However, the history of nucleation and changing growth conditions will be preserved in the crystal (Bailey and Hallett 2009). Regarding symmetry and surface texture, ice crystals may not always be perfect. Bailey and Hallett (2009) state that *"most ice crystals are defective and irregular in shape to varying degrees and are mostly polycrystalline at temperatures below -20°C... (the) vast majority of ice crystals are defective in shape with rough surfaces."*

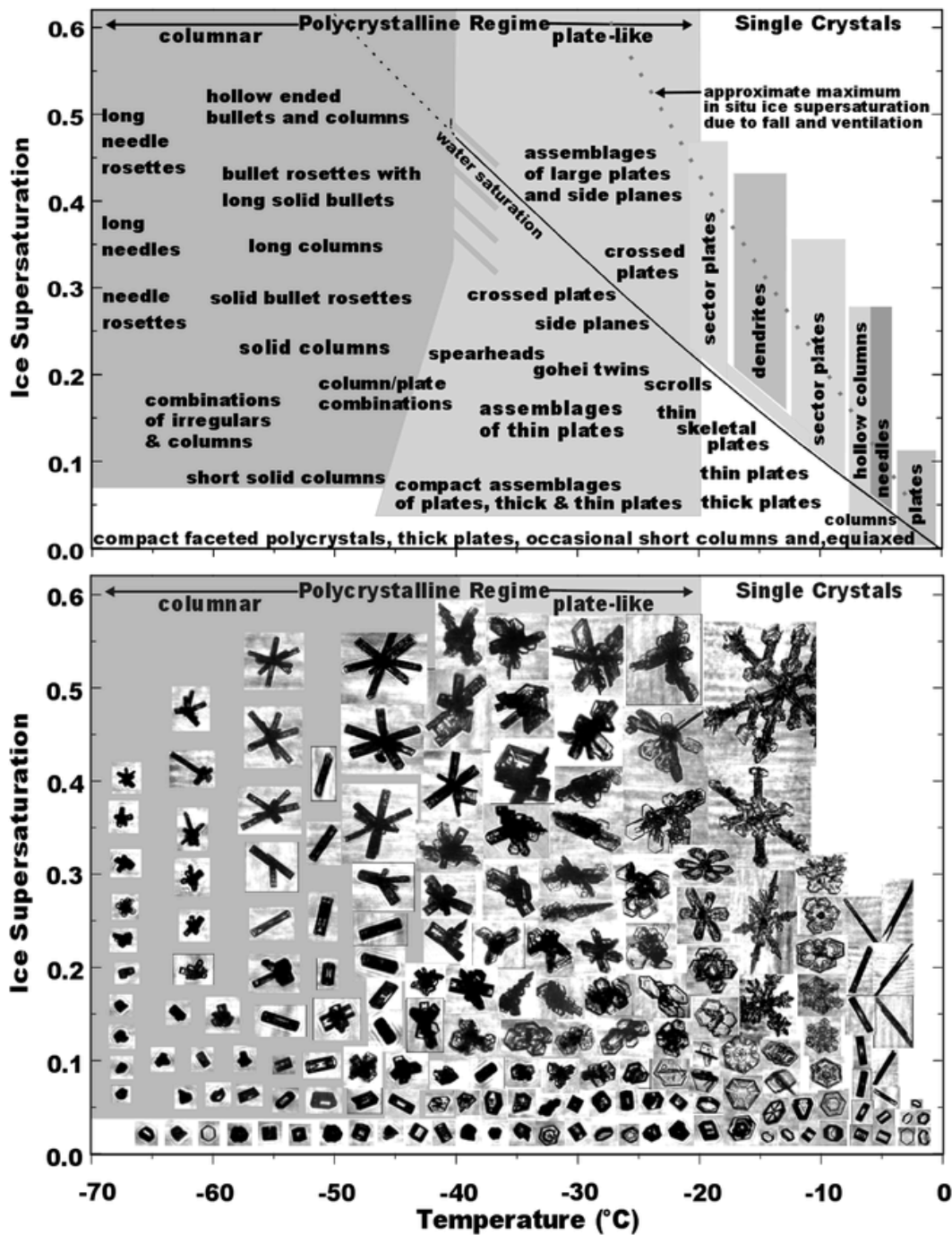


Fig. 2.2: Habit diagram for atmospheric ice crystals in text (above) and in pictorial format (below), taken from Bailey and Hallett (2009).

2.1.2 Orientation of crystals

In an ice cloud, ice crystals can be seen in different orientations. However, the orientation of the crystal depends largely on its geometry, or more simply, keeping its largest surface area horizontal. For example, planar crystals like columns and plates are usually found orienting horizontally. More specifically, hexagonal columns are usually found horizontally oriented along its column axis, while plates are often seen lying on their basal facet. The preferred orientation is due to the atmospheric drag force. The larger the surface area of the crystal, the larger the drag force will be. Based on a study (Noel and Sassen 2005) conducted in cold cirrus cloud to investigate the orientation of ice crystals using LIDAR (Light Detection and

Ranging) observations, 81.5% crystals were found below 1.75° to the orientation angle. About 11.5 % of the crystals were between 1.75 - 3° , and 7% of the crystals above 3° to the orientation angle. Therefore, it was estimated that the high-level cold clouds ($< -30^\circ\text{C}$) have a maximum deviation angle of $\sim 1.0^\circ$ (Noel and Sassen 2005). Other studies (Chepfer et al. 1999, Westbrook et al. 2010) also confirm that planar crystals are found to be horizontally oriented.

2.2 Cirrus clouds

Clouds are made of minute particles of liquid water, ice crystals, or both. They may also contain ice nucleating particles or aerosols. Ranging from puffy cumulus to colourful noctilucent, clouds are divided into different types depending on their appearance (shape, texture etc.), and the atmospheric level at which they occur. Though clouds can be seen at all levels of the atmosphere, most of them are found in the lowest layer of the atmosphere called the troposphere (up to 10km from Earth's surface), where the majority of the dust particles and water vapour are present.

High clouds, which are entirely composed of ice crystals are called cirrus clouds. They have a white, thin, and wispy appearance with a mean optical depth of 0.31 ± 0.24 (Giannakaki et al. 2007). An example is shown in Fig. 2.3. Even though previous studies (Kramer et al. 1999) show that homogeneous nucleation is the main nucleation mechanism due to low temperature, later studies (O'Shea et al. 2016) show evidence for both heterogeneous and homogeneous nucleation of ice particles in cirrus clouds. They are also formed as a result of contrails left behind by aeroplanes, known as contrail cirrus (Karcher 2018). For high clouds like cirrus, cirrostratus, and cirrocumulus, (sometimes referred as cirriform clouds collectively), the typical height of the cloud base above the Earth's surface is 5-13km and 6-18km in the temperate and tropical regions respectively (Houze 2014).



Fig. 2.3: Cirrus cloud seen across the sky over Hertfordshire, U.K., along with contrails.

The cirrus cloud can be further divided into different types. Cirrus spissatus (translates to 'thick' in Latin) is the thickest cirrus cloud which can be seen in the upper troposphere. An example,

taken from St. Brelade, Jersey can be seen in Fig. 2.4 (a). Another cirrus cloud type known as cirrus floccus can also be seen in its initial stage of development (see inset of Fig. 2.4 (a), *CloudAtlas 2017*). Houze (2014) suggests that as the cloud ages, the hair-like appearance of cirrus clouds will become more exaggerated. Fig. 2.4 (b-d), taken from Colorado, shows this aging process (Houze 2014). In Fig. 2.4 (b), cirrus floccus with wool-like patches can be seen. In a more advanced stage of development, cirrus uncinus can be seen in Fig. 2.4 (c), which can be easily distinguished by its unique hook shape (uncinus means ‘curly hooks’ in Latin). Later, in the most advanced state, cirrus fibrates are formed with parallel streaks without any hook. Fig. 2.4 (d) shows a special kind of cirrus fibrates known as ‘cirrus fibrates vertebratus’ with a distinct fish bone-like look.

Clouds, in general, play a very important role in climate. “Changes in cloud cover are important because clouds exert a strong control over Earth’s radiative balance (Carslaw et al. 2002). They can make the Earth’s atmosphere cooler or warmer by reflecting or absorbing the sunlight. According to the report by the Intergovernmental Panel on Climate Change, “Clouds and aerosols continue to contribute the largest uncertainty to estimates and interpretations of the Earth’s changing energy budget” (Boucher et al. 2013). Cirrus clouds, in particular, have been a topic of interest for many researchers. Results from space-based measurements show that at any given time, cirrus covers about 30% of the mid-latitudes, and 60%–80% of the tropics (Baran 2012). Relatively higher cloud fractions were found in tropical regions compared to mid-latitudes (Lloyd et al. 2021).

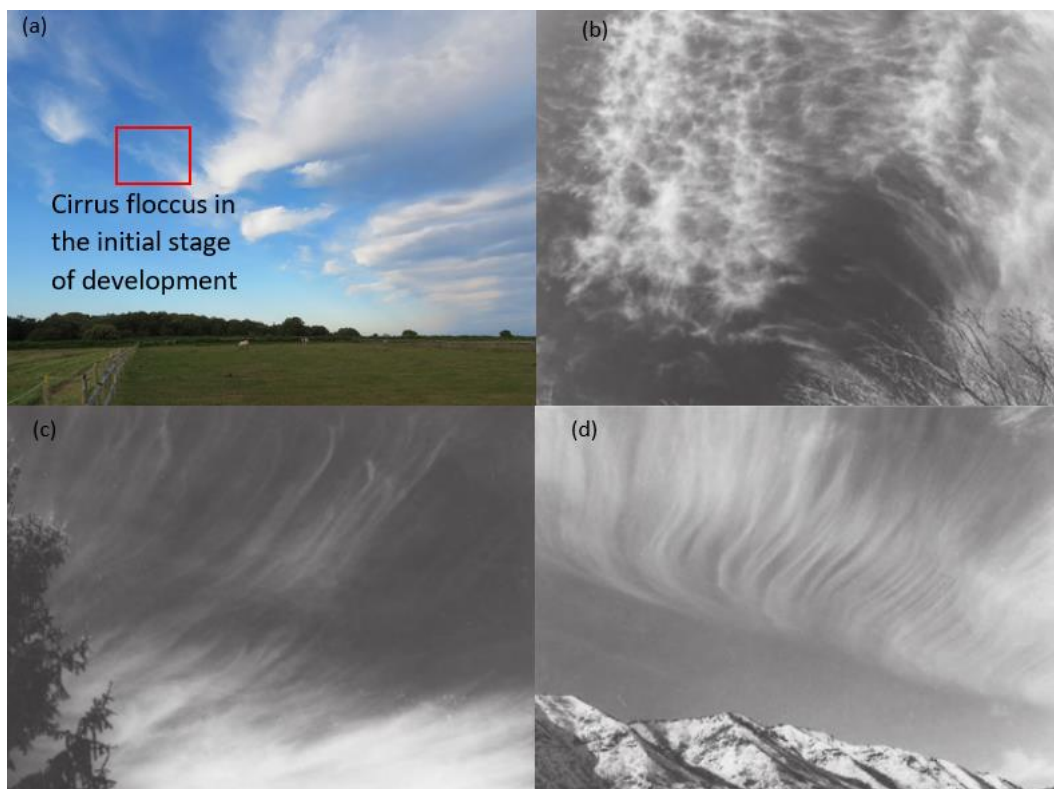


Fig. 2.4: Different types of cirrus clouds. (a) Cirrus spissatus (taken from *CloudAtlas (2017)*); the highlighted area shows the cirrus floccus in its initial development stage. (b) Cirrus floccus, (c) cirrus uncinus, and (d) cirrus fibrates vertebratus. Images (b-d) are taken from Houze (2014).

2.2.1 Microphysical properties of cirrus clouds and its impact on climate

Inconsistencies still exist in climate modelling due to spatial and temporal variations of cirrus clouds and differences in their microphysical parameters (Baran 2012, Zhang et al. 1999). Limitations of imaging instruments in capturing their exact properties, scarcity of satellite as well as in situ measurements are other contributing factors to such inconsistencies (Jensen and Pfister 2004, Karcher 2018). Several authors (Strom et al. 1997, Noel and Sassen 2005, Murray et.al 2015) have pointed out the shortage of information about the microphysical properties of cirrus clouds which results in uncertainty of their effect on the radiative balance and ultimately, in modelling climate. *“The radiative impact of cirrus clouds is one of the largest sources of uncertainty in global climate models (GCMs) due to the complex microphysical processes that are poorly understood and difficult to measure”* (Lloyd et al. 2021).

Cirrus clouds can be seen primarily in the tropopause layer, a transition layer which separates the dry stratosphere from the wet troposphere. It extends between ~10-12km at high altitudes and 14-18km in the tropics (Houze 2014). Within the tropopause layer temperature stays almost constant. Between the Earth’s surface and the tropopause layer temperature decreases with height and above the tropopause layer, the temperature increases with height (temperature inversion). In the tropics, this layer is known as Tropical Tropopause Layer (TTL). Many authors (Baran 2012, Thornberry et al. 2017) claim that the TTL cirrus act as a crucial layer in the atmosphere by contributing to thermal radiation and temperature biases. *“The role of thin cirrus clouds for cloud feedback is not known and remains a source of possible systematic bias...Feedbacks from thin cirrus amount cannot be ruled out and are an important source of uncertainty”* (Boucher et al. 2013).

Cirrus clouds can absorb the thermal infrared radiation emitted from the Earth’s surface and lower atmosphere and at the same time, they can reflect the incoming sunlight (Kokhanovsky 2006). Depending on the amount of radiation it absorbs and reflects, the net energy varies. *“Understanding the role of cirrus clouds in this [radiative energy budget] system is vital, as they interact with short- and long-wave radiation, and the presence of cirrus can be decisive as to a net gain or loss of radiative energy in the [polar] atmosphere”* (Marsing et al. 2023). The net radiative effect of cirrus cloud is defined as the sum of the short-wave radiation and long-wave radiation (Baran 2012).

$$R_{net} = R_{SW} + R_{LW} \quad (2.1)$$

where R_{net} is the net radiation (irradiance, unit: W/m²), R_{SW} is the short-wave radiation and R_{LW} is the long-wave radiation. The short-wave radiation is the difference between the short-wave irradiance from cirrus ($R_{SW(cirrus)}$) and cloud-free sky ($R_{SW(cloud_free)}$). Similarly, the long-wave radiation is the difference between the long-wave irradiance from the cirrus ($R_{LW(cirrus)}$) and cloud-free sky ($R_{LW(cloud_free)}$).

$$R_{SW} = R_{SW(cirrus)} - R_{SW(cloud_free)} \quad (2.2)$$

$$R_{LW} = R_{LW(cirrus)} - R_{LW(cloud_free)} \quad (2.3)$$

The net radiative effect can be positive, negative, or neutral depending on ice crystal shape and size distribution along with other parameters (optical depth, ice water content, altitude etc.) of the cirrus cloud (Baran 2012). For example, in terms of crystal habit, a cloud containing spherical crystals has higher radiative forcing compared to one with aspherical or polycrystals (aspherical crystals have higher reflective (albedo) properties) (Zhang et al. 1999). In terms of crystal size, large ice crystals produce positive cloud radiative forcing (and thereby warming effect on Earth-atmosphere system); on the other hand, a large number of smaller crystals can create the opposite effect (Zhang et al. 1999). The authors also state that *“Cirrus cloud radiative forcing, which reflects the potential climate impact of cirrus, is extremely sensitive to crystal shape and to crystal size distribution.”* Other studies (Wendisch et al. 2005 and 2007) also confirm that ice crystal shape can significantly affect long-wave radiation.

Small particle size with low fall speed (the rate at which crystals fall down in the atmosphere due to gravity) is one of the reasons for longer cloud persistence in the TTL (Fueglistaler et al. 2009). “The small particles may make an important contribution for the radiative transfer in clouds and should not be neglected” (Wyser 1998). In the next section, the importance of studying small crystals is described, based on the previous studies conducted in the cirrus clouds.

2.2.2 Previous studies on cirrus clouds

Over the years, various studies of the microphysics of cirrus clouds have demonstrated the prevalence of small ice (<100 μm). However, there are uncertainties concerning their morphology (Baran 2012).

In a study, based on a series of in-situ measurements over several states in the U.S., a higher concentration of smaller sized crystals was found. The particle size distributions measured in and near cirrus clouds using optical array probes can be seen in Fig. 2.5 (Heymsfield 1975). The temperature varied between -19°C and -58°C during sampling. From Fig. 2.5, it is evident that the particle spectra are roughly the same for two types of cirrus, cirrus uncinus and cirrostratus up to crystal size of 100 μm . The particle concentration is high in the size range 10-100 μm . Then it reduces gradually for cirrostratus; while for cirrus uncinus, it peaks again at 500 μm .

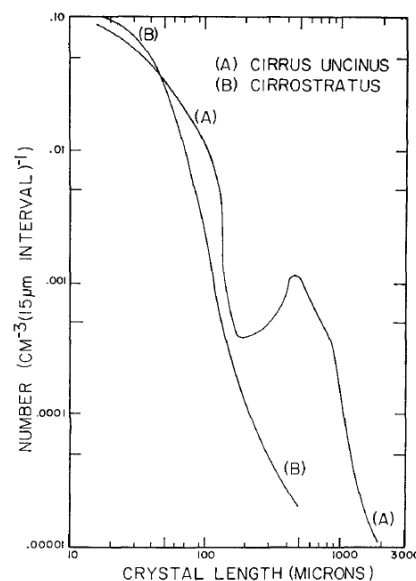


Fig. 2.5: The particle size distributions measured in cirrus clouds, taken from Heymsfield (1975). Two types of cirrus clouds were sampled: cirrus uncinus (A) and cirrostratus (B).

Regarding a series of measurements to analyse the distribution and mass concentration of ice in cirrus clouds using an airborne optical ice particle counter, Liou (1986) states that “The crystal shapes associated with cirrostratus, cirrocumulus and cirrus were found to be columns, plates and bullets with sizes ranging from about 100 to 1000 μm . It is noted that many crystals with sizes smaller than 100 μm may be missed by the sampling techniques.”

NASA has also conducted several studies of cirrus clouds over the years. The objective of one such study, the 2014 Airborne Tropical Tropopause Experiment (ATTREX), was to investigate the composition, humidity, and thermal structure of TTL cirrus (Jensen et al. 2019). (Note that this investigation is also part of ATTREX but focused on 2015 ATTREX.) Details of the instruments and ATTREX mission are given in Chapter 3. Fig. 2.6 shows the mean size

distribution of crystals sampled on 9-10 March over Western Pacific (the fifth flight out of six flight samplings) along with their CPI (Cloud Particle Imager) images. The size distributions are shown for two temperature ranges. From the CPI images, the abundance of smaller crystals at lower temperature ($T < 195\text{K} = -78^\circ\text{C}$) can be seen. In comparison, larger crystals are evident at the higher temperature range of $195\text{--}210\text{K}$ ($= -78$ to -63°C). In general, the smaller crystals look quasi-spheroidal (except a few plates, columns, and bullets), but it is difficult to identify the actual crystal shape from the image. In terms of crystal size, the distribution peaks can be seen at crystal sizes $< 30\mu\text{m}$. This data is from just one of 6 flight sampling results; nevertheless, the results from the other flights corroborate the abundance of small crystals $< 30\mu\text{m}$ (Woods et al. 2018).

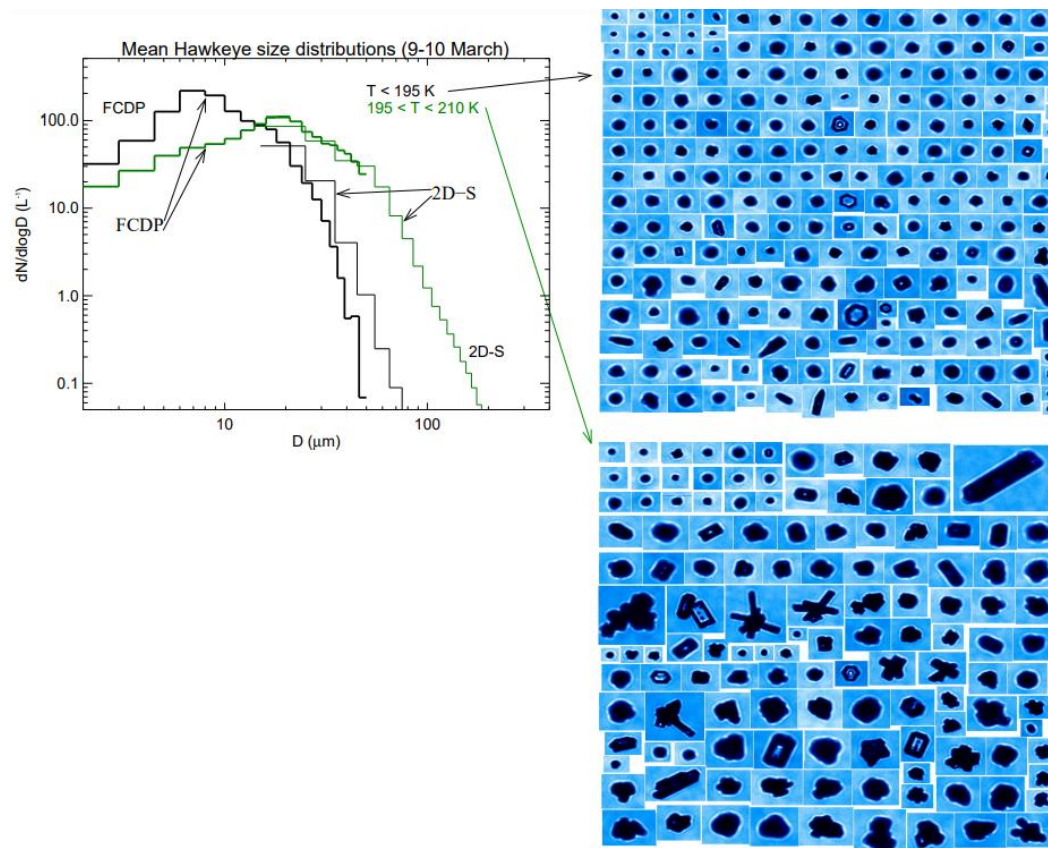


Fig. 2.6: The mean size distribution of crystals (provided by FCDP and 2D-S probes) and the crystal images captured by the CPI during the flight on 9-10 March as part of the 2014 ATTREX campaign. Image reproduced from Jensen et al. (2019). The two CPI image panels (right) correspond to temperature $< 195\text{K}$ (top) and between $195\text{--}210\text{K}$ (bottom).

Similar results were found during a mission to study the microphysical properties of midlatitude cirrus clouds where temperature ranged between -28°C and -61°C . The particle distribution peaked in number concentration near $30\mu\text{m}$; 99% of the total number concentration were accounted by particles $< 50\mu\text{m}$ (Lawson et al. 2006b). Among these measurements, two flights were through thin cirrus clouds and no particles $> 100\mu\text{m}$ were observed. The dominance of small crystals might be explained by ice shattering, but the authors consider this phenomenon to have only a partial effect on the counts. “Thus, the data suggest that, while crystal shattering may inflate the number of small particles in some cirrus clouds, there are instances where crystal shattering is highly unlikely and very high concentrations of small particles are still observed” (Lawson et al. 2006b).

In another study, cirrus clouds were sampled by an aircraft off the UK coast, to the northeast (altitude 6500 to 8500 m) and north (altitude 6000 to 9000 m), on 11th and 13th March 2015 respectively (O'Shea et al. 2016). During the former flight, the temperature ranged between 230 and 239 K with a cloud top temperature of 220K. During the latter, it was 226 to 245 K with a cloud top temperature of 226K. It is reported that *“For both flights the highest concentrations of small ice (less than 100µm in size) are observed at the lowest temperatures suggesting that this is where most of the ice nucleation is occurring”* (O'Shea et al. 2016).

In addition to the studies mentioned above, a novel imaging remote sensing method was used during a recent study (Forster and Mayer 2022) on retrieving ice crystal properties in cirrus cloud. It was based on ground-based imaging observations of halo displays and they found that 90% of the crystals had an effective radius (measure for mean size in particle population) of <40µm. The process of retrieval of ice crystal properties is as follows: The image database consists of images taken by the HaloCam. An automated HaloForest algorithm validates the images with 22° halos. The images are centred around specific azimuth angles. The best match is found based on the radiance measurement of the ground-based HaloCam RGB image and the precomputed radiance distribution in the look up table in the scattering angle range of 18-25°. The look up table consists of different parameters like ice crystal habits, surface roughness values, effective radii, cirrus optical thickness etc. The ice crystal properties of the best match are then retrieved. In addition, they also check for the presence of the 46° halo, to further differentiate the crystals. Though the light shed by the study on the crystal size is valuable, it is worth noting that, since it was focused on halo producing crystals (usually faceted crystals), other crystals (like quasi-spheroids, which are incapable of producing halos) were excluded from the study.

Despite all these studies, there is ambiguity around small sized crystals as to whether they are actual crystals or just artifacts resulting from the partial observation of out-of-focus larger particles (O'Shea et al. 2016). They are also often considered as shattered ice (O'Shea et al. 2016, Guignard et al. 2012), misclassified or generalized as quasi-spheroids (Bailey and Hallett 2009, Woods et al. 2018), missed by the detecting instruments (Liou 1986), or even excluded from the dataset due to pixel inadequacy (O'Shea et al. 2016). *“The presence or absence of such small particles has important implications for understanding cirrus cloud microphysics and radiative properties, and so further investigation of this issue is crucial to further progress”* (O'Shea et al. 2016).

It is clear from these studies that a detailed knowledge of small ice crystal (<100µm) properties is required to characterise cirrus more effectively, permitting the development of more accurate radiative transfer and climate model simulations. The current study is specifically focused on this range and provides just such an insight into these properties. Since this investigation is based on analysing the 2D light scattering patterns captured by the AITS, the method is not affected by the resolution limit imposed by direct imaging. Additionally, the surface texture can also be analysed accurately. Scattering images however mean that, the properties of ice crystals can only be found by solving the indirect problem using a combination of observational data analysis and computer modelling techniques.

Before proceeding any further, the scattering process and related terminologies are discussed.

2.3 The process of scattering and related terminology

Consider a particle which is subdivided into smaller regions. Light, an electromagnetic wave, can induce a dipole moment in each of these regions and set the dipoles to oscillate at the frequency of the applied field. As a result, they radiate energy in all directions known as scattered wave. At any point P, the total scattered field will be the sum of all the scattered

wavelets (Bohren and Huffman 1998). Fig. 2.7 provides a pictorial representation of this process.

Not all the incident waves will be re-radiated as a scattered wave. A portion of the incident energy could be ‘absorbed’ by the particle depending on the absorption coefficient of the medium. As a result of scattering and absorption, the incident wave will be attenuated, which is commonly referred as ‘extinction’.

$$\text{Extinction} = \text{Scattering} + \text{Absorption}$$

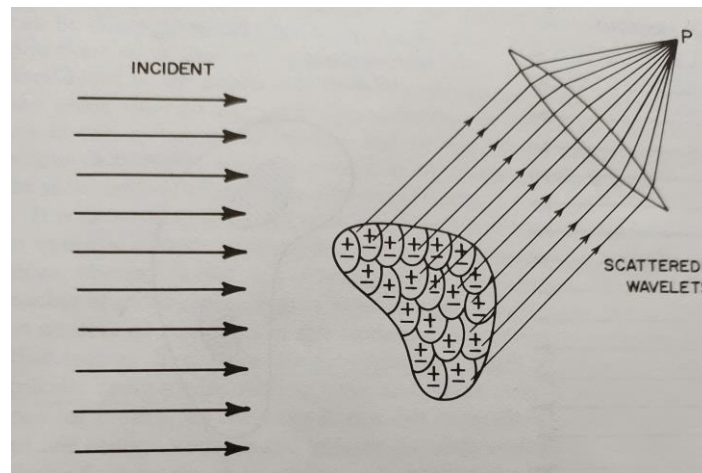


Fig. 2.7: The process of incident light scattered by a particle, taken from Bohren and Huffman (1998).

The light wave incident on a particle can be absorbed, reflected from its surface or refracted through the particle and be scattered in different directions. It is possible to capture part of the angular distribution of the scattered light using instruments like the AITS (described in Section 3.2.4) and by analysing the features of the scattering pattern, the properties of particles can be retrieved. This is termed the **Indirect (inverse) scattering problem**. That is, finding the characteristics (shape, size, and surface) of the particle by analysing its scattering data, which is a challenging problem. The converse is called the **direct scattering problem**, finding the scattered field from a particle of known shape, size, and constituents.

Note that only elastic scattering is considered. That is, the scattered light is assumed to have the same wavelength (or frequency) as the incident light.

2.3.1 Scattering pattern

Scattering patterns help us to study the morphology of ice crystals as the features in the pattern vary depending on the crystal habit. It is a two-dimensional plot of the scattered light represented in polar co-ordinate form (θ, ϕ) , where $0^\circ \leq \theta \leq 180^\circ$ and $0^\circ \leq \phi \leq 360^\circ$. In general, the forward and backward scattering hemisphere gives scattering information between $\theta=0^\circ-90^\circ$ and $\theta=90^\circ-180^\circ$ respectively. In this study, the focus is on the forward scattering information of $6^\circ \leq \theta \leq 25^\circ$, which is the angular range of AITS images. The same range is used while scattering patterns of model crystals are simulated using the Beam Tracing Model (BTM, see Section 4.3.1). The scattering pattern in a linear intensity scale will only illustrate features at high intensity. For this reason, the scattering pattern is plotted in logarithmic scale for a better visualisation of the intricate details, especially at the lower intensity range.

2.3.2 Single scattering and its properties

Single scattering refers to scattering from a single particle. In single scattering, it is assumed that the particles are at large separation from each other, and only the scattered field of the individual particle when excited by an external field is considered. Hence, it is sometimes referred as independent scattering. That is, each particle is treated in complete isolation from the surrounding particles (Bohren and Huffman 1998). Regarding the minimal particle separation for independent scattering, there is no universal rule. While a mutual distance of three times the radius is recommended by Hulst (1957), a distance of four times their radius is suggested by Mishchenko (2000).

Some of the single scattering properties are described below.

2.3.2.1 Cross-sections and efficiencies

The scattering cross section (C_{sca}) can be defined as the ratio of the total power (unit: W) removed from the incident beam due to the light scattering by the particle to the incident irradiance (unit: Wm^{-2}). Similarly, absorption cross section (C_{abs}) can be defined as the ratio of the total power removed from the incident beam due to the absorption of light by the particle to the incident irradiance. Extinction cross section (C_{ext}) accounts for the attenuation resulting from both the scattering and absorption cross sections.

By the law of conservation of energy,

$$C_{ext} = C_{sca} + C_{abs} \quad (2.4)$$

For a non-absorbing particle,

$$C_{ext} = C_{sca}$$

The scattering cross section can also be defined as the product of scattering efficiency (Q_{sca}) and the geometrical projected cross section of the particle. Equation 2.4 can be written in terms of efficiencies as,

$$Q_{ext} = Q_{sca} + Q_{abs}$$

where Q_{ext} and Q_{abs} are extinction and absorption efficiencies respectively. The cross sections have units of area, while efficiencies are dimensionless.

2.3.2.2 Single scattering albedo

The ratio of scattering cross section to extinction cross section is defined as the single scattering albedo.

$$\bar{\omega} = \frac{C_{sca}}{C_{ext}}$$

It provides a measure of how much of the extinction is due to scattering and takes a value between 0 and 1. While $\bar{\omega} = 1$ implies that the extinction is solely due to scattering, $\bar{\omega} = 0$ implies that the extinction is solely due to absorption.

2.3.2.3 Phase function

The angular intensity distribution of light scattered by a particle at a given wavelength is called the phase function. The direction of scattering is characterized by scattering angle (θ) and azimuth angle (ϕ). The scattering angle θ is the angle formed between the incident and

scattered beam directions. The phase function is normalized in such a way that the integral over the scattering sphere centred on the particle is equal to 4π (Sienfeld and Pandis, 1997).

$$\int_{\phi=0}^{\phi=2\pi} \int_{\theta=0}^{\theta=\pi} P_{11}(\theta, \phi) \sin\theta \, d\theta \, d\phi = 4\pi$$

2.3.2.4 Asymmetry Parameter

Asymmetry parameter refers to the intensity-weighted average of the cosine of the scattering angle (θ).

$$g = \langle \cos\theta \rangle = \frac{1}{2} \int_{\theta=0}^{\theta=\pi} P_{11}(\theta) \cos\theta \sin\theta \, d\theta$$

Depending on the direction of the scattered light, the value of g changes between -1 and 1. When $\theta=0^\circ$, the scattered light propagates in the same direction of the incident light (forward scattering and $g=1$). For backward scattering ($\theta=180^\circ$), when the scattered light propagates in a backward direction to the incident light, $g=-1$. When the light is scattered equally in all directions (isotropic), $g=0$.

In this chapter, an overview on ice crystals and cirrus clouds were given. The scattering process and associated terminology were also outlined. Previous studies point out the importance of understanding the microphysical properties of small ice crystals in cirrus cloud and this research is focused on investigating the properties of these ice crystals.

In the next chapters, this paper briefly discusses:

- The light scattering data and instrumentation.
- The features that can be seen in the scattering pattern and how to identify the ice crystal geometry based on those features. The processes of estimating the size of smooth and rough crystals are also described.
- Examples of different types of modelled crystals and their simulated scattering patterns are compared to the AIITS light scattering pattern images.
- The statistics of crystal types and sizes based on analysing the light scattering data taken by AIITS (05 March ATTREX 2015).
- The steps involved in developing a Deep Learning code for future crystal classification.

3. LIGHT SCATTERING DATA

The data used in this research was obtained during the ATTREX (Airborne Tropical Tropopause Experiment) scientific campaign on 5th March 2015. The data, a collection of 2426 indirect images or far-field light scattering patterns, was generated by the AIITS (Aerosol Ice Interface Transition Spectrometer), an instrument designed and built at the University of Hertfordshire. This chapter outlines the ATTREX mission and some of the instruments used during the science flight.

3.1 Airborne Tropical Tropopause Experiment (ATTREX)

The ATTREX was a series of scientific measurement campaigns initiated by NASA (National Aeronautics and Space Administration) to study the physical processes, chemical composition, moisture levels and humidity in the TTL from 2011 to 2015. NASA's Global Hawk (Fig. 3.1), an unmanned aerial vehicle (UAV) was chosen for this project to carry the specialised instruments due to its ability to fly at high altitude (20 km) covering a long range (16000 km) with a payload capacity of around 680 kg (*Jensen et al. 2013*). The ATTREX project was managed by the NASA Ames Earth Science Project Office, along with investigators from NASA, National Oceanic and Atmospheric Administration (NOAA), National Centre for Atmospheric Research (NCAR), several universities as well as private industry (*Conner 2015*).



Fig. 3.1: NASA Global Hawk during a checkout flight of ATTREX instruments (*Baccus 2014*).

Overall, the ATTREX mission provided over 300 hours of TTL sampling (*Jensen et al. 2022*). Brief summaries of the flights, the regions where the experiments were conducted as well as the flight duration when sampling are given in Table 3.1. The flight path taken during different ATTREX missions are shown in Figs. 3.2 and 3.3. The figures have a different range in latitude/longitude. Details of the **2011** and **2013** ATTREX missions are discussed in *Jensen et al. (2013)*.

Year	Flight hours	Sampling Region
2011 (Oct-Nov)	61.3 (3 flights)	Eastern Pacific TTL
2013 (Feb-Mar)	146.6 (6 flights)	Central and Eastern Pacific TTL
2014 (Jan-Mar)	99.9 (6 flights)	Western Pacific TTL
2015 (Jan-Mar)	66 (4 flights)	Central and Eastern Pacific TTL

Table 3.1: ATTREX flights details.

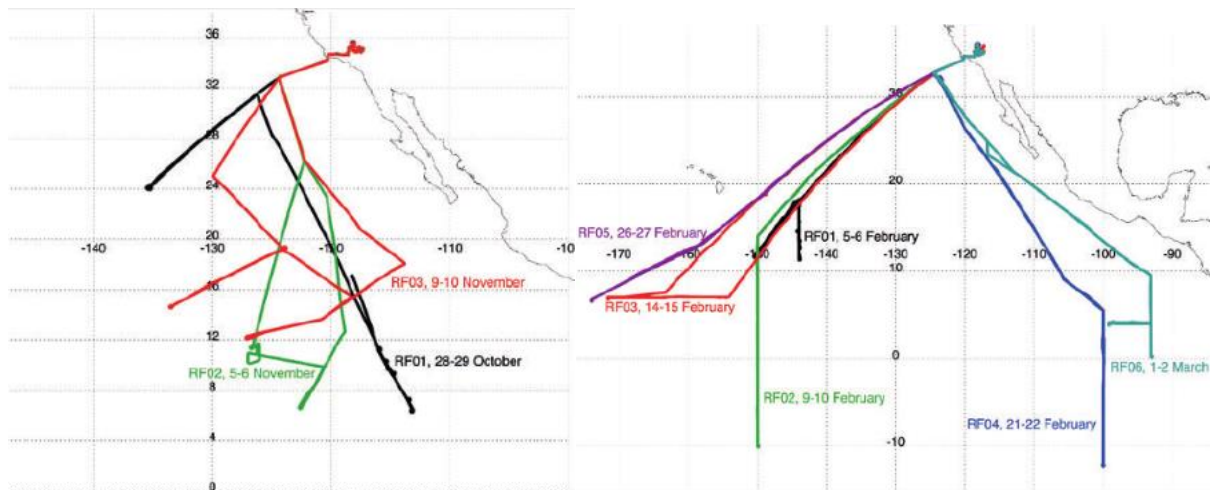


Fig. 3.2: Flight tracks of ATTREX 2011 (left) and 2013 (right) flights (Jensen et al. 2013).

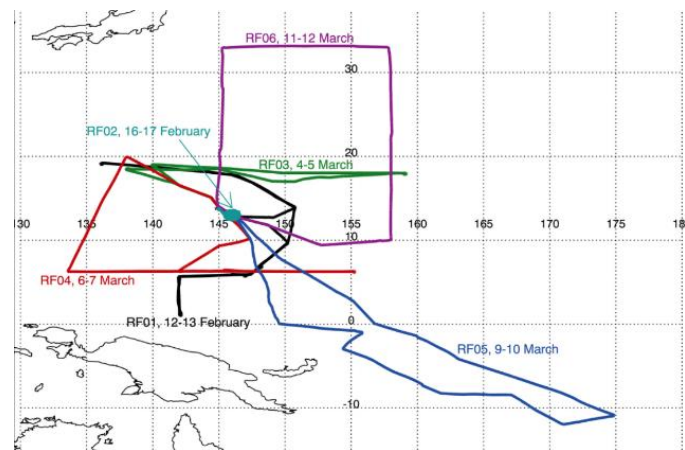


Fig. 3.3: Flight tracks of ATTREX 2014 science flight (Woods et al. 2018).

During the ATTREX 2014 deployment, six research flights were conducted in the Western Pacific. These are shown in six different colours in Fig. 3.3. Fig. 3.4 also shows the ATTREX 2014 flight path, but additionally it shows the occurrence of clouds (coloured by temperature in Kelvin) along the flight track as well as the vertical flight profile. The clouds were sampled at an altitude between 14-18 km and the temperature of the cloud ranged between 185-207 K. Further information on the 2014 ATTREX mission can be found in Thornberry et al. (2017), Jensen et al. (2017) and Woods et al. (2018).

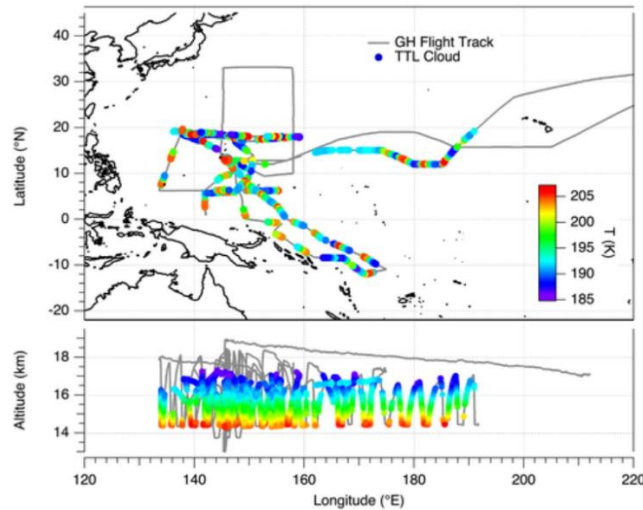


Fig. 3.4: The Global Hawk flight path over the Western Pacific for ATTREX 2014 (top) shown in grey colour. The presence of cloud is shown in rainbow colours with a temperatures scale on right side of the figure. The TTL clouds are shown in dark blue colour. The altitude of clouds (in km) along with the vertical profile of the flight are shown in the bottom panel (Thornberry et al. 2017).

3.1.1 ATTREX 2015

The 2015 ATTREX deployment was NASA ATTREX and CAST (Co-ordinated Airborne Studies in the Tropics, funded by Natural Environmental Research Council (NERC)) joint mission conducting research flights using the Global Hawk. The Global Hawk took off from its base at NASA's Armstrong Flight Research Centre, California, and conducted three research flights between 3rd and 13th March with an average duration of 22 hours totalling 66 hours.



Fig. 3.5: Image of ATTREX 2015 flight tracks superimposed on a 'colorterrain' map. The flight track on 5th March is shown in red. The other flight tracks on 10th March (blue), 2 range flights on 26th Feb (yellow) and 13th March (green), can be seen as well.

Along with the previously flown ATTREX payload, two new CAST probes were used, the AIITS and the Green House gas Observations in the Stratosphere and Troposphere (GHOST) (Conner 2015). More details on AIITS can be found in Section 3.2.4. GHOST is a shortwave-infrared (SWIR) spectrometer which measures the greenhouse gases from an airborne platform (Humpage et al. 2018). The two CAST instruments had conflicting requirements for atmospheric conditions to get optimal results; while AIITS is designed to study cloud particles, GHOST require cloudless skies (Humpage et al. 2018). Therefore, separate flights were targeted for AIITS and GHOST on 5th and 10th March respectively. The flight on the 5th of March (flight track shown in red colour in Fig. 3.5) lasted for a total duration of 25 hours and a large proportion of it consisted of vertical profiling through the TTL clouds.

Fig. 3.6 shows how the static temperature and pressure change as a function of altitude. Pressure is given in units of hecto Pascals (hPa). 1 hPa=100 Pa= 1 millibar. At higher altitudes around 18km, the pressure ranges between 50-100 hPa and the temperature 190-215 K, compared to the surface values 900-950 hPa and 280-290 K respectively.

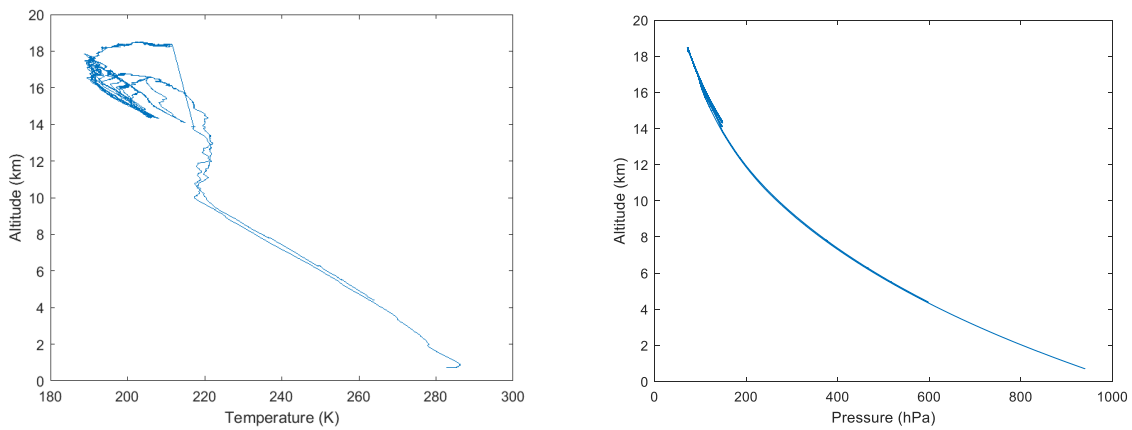


Fig. 3.6: Temperature(left) and Pressure (right) profile.

Temperature and altitude data are shown in Fig. 3.7. The vertical profile of the flight, track shown in blue colour, ranges from 14 to 18 km. The corresponding value of temperature is shown in red colour. Over time, the temperature varied between 190 and 220 K, and as expected, the temperature peaked at around 205K over the area in which the flight descended to 14km.

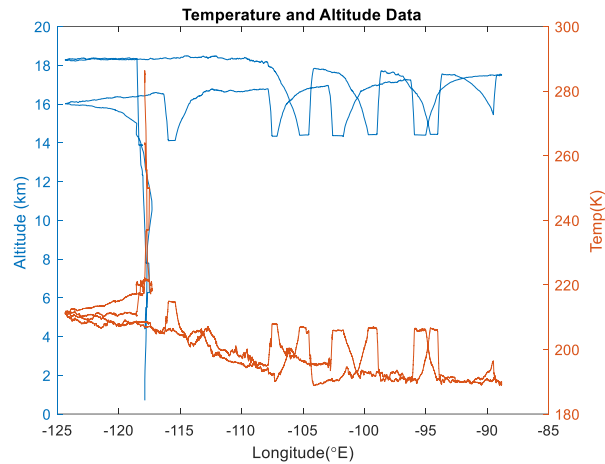


Fig. 3.7: The temperature and altitude data. The blue solid line represents the vertical profile of the flight track, and the red solid line represents the static temperature along the flight track.

3.2 Measurement Probes

Several measurement probes were installed on the aircraft during the ATTREX mission, some of which are briefly described here.

3.2.1 Fast Cloud Droplet Probe (FCDP)

FCDP is an optical particle counter designed to measure cloud particle number and size distributions in 1.5-50 μm diameter range. The probe (see Fig. 3.8) consists of 2 arms with a laser beam on one side (transmitter arm) and the photodetectors on the other (receiver arm). It works on the principle of forward scattering; as the particle passes through the sample volume (between the transmit and receive arm) the light will be scattered and directed through collection lens system, while the detecting optics measures the particle size based on the intensity of scattered light collected at the dump spot. The data acquisition as well as the signal processing systems are kept in the main body (SPECinc 2019). The instrument provides reliable measurement in ice clouds (Jensen et al. 2013). The FCDP, along with the layout of its light scattering measurement principle is shown in Fig. 3.8. Apart from ATTREX, FCDP has also been used in the NASA POSIDON (Pacific Oxidants, Sulphur, Ice, Dehydration, and cONvection) experiment to study the OH and sulphur chemistry, cirrus clouds, and dehydration in the tropical upper troposphere and lower stratosphere over the western Pacific (NASA 2020).

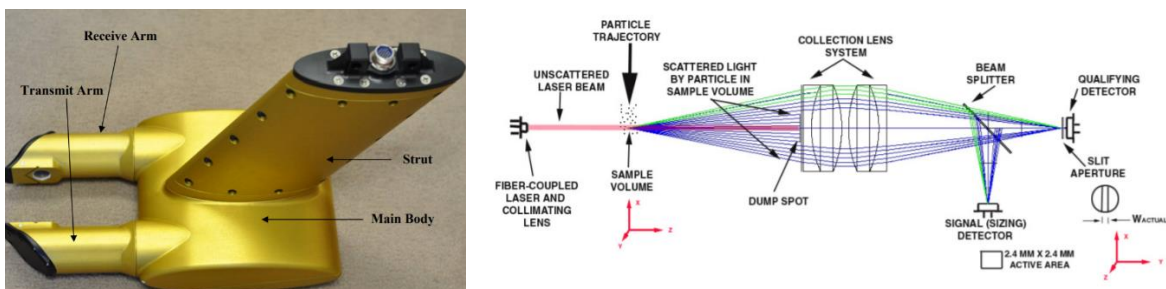


Fig. 3.8: Picture of FCDP (left) (SPECinc 2019) and its light scattering measurement principle (right) (Glienke et al. 2020).

3.2.2 Two-Dimensional Stereo (2D-S)

2D-S is an optical imaging instrument capable of taking shadowgraph images (a photographic image resembling a shadow) of particles with a pixel resolution of $10\mu\text{m}$ at aircraft speeds up to 250 m/s (Lawson *et al.* 2006a). It can measure the particle size between $10\text{-}1280$ microns using two independent $10\ \mu\text{m}$ channels, as well as particle concentration and extinction (NASA 2022). It consists of two linear 128-photodiode arrays illuminated by two diode laser beams perpendicular to each other. The beams are directed through the centre of the sample volume. Since the probe is capable of recording two independent images of the same particle in the beam's overlap region, even a three-dimensional view can be reconstructed for some particles. Single images of particles are captured outside the rectangular overlap region (Lawson *et al.* 2006a). Although replaced by the Hawkeye and 3V-CPI (Three view Cloud Particle Imager, combination of 2D-S and CPI), the instrument is still operational. Fig. 3.9 shows the zoomed in portion of sample volume of the 2D-S as well as the instrument installed on an aircraft.



*Fig. 3.9: Photograph of 2D-S' close-up view of sample volume with orthogonal laser beams (left) and of 2D-S and CPI installed on a research aircraft (right) (Lawson *et al.* 2006a).*

3.2.3 Hawkeye

Hawkeye (see Fig. 3.10) is a particle imager which houses a combination of cloud particle probes: Two channels of 2D-S capable of sizing particles in the $10\text{-}1280\ \mu\text{m}$ and $50\text{-}6400\ \mu\text{m}$ size ranges at $10\mu\text{m}$ and $50\mu\text{m}$ resolution respectively, FCDP with $1.5\text{-}50\ \mu\text{m}$ size range at $3\mu\text{m}$ resolution and Cloud Particle Imager (CPI) with $2.3\text{-}2300\ \mu\text{m}$ size range at $2.3\mu\text{m}$ resolution (SPECinc 2012). In other words, it is an extended version of 3V-CPI integrated with FCDP. The 3V-CPI, an imaging probe, comprises of two channels of 2D-S as well as the CPI probe and is used to measure the particle size, shape, and concentration. The CPI was operating in a trigger mode to take high resolution images of the particle when the particle is found in the overlap region of the 2 laser beams from the 2D-S probe. The CPI camera provides grayscale images with a maximum rate of 400 frames per second. Therefore, the CPI provided information on crystal habit while 2D-S provided data on particle size distribution. The sectional view of the instrument as well as its optical layout is shown in Fig. 3.10.

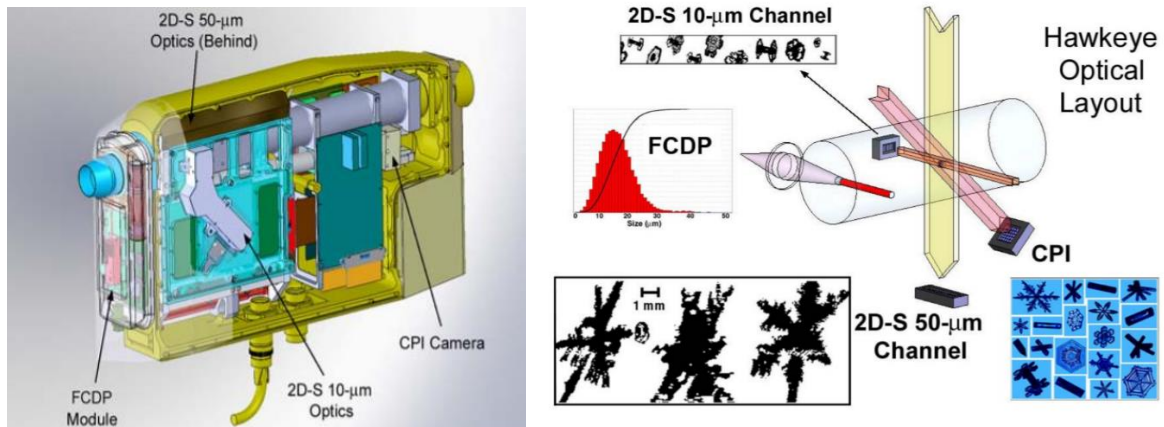


Fig. 3.10: The sectional view of Hawkeye instrument (left) and its optical layout (right).
Reproduced from SPECinc (2011).

3.2.4 Aerosol Ice Interface Transition Spectrometer (AIITS)

AIITS is a light scattering (indirect imaging) instrument used to investigate the morphology of airborne particles, in particular ice crystals in high altitude cirrus clouds. Indirect imaging is particularly useful for small crystal analysis since optical (direct) imaging is often constrained by depth of field, aberrations, and diffraction. Therefore, the lower size limit is much larger with direct imaging. It works by introducing a laser beam to an individual particle and the forward scattering patterns are captured in two dimensions by two high-resolution cameras (Stopford *et al.* 2015). The instrument can analyse the individual particles ranging from 1 to 100 μm in size, carried in the airflow. It was developed at the University of Hertfordshire as part of the NERC project Co-ordinated Airborne Studies in the Tropics (CAST).

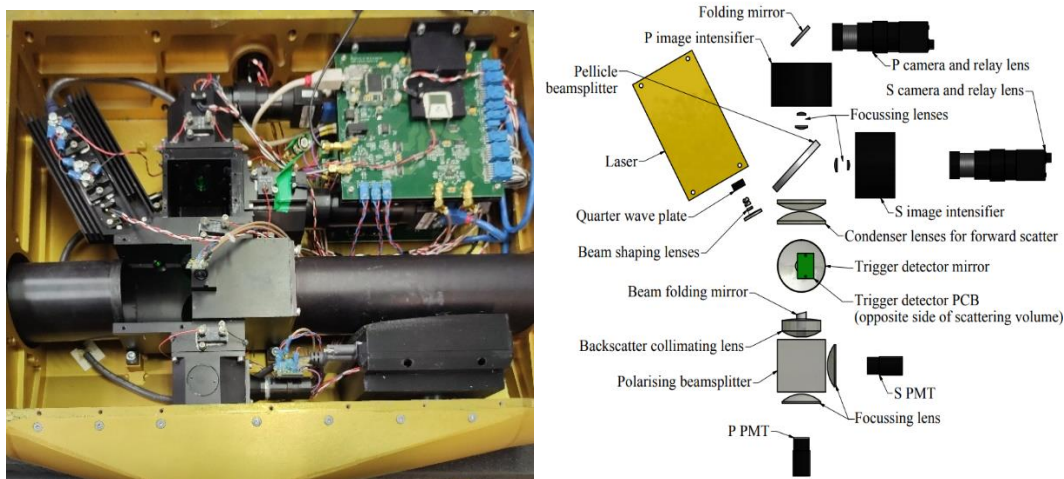


Fig. 3.11: The AIITS instrument (left). The instrument layout, picture courtesy of Dr Chris Stopford (right). The components are not to scale.

The instrument shown in Fig. 3.11, consists of a laser source (532nm), photomultiplier tube (PMT), beam splitters, trigger detector system and cameras. The instrument weighs approximately 35kg; its outer casing is made of anodized aluminium. The particle enters through the inlet (left side) of the instrument shown in Fig. 3.11. The inlet is designed to reduce shattering of ice with an angled leading edge.

Optionally, the laser light is passed through a quarter-wave plate, which converts linearly polarized light into circularly polarized light (and vice versa). This is directed towards the beam steering mirror, which reduces the size of the optical system by bending the beam while redirecting the beam to the scattering volume. The scattering volume is defined by the region intersected by the trigger detector mirror (bottom) and the photodiode (top). To be triggered, a particle must be within the scanning area of the detector as well as in the path of the beam. The emerging scattered light passes through a Pellicle beam splitter and the images are captured by the intensified CCD cameras.

The instrument can operate in two different modes: forward scattering intensity mode and forward and backward depolarisation mode. In the former mode, the quarter wave plate converts the beam into circularly polarized light and the cameras capture the 2D intensity patterns. While operating in the latter mode, the beam will be linearly polarized, and independent images of parallel and perpendicular polarization are taken by the two intensified cameras with up to 100fps (frames per second). Backward scattered depolarisation is captured on to two PMTs with orthogonal polarisation filters applied. The images are greyscale images (8-bit JPG) with a dimension of 512x640 pixels. The forward and backward scattering pattern have an angular range of 6°-25° and 163.5°-173.7° respectively. Unfortunately, one of the intensifiers was broken during the testing phase of ATTREX 2015 science flight and therefore, the polarised images were not captured.

All the instruments described in this section can be mounted on aircrafts. The specifications of these instruments are summarized in Table 3.2.

Instrument	Sample Volume at 100m/s	Sample Area	Collection angle	Measurement Range	Optimum size range (μm)
FCDP	0.08 L/s [1]	2.4mm x 2.4 mm [2]	4-12° [2]	1.5-50 μm [2]	10-25 μm [3,1]
2-DS	16 L/s [4]	0.128 cm x 6.3 cm [5]	-	10-1280 μm [6]	>30 μm [3]
CPI	0.37 L/s [4]	2.3mm x 2.3 mm [7]	2.5-8.2° [8]	2.3-2300 μm [9]	>30 μm [3,10]
AIITS	0.74mm ² x 90 μm = 0.06mm ³ [11]	0.74mm ² [11]	6-25° [12]	1-100 μm [11]	1-100 μm [11]

Table 3.2: Specifications of different instruments.

The results from the NASA probes are compared with the AIITS' results in Section 6.3.

¹ Thornberry et al. 2017

² Glienke et al. 2020

³ Dr Richard Cotton, private communication, Oct 2023

⁴ Baumgardner et al. 2011

⁵ Sample cross section, Lawson et al. 2006a

⁶ NASA (2022)

⁷ Przybylo et al. 2022

⁸ SPECinc (2013)

⁹ SPECinc (2012)

¹⁰ Lawson, R. P. et al. 2008

¹¹ Dr Chris Stopford, private communication, Nov 2023

¹² Stopford et al. 2015

3.3 Images taken by the CPI

The images taken by the CPI instrument on 5th March 2015 are given in Fig. 6.25. In the figure, a few hexagonal plates and columns can be seen, but predominantly the crystals look quasi-spheroidal. The spheroidal crystals may not be spheroidal in reality; it might be due to the constrained resolution of the instrument. Likewise, the surface texture cannot be determined from the given images. This is where additional information can be drawn from the AIITS images, as the intricate features in the scattering pattern can be clearly seen. And by solving the inverse problem, the crystal type can be identified. An example image, taken using AIITS instrument is shown below (Fig. 3.12), where the speckle-like feature is visible, indicative of a rough surface texture. Based on modelling results, it was found that the crystal was indeed a rough solid column (details in Section 5.2.2).

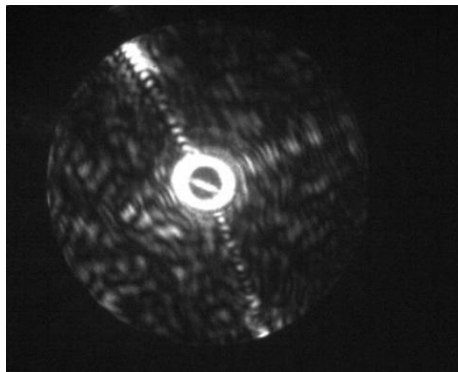


Fig. 3.12: AIITS no.1906

This chapter provided an introduction to the ATTREX mission, and several probes used for measurements including the AIITS. Next, we look at how the features in the scattering pattern images taken by the AIITS help in identifying the crystal types. The method used to simulate the scattering patterns of model crystals and some terminologies related to crystal modelling are also described.

4. METHODOLOGIES

In the first section of this chapter, some of the terminologies associated with crystal modelling are discussed. The crystal modelling requires different analytic as well as computational techniques as it varies with type of crystal. The crystal type can be identified by analysing the features in the scattering pattern. This is outlined in Section 4.2. This is followed by the method which is used to simulate the light scattering pattern as well as the steps involved in estimating ice crystal geometry. Finally, the process of extracting the crystal diameter and surface roughness from rough crystals using two different algorithms is discussed in detail in Sections 4.5.1 and 4.5.2 respectively.

4.1 Terminology

Some of the terminologies that are often used in this and following chapters are explained here.

4.1.1 Euler angles

The Euler angles are used to define crystal orientation. For example, the model crystal needs to be rotated several times using different Euler angles, until a best match between the simulated images and AITS images are found. Hence, they play a key role in accurately estimating the crystal sizes (discussed in Chapter 5).

Consider a (three dimensional) Cartesian co-ordinate system with x , y , and z axes (perpendicular to each other) and the propagation of incident beam is in $-z$ direction, with the particle situated at its centre. An example is shown in Fig. 4.1.

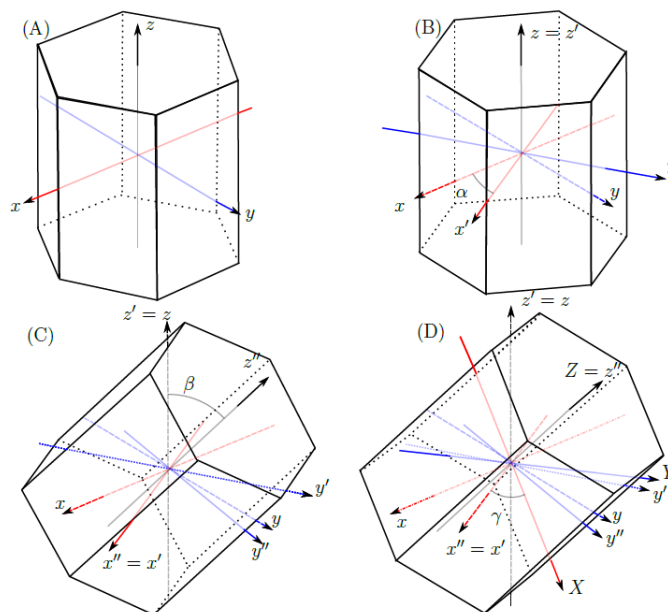


Fig. 4.1: Changing the orientation of a column crystal using the Euler angles, taken from (Taylor 2016). Step-by-step rotation from the crystal's initial to final orientation using three different angles are shown through A-D.

The hexagonal column aligned with its axis parallel to the z-axis, is rotated in 3 steps defined by 3 angles: alpha (α), beta (β) and gamma (γ) respectively. The original orientation before any rotation is shown in Fig. 4.1 (A). Once rotated, the subsequent rotations are calculated from the new co-ordinate system. This results in 3 axes of rotation: 1) Rotate around z axis by an angle α ($z'=z$ and the new axes are named x' and y'). 2) Rotate around the new x' axis by an angle β ($x''=x'$ and, y' and z' changes to y'' and z''). 3) Rotate around the z'' axis by an angle γ ($Z=z''$ and, x'' and y'' changes to X and Y). These three rotations are shown in Fig. 4.1 (B-D) respectively. If rotated in the clockwise direction, the angle of rotation will be positive. In this paper, Euler angles are specified in radians, unless otherwise stated.

4.1.2 Aspect Ratio

The aspect ratio (AR) is defined as the ratio of the hexagonal prism height (H) to its basal diameter ($D = 2 \times \text{prism radius}$). The aspect ratio is larger than one for columns, and smaller than one for plates. Examples are shown in Fig. 4.2 using a hexagonal column and plate. Crystals with aspect ratio unity are often called as equiaxed as their prism height and basal diameter are equal.

$$AR = \frac{H}{D}$$

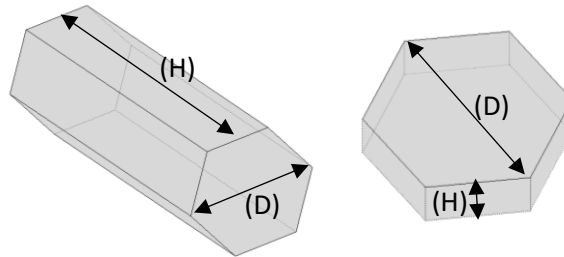


Fig. 4.2: Planar crystals: column (left) and plate (right) with dimensions indicated.

4.1.3 Size Parameter

The size parameter (X) is the product of wave number ($k = \frac{2\pi}{\lambda}$) and the characteristic size (r) of the particle. It is dimensionless.

$$X = kr = \frac{2\pi r}{\lambda}$$

In many applications the characteristic size is defined as $\frac{D_{max}}{2}$, where D_{max} is the maximum dimension of the particle.

$$X = \frac{\pi D_{max}}{\lambda}$$

For a hexagonal prism, $D_{max} = \sqrt{H^2 + D^2}$ where H and D are the height and diameter of the particle, respectively.

Since the AIITS detects particles in the 1-100 μm diameter range at a wavelength of 532nm, the current study is only focused on size parameters ranging from 5.9 to 590.5.

4.2 Features of different types of crystals and their scattering patterns

Different features are manifested in the scattering pattern depending on the crystal type. In general, the scattering pattern varies with particle shape, size, texture, refractive index, and wavelength at which it is measured. As this study is focusing on ice crystals with refractive index 1.31 at the wavelength 532nm of the AITS' laser beam, the scattering pattern depends only on the crystal shape, size, and texture. By analysing the features in the pattern, it is possible to identify the overall shape of the crystal and other properties such as whether it is rough, rounded, or pristine. In general, pristine crystals exhibit bright, sharp, and well-defined scattering arcs; rough crystals show speckle-like features and crystals with significantly rounded edges are likely to display ring-like structure in their scattering pattern. In plates, due to the crystal orientation, 22° halos cannot be observed. The features of different types of crystals and their scattering patterns are summarized in Table 4.1.

Crystal Type	Features of crystal with sub-categories	Features in the scattering pattern
Plates	<ul style="list-style-type: none"> - orientated preferentially on its basal facet (perpendicular to the gravitational force). - can be regular hexagonal, trigonal, scalene or droxtal type with pristine/round edges and smooth/rough surface 	<p>Regular Hexagonal: 6 prominent scattering arcs extending from the centre radially.</p> <p>Scalene: 4 prominent and 2 weak scattering arcs.</p> <p>Trigonal or scalene with 3-fold symmetry: 6 scattering arcs with distinct features.</p> <p>Droxtals: 3 or more scattering arcs with bright spots (halos). These can be regular or scalene type as well. (For details, see Section 5.1.4)</p> <p>Rough plates: Speckle-like feature with 3 or more arcs.</p> <p>Rounded plates: Ring-like structure with 3 or more arcs.</p>
Columns	<ul style="list-style-type: none"> - orientated preferentially on prism axis near perpendicular to the gravitational force. - can be short or long columns and needles (extremely thin solid columns). - can be rough or smooth with rounded, or pristine edges. 	<p>Smooth columns: 2 bright scattering arcs in the centre (later mentioned as major central arc) with or without parallel lines. The central arc can contain maxima and minima. The number of these will increase with crystal diameter. Often a bright spot (halo) can be seen towards the end of one scattering arc.</p> <p>Needles: Major central arc without accompanying parallel lines.</p> <p>Rough columns: Speckle-like feature with a major central arc.</p>
Rough crystals	<ul style="list-style-type: none"> - any orientation. - crystals with rough surface. 	Speckle-like feature.

Smooth Rounded crystals	- any orientation. - crystals with rounded edges and smooth surface.	Ring-like structure.
Rough Rounded crystals	- any orientation. - crystals with rounded edges and rough surface.	Combination of both ring-like and speckle-like features.

Table 4.1. Features of different types of crystals and their respective simulated patterns.

These main and sub-crystal categories, what their simulated scattering patterns look like, how specific models are created, how the simulated patterns are generated from these models and how they are compared, are all explained in detail in Chapter 5 along with examples.

4.3 Methods for simulating light scattering patterns

In principle, light scattering patterns can be simulated by exact methods (finding solutions to the scattering problem by directly solving Maxwell's equations). For example, the T-matrix method (*Mishchenko et al. 2014*) is an exact method, and the discrete dipole approximation (*Yurkin et al. 2007*) is a numerically exact method. Although accurate, exact methods' computational limits makes them unsuitable for large particle sizes and/or particles with complex shape. For such particles hybrid physical-geometric optics can be applied (*Yang et al. 2019, Konoshonkin et al. 2017, Taylor 2016, Hesse et al. 2018*). Within this project, the Beam Tracing Models (*Taylor 2016 and Hesse et al. 2018*) are applied. They are briefly described in the next section.

4.3.1 The Beam Tracing Model (BTM)

For this work two versions (*Taylor 2016 and Hesse et al. 2018*) of the Beam Tracing Model (BTM) were used. In both methods the incident plane wave is split into beams. In *Taylor (2016)* method, the beams are defined by the projected cross sections of the beam-facing facets, but in *Hesse et al. (2018)* method, beams are defined by triangulating the projected cross section of the particle. Following Snell's law, each beam is reflected and refracted at the particle surface. This is implemented differently in the two methods: if a transmitted beam hits more than one facet, it is split into sub-beams, which are again reflected and refracted, etc, until beam energy is below a set minimum or a set number of recursions is reached in *Taylor's method (2016)*, whereas the small triangular beams are not further subdivided in *Hesse et al. (2018)* method.

In both methods, externally reflected and outward refracted beams undergo Kirchhoff diffraction, and the far field is calculated for the angular region of interest. In addition to tracing the part of the incident wave hitting the crystal, external diffraction needs to be considered. Following Babinet's¹³ principle, this is done by computing Kirchhoff diffraction by the beam facing facets. *Taylor's (2016)* method is very fast, but the current implementation is only applicable to simple geometric shapes like hexagonal prisms, whereas the method of *Hesse et al. (2018)* is not restricted by such limitations to particle shape, but it is more computationally expensive.

¹³ Babinet's principle states that the diffraction pattern from an aperture is identical to that from a complimentary screen, however there is a phase shift of π in the electric field (*Hecht, 2002*).

4.4 Estimating the shape and size of crystals

In general, estimating the crystal geometry is a four-step process, which is outlined below. In step 1, an overall idea about the crystal habit is obtained through the analysis of features in the scattering pattern. However, for an accurate estimation of both size and shape, steps 2-4 are to be followed. After finding the crystal type, corresponding model crystals are generated. The BTM is used to simulate the scattering pattern of model crystals. Model crystals of various sizes and orientations are used until the simulated patterns matches the AIITS images. Once they match, the crystal size is estimated depending on the crystal habit.

Step 1: Find the crystal shape: Analyse the features in the light scattering pattern images to find the type of ice crystal. The features of different types of crystals were already addressed in Section 4.2. This can be done by visual inspection. However, it is challenging to classify the crystal habits manually and the process will become even harder for larger datasets. This is the motivation behind implementing a Deep Learning Network, an automated neural network to classify the scattering images based on the crystal type, which will be discussed in Chapter 7.

Step 2: Model specific crystal: Generate the specific crystal files using the relevant program. Different programs (in Fortran) are used to generate crystals with different geometries like pristine hexagonal plates, quasi-spheroids, rough crystals etc. Model crystals of different sizes and in different orientations are required. Model crystals are initially produced in $\alpha=\beta=\gamma=0$ orientation. These crystal files are used alongside MATLAB code to visualize the particle shape. For more complicated crystal files like rough crystals, a software named 'QuickDraw 3D Viewer' is used for visualization.

Step 3: Simulate the scattering pattern: The model crystal file obtained in step 2 is used as input for the Beam Tracing Model (discussed in Section 4.3.1), to produce 2D scattering pattern of the model crystal. The simulated pattern is then compared (by eye) with that of the AIITS scattering pattern image. Since the pattern changes with crystal size and orientation, steps 2 and 3 are repeated with different crystal sizes and orientations until the two patterns match. By changing the values of the Euler angles, different crystal orientation can be obtained. The scattering pattern is visualized using MATLAB.

Step 4: Estimate particle size: Once the simulated pattern and the AIITS scattering pattern image match, the crystal size is estimated. The process of size estimation varies with the crystal habit and is explained in detail in the next chapter. For example, size estimation of a smooth hexagonal prism is done manually by analysing the angular distribution of diffraction minima in the scattering pattern (or the width of the scattering arcs). As the width of the scattering arc increases, the crystal size decreases. For a rounded crystal, size can be estimated based on the number of 'ring like' structures in the scattering pattern. The higher the number of rings, the larger the crystal. For rough crystals, smaller speckles are indicative of larger crystals, and vice versa.

In general, these steps are followed to estimate the shape and size of all crystals. Chapter 5 provides the process of modelling different types of crystals, comparing it with AIITS images and estimating the crystal sizes, in detail with examples. For rough crystals, two MATLAB algorithms are used to estimate particle diameter as well as particle roughness. These are explained in the next section.

4.5 Estimating the size and roughness of rough crystals

One of the easiest ways to identify the rough crystals is to check whether its scattering pattern contains any speckle-like features. For rough plates and rough columns, in addition to speckles, scattering arcs will be visible. However, in some other cases like rough quasi-spheroids or irregular crystals, the absence of additional unique features (nothing other than speckles) makes the detection of underlying crystal habit challenging. For this reason, only

rough plates and rough columns are separately classified. Other crystals are collectively grouped into the 'Rough crystal' category as their crystal habits are unknown. See Section 5.4 for more information.

Unlike the analysis described in the previous section, the process of rough crystal estimation is automated using MATLAB. That is, the images are directly fed into the program to calculate the crystal diameter. However, the results have been validated by manual analysis as well and this is described in Section 5.4.1 in detail. First, the Speckle Analysis code used to calculate the rough crystal size, is discussed. Then, the Combined Roughness code is discussed, which evaluates how rough the crystals are on a scale between 0 to 1, ranging from smooth to very rough respectively. In each section, the accuracy of the algorithm is reviewed, and changes were made where appropriate.

4.5.1 Speckle Analysis

To estimate the size of the rough crystals, the method described in Ulanowski *et al.* (2012) is followed, where the authors state that the median of the speckle area is inversely proportional to the particle size. The equation,

$$D \approx \frac{4\lambda z}{\pi D_s} \quad (4.1)$$

is used to estimate the particle size or diameter (D). λ is the wavelength of light (532nm), z is the distance between the particle and the detection plane in equivalent pixels, and D_s is the average diameter of the speckle spots in pixels.

Based on the method described in Ulanowski (2012), a Speckle Analysis programme has been written (in MATLAB) to estimate the crystal size by analysing the speckles in the scattering pattern (Appendix 11.1). The flowchart of the code is shown in Fig. 4.3.

The first step is the image pre-processing stage which involves 2D median filtering and displaying the relevant area of the greyscale image. By using 2D median filtering, the noise can be reduced without damaging the edges of the image.

The next step is the greyscale morphological reconstruction of the image using the 'imreconstruct' function which has two parameters: Marker and Mask. The image which needs to be enhanced is used as the Mask. The Marker is used to mark the regions to be enhanced. The greyscale reconstruction simply extracts the connected components of Mask which are 'marked' by the Marker using iterative geodesic dilations (Vincent 1993). The geodesic distance is the shortest distance between two pixels in the Mask and is highly dependent on pixel connectivity (Vincent 1993). As the Marker value, the image is multiplied by a constant, 0.6 which is recommended in Ulanowski *et al.* (2012). Once the morphological reconstruction is done, the regional maxima is computed using 'imregionalmax' function. Since this function finds the regional maxima in the reconstructed image by replacing the pixels of constant intensity values with 1 and their neighbours of lower pixel values with 0, the speckles can be identified as pixel values of 1. At this point the image will be binary or logical.

Finally, the function 'regionprops' is applied on the regional maxima (speckles) to find the properties of the speckles like speckle area. The median area of the speckle is found, from which the diameter of the speckle (D_s) is derived. This is done by equating the median speckle area to the equivalent circular area. The speckle diameter (D_s) is then substituted into Equation 4.1 to find the particle diameter (D).

Ulanowski *et al.* (2012) recommends using a quality criterion (Q),

$$(4.2)$$

$$Q = 4C/(1 - C)$$

where C is the spot coverage, $C = \frac{A}{A+A_b}$, A is the total speckle area and A_b is the background area. Q has the maximum value ($Q = 1$), when $C = 1/2$ which occurs when $A = A_b$ and the lowest value ($Q = 0$), when $C = 0$ or $C = 1$ (when either A or A_b is zero). The results are rejected if the quality criterion value falls below 0.4. The chosen threshold is based on comparing true and predicted values where the correlation value is maximised.

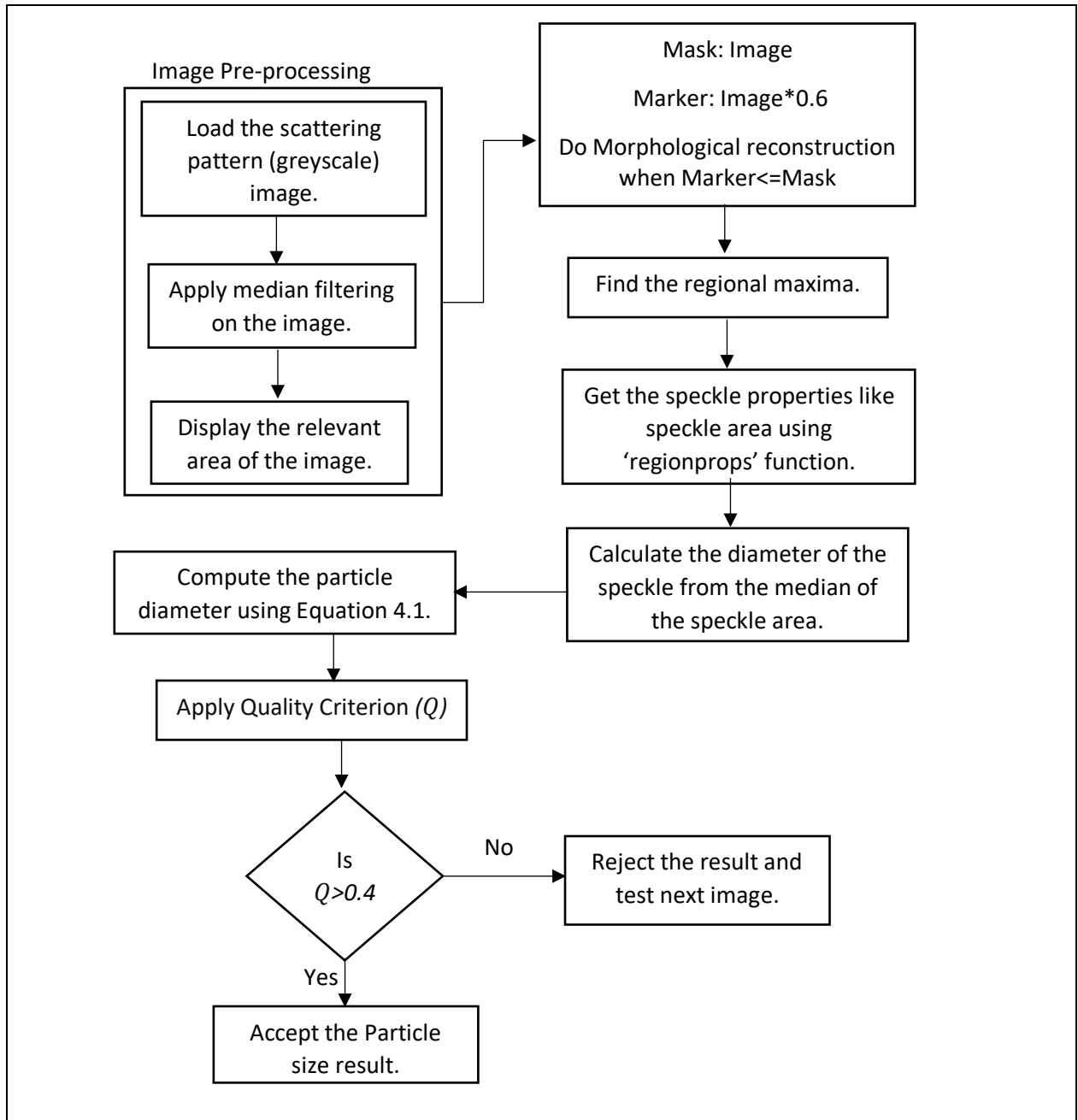


Fig. 4.3: Flowchart of the Speckle Analysis code.

The speckle analysis code has been tested using simulated scattering pattern images and the result is described in the next section.

The value of 'z' in Equation 4.1 is calculated for the simulated images as follows (Fig. 4.4):

The simulated images have a dimension of 511x511 pixels:

$$z = \frac{511/2}{\tan 25^\circ} = 547.92 \text{ pixels}$$

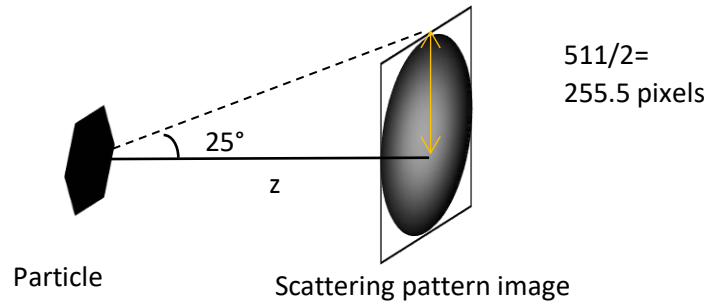


Fig. 4.4: Figure showing the geometry for calculating value 'z'.

On substituting $\lambda=532\text{nm}$ and $z =547.92\text{pixels}$, Equation 4.1 reduces to:

$$D = \frac{371.3}{D_s} \mu\text{m} \quad (4.3)$$

4.5.1.1 Testing the Speckle Analysis code using simulated scattering images

The code was tested using the simulated scattering pattern images of modelled crystals. The rough crystal models of various roughnesses, types and sizes were generated using the method described in Collier (2014). Since the sizes of these crystals were known in advance, it was straightforward to test the accuracy of the prediction results. There were 25 entries in total with particle diameters ranging from about 10 to 100 μm , consisting of plates, columns, and spheres in different orientations and with various degrees of roughness. The simulated pattern images were saved in .jpg image format. As an image pre-processing step, these were converted to greyscale images with only the region of interest displayed. The rest of the process is the same as shown in the flowchart Fig. 4.3.

In Fig. 4.5, test of the simulated pattern of a rough column with radius 10 μm and length 30 μm using the Speckle Analysis code is shown in successive steps as an example. In the top panel, the simulated image in .jpg is given in Fig. 4.5 (a), the image after pre-processing is used as Mask in (b), and the image multiplied by a constant 0.6 is used as the Marker in (c). The resulting image after morphological reconstruction using the Marker and Mask is shown in (d). The regional maxima obtained from the reconstructed image is shown as the binary image in (e). The 'regionprops' function is used to get the area of the speckle and its median is computed. To analyse the proportion of speckles taken into consideration using the 'regionprops' function, extra lines of code were added, and the selected speckles are highlighted in (f).

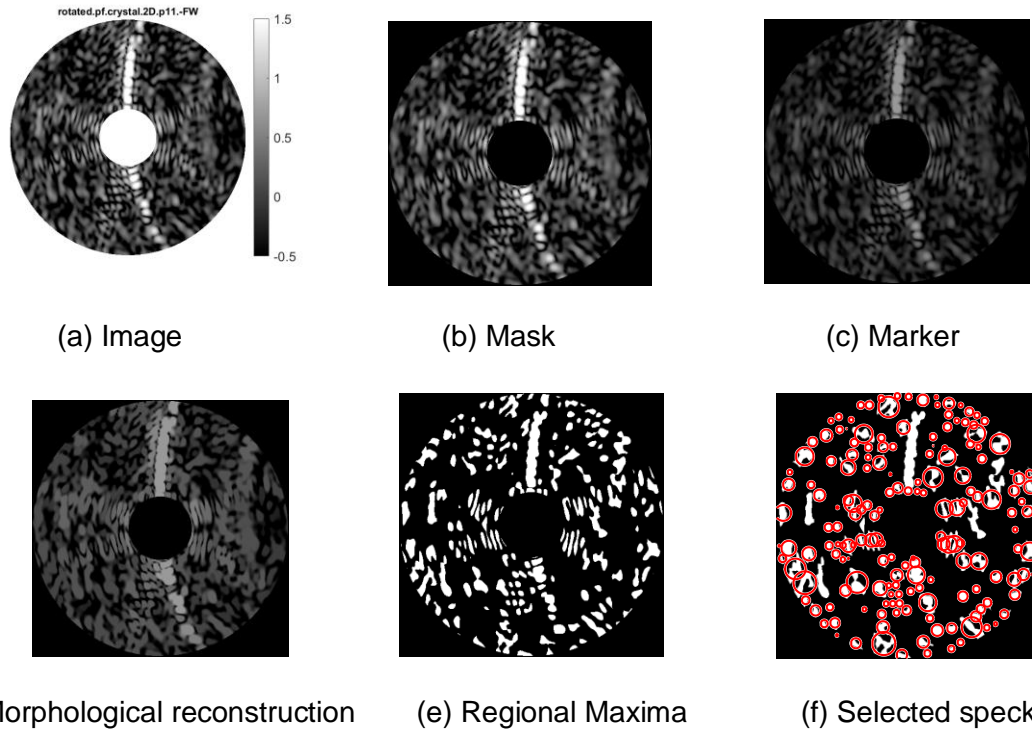


Fig. 4.5: The step-by-step output of the Speckle Analysis code while using 0.6 as the Marker value. (a) The simulated image, (b) the cropped image used as the Mask, (c) the image multiplied by 0.6 used as the Marker value, (d) the result of morphological reconstruction using Marker and Mask, (e) the regional maxima in the reconstructed image and (f) highlighting the speckles that are considered in the reconstructed image.

The maximum dimension of the crystal was compared against the diameter predicted using the Speckle Analysis program. Regarding the Quality Criterion (Q), Ulanowski *et al.* recommend that the predicted result is acceptable if $Q > 0.4$. However, on analysing the Q values and the predicted result, they were not consistently correlated. That is, the predicted crystal diameter matched with the actual crystal diameter in some cases where Q value is less than 0.4. On testing simulated images no particular relationship was found between Q value and predicted result. Hence the quality criterion was not utilised in this analysis.

Ulanowski *et al.* (2012) states that the median of the speckle area is inversely proportional to the particle size. This is confirmed in the current study. In Fig. 3.6, the estimated particle diameter is plotted against the inverse of the median speckle area of the simulated images. The red line is the Equation 4.1 (or Equation 12 in Ulanowski *et al.* (2012)). The equation holds true for smaller crystal sizes up to $30\mu\text{m}$ in diameter. However, for crystals larger than $30\mu\text{m}$, it departs from the red line indicating that the speckle sizes are larger for larger crystals.

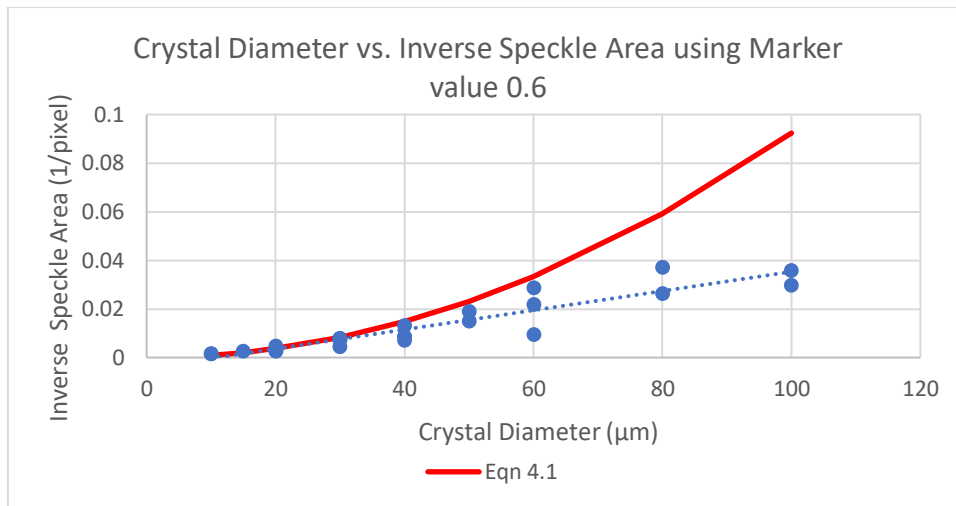


Fig. 4.6: A plot of estimated particle diameter versus the inverse of the median speckle area for the simulated scattering images of rough spheres, plates, and columns. The trendline is shown as blue dotted line and Equation 4.1 as red line.

In comparison, a similar plot from Ulanowski *et al.* (2012) is shown in Fig. 4.7. They used a variety of samples like living cells, rough and smooth dust grains as well as ice analogues. It is evident from the plot that, as grain size increases beyond 30 μm , the black line representing Equation 4.1 diverges from the data points.

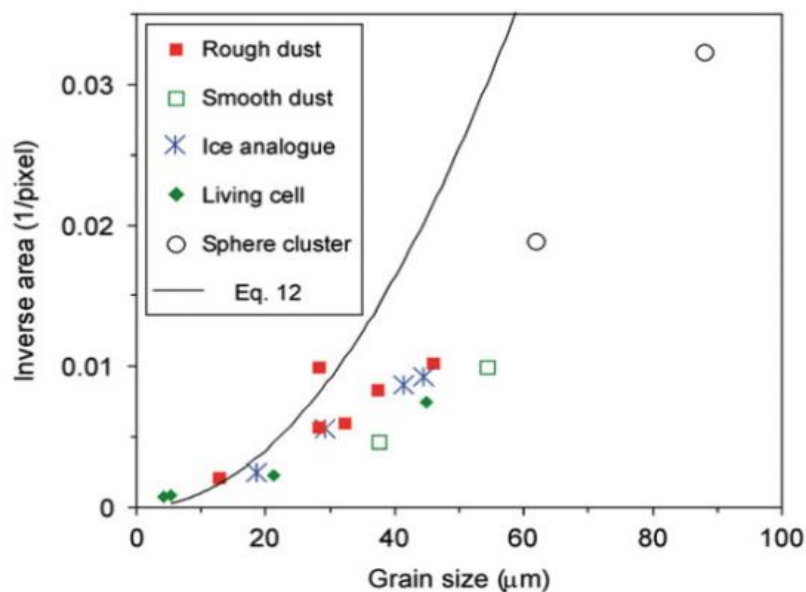


Fig. 4.7: A plot of grain size versus the inverse of the median speckle area for a variety of samples including dusts, living cell and ice analogue in size range:4-88 μm , taken from Ulanowski *et al.* (2012). Equation 4.1 is shown in black line.

Since Equation 4.1 does not fit for crystal sizes greater than 30 μm , the algorithm has been tested with different Marker values rather than just 0.6. Values between 0.6 and 0.9 were tested in steps of 0.1. The resulting plot of crystal diameter against inverse median speckle area is shown in Fig. 4.8 and it was found that the line representing Equation 4.1 passes in

between the datapoints of Markers 0.7 and 0.8. Hence, an attempt was made to test Marker 0.75 as well. The general trend is that, as the Marker value increases, the median speckle area decreases.

On analysing Fig. 4.8, it is obvious that the line representing Equation 4.1 goes through majority of the datapoints for Marker values 0.75. The crystal diameter is overestimated, if the datapoints are above the Equation 4.1 line and on the other hand, underestimated if they are below the Equation 4.1 line.

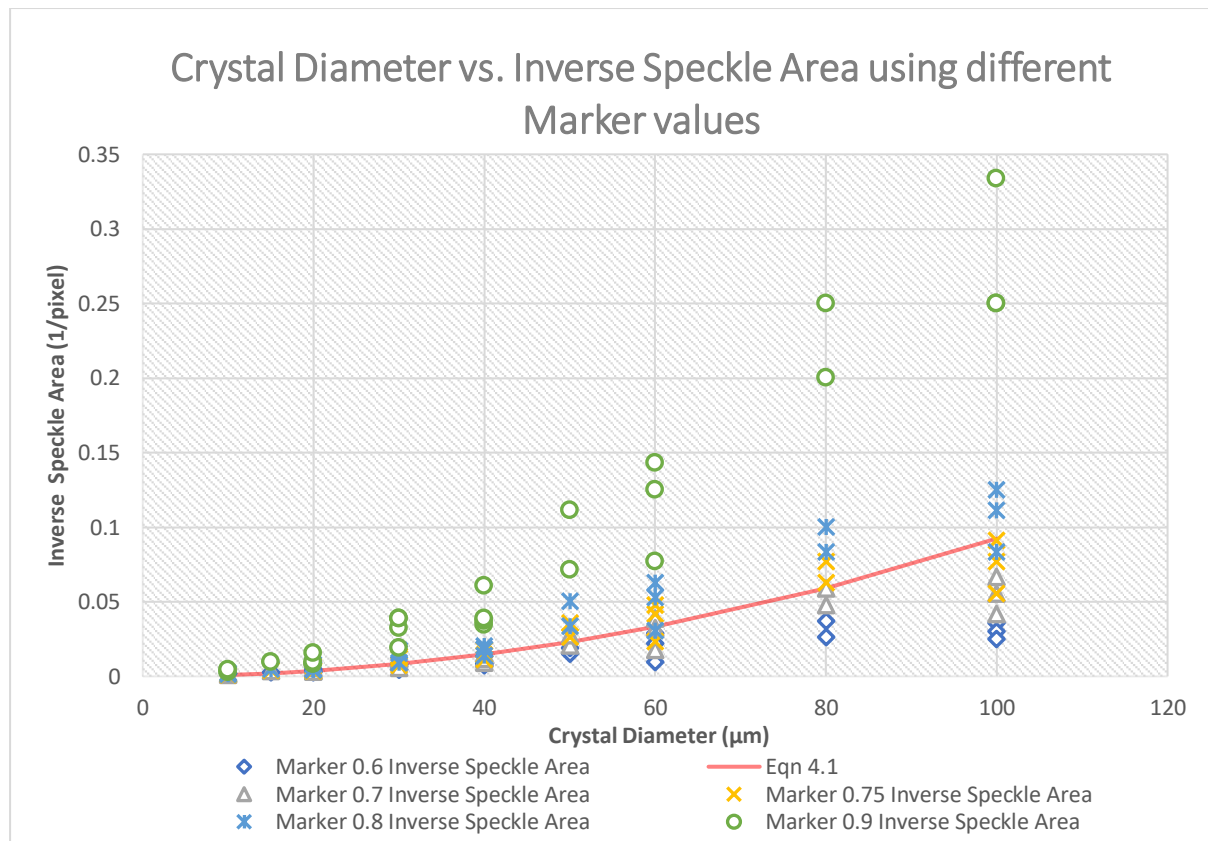


Fig. 4.8: Crystal diameter versus the inverse of the median speckle area for simulated images using Marker values between 0.6 and 0.9. The Equation 4.1 is shown in red line.

The Sample Standard Deviation was also calculated for the different Marker values using the equation,

$$\text{Sample Standard Deviation} = \sqrt{\frac{\sum (ISA - ISAE)^2}{25 - 1}} \quad (4.4)$$

where *ISA* is the Inverse median Speckle Area obtained from reconstructed image and *ISAE* is the Inverse Speckle Area obtained from Equation 4.1. The different Marker values along with their standard deviation are given in the Table 4.2. The standard deviation values are low for Marker values between 0.7 and 0.8. Based on the plot in Fig. 4.8 and standard deviation calculation, 0.75 seems to be the optimal Marker value having the lowest standard deviation value of 0.0103.

Marker values	Sample Standard Deviation
0.6	0.0243
0.7	0.0145
0.75	0.0103
0.8	0.0159
0.9	0.0919

Table 4.2: The standard deviation of different marker values.

Though using Marker = Original Image x 0.75 was found to be optimal based on testing the samples of simulated images of crystal sizes between 10-100 μm and its sample standard deviation result, it is better not to rely on a constant Marker value that works for all crystal sizes. Based on Fig. 4.7 and Fig. 4.8, where different samples are used, both plots show a similar trend of predicting accurate crystal diameters up to 30 μm while using Marker value 0.6. Therefore, it appears that there is a relationship between crystal size and Marker value. Image dimension is another factor that affects the crystal diameter prediction. For example, the Speckle Analysis code predicts different values as crystal diameter for a simulated image of 511x511 pixel dimension compared to a resized image of 458x458 pixel dimension. For these reasons, an approximative process is recommended: start with a 0.75 Marker value and compare the speckle size in the reconstructed binary image with regional maxima with that of the speckles in the original image. If the speckle size in the reconstructed image is smaller, use a smaller Marker value, otherwise, use a larger Marker value. This will help in a more accurate crystal size prediction.

4.5.2 Combined Roughness

The crystal roughness can be characterized using the combined roughness parameter (Ulanowski *et al.* 2014). Depending on the crystal roughness, the combined roughness value varies from 0-1; with 0 being the least rough crystal and 1 being the roughest crystal. The combined roughness value is calculated based on analysing the textural features in an image. Textural features provide information on spatial distribution of intensities or more simply, the variations in the grey levels of pixels in an image. In the same manner whether a surface is smooth or rough can be differentiated by touching it, the high and low brightness values in neighbourhood pixels in an image can be manipulated to find out the image texture. As a statistical approach, Grey Level Co-occurrence Matrix (GLCM) is used to analyse the texture of different regions of the image. In the following section, the GLCM is explained with an example and its statistical features are described. The MATLAB program written for computation of the combined roughness parameter can be found in Appendix 11.2.

4.5.2.1 Grey Level Co-occurrence Matrix (GLCM)

GLCM provides information about grey level values in a neighbourhood region. For example, in areas with smooth texture, the range of values in the neighbourhood around a pixel is a small value; in areas of rough texture, the range is larger. In MATLAB, the function 'graycomatrix' is used to create a GLCM (also called Grey-level spatial dependence matrix). The matrix elements are numbers which specify how often the pixel value 'i' (grey-scale or intensity value) occurred adjacent to the pixel value 'j' at a distance 'd' and direction angle ' θ '.

Specifying the spatial relationship of GLCM:

The spatial relationship of GLCM can be varied using parameters like 'direction angle' and 'symmetric' in MATLAB. The direction angle ' θ ' (also called an 'offset') represents the direction along which the distance between a pixel and its adjacent pixel are calculated and the default 'offset' is set to a pixel and its horizontally adjacent pixel to its right (offset= [row_offset column_offset] = [0,1]). By default, 'symmetric' is set to 'false', that is the order of values (1,2) and (2,1) are counted differently. If it is set to 'true', both (1,2) and (2,1) will be considered as

same if they are adjacent, and its order is disregarded. Usually, second order statistics (distance between 2 pixels) are followed while defining the spatial relationship. Higher order (distance of 3 or more pixels) statistics results in complex computations and are time consuming.

For example, consider an image (Fig. 4.9 (a)), a two-dimensional matrix of 5x6 order which contains eight grayscale or intensity values between 1 and 8. This means that there will be 8 shades of brightness in the image. Its GLCM with an offset [0,1], distance 1(pixel) and symmetric 'false' is shown in Fig. 4.9 (b).

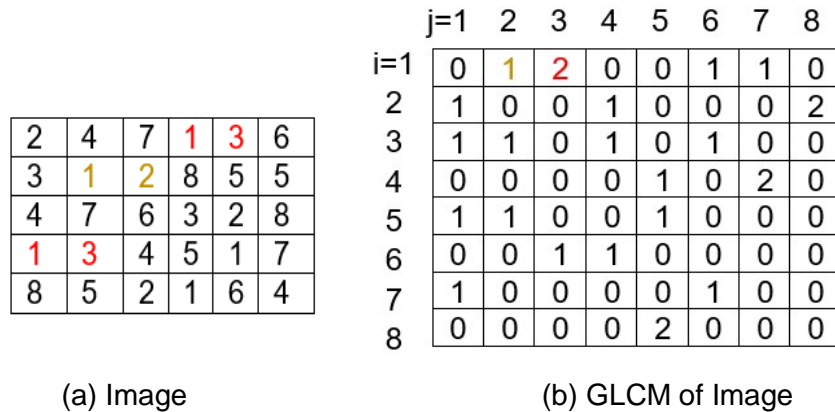


Fig. 4.9: (a) An image and (b) its GLCM shown using a 2D matrix.

The GLCM is not an image, but a matrix containing the frequencies of pixel elements based on the original image matrix. To illustrate, the first element in the GLCM (row 1, column 1) is zero as there is no occurrence of pixel value 1 adjacent to 1 in the image. The second element in GLCM (row 1, column 2) is 1 as there is one instance of pixel value 1 next to pixel value 2 in the image matrix. The third element (1,3) has occurred twice in the image matrix and hence 2 is tabulated in the GLCM. Similarly, the rest of the pixel pairs in the GLCM are computed.

In general, an image with 'n' different pixels generates a co-occurrence matrix of 'n x n' order. As the size of the matrix gets larger, MATLAB by default scales down the intensity values to eight equal width bins. For an image with grayscale value ranges from 0-255, the 256 grey levels are divided into 8 bins (of 32 levels each) and the values in each bin are mapped into a single grey value between 1 to 8.

The number of GLCMs depends on the number of offsets (or directions) and its dimension depends on the number of grey levels or more specifically, the binned grey levels. For an offset [0,1], only one GLCM is created as only one direction is specified. If a four directional offset is specified, four GLCMs are created and there will be 4 values for each statistical feature corresponding to each direction, from which the mean value is taken. Two examples are given below (Fig. 4.10) for creating GLCMs with the distance between the pixel of interest (P) and its nearest neighbour pixels in four directions.

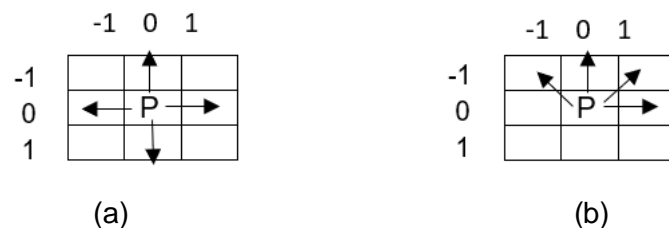


Fig. 4.10: An example showing the spatial relationship with (a) an offset = [0 1; 0 -1; -1 0; 1 0] and (b) an offset = [0 1; -1 1; -1 0; -1 -1].

Fig. 4.10 (a) has an array of offset = [0 1; 0 -1; -1 0; 1 0] specifying right, left, top and bottom directions respectively and Fig. 4.10 (b) with an array of offset = [0 1; -1 1; -1 0; -1 -1] specifying right, top right, top and top left directions respectively. As Ulanowski *et al.* (2014) is followed, a distance of 1 pixel in the 4 directions (offset = [0 1; -1 1; -1 0; -1 -1] is also referred to as 0°, 45°, 90° and 135° angles respectively). Also, the grey levels (0-255) are divided into 8 bins. Therefore, GLCMs are of order 8x8x4, that is, 4 different GLCMs for the four directions and each GLCM contains 8 rows and 8 columns (Haralick *et al.* 1973).

The MATLAB function 'graycoprop' normalizes the GLCM by equating the sum of its elements to one and calculates the statistical properties of the GLCM. The number of values in the statistical features depends on the number of GLCMs. There are four properties in total; they are dependent on angles and are defined as follows in MATLAB:

Contrast or variance: Measures the local variations in the GLCM. Or simply, it measures the intensity or value of a pixel and its neighbour over the whole image. If the pixel values are similar, the contrast of the image will be low, and the higher the amount of local variation in the image, the greater will be the contrast value.

$$Contrast = \sum_{i,j} |i - j|^2 p(i,j) \quad (4.5)$$

where $p(i, j)$ is the probability value in row 'i' and column 'j'.

Correlation: A measure of image linearity, so it measures how correlated a pixel is to its neighbour over the whole image. If the image is linear, higher the correlation value. Correlation is one for a perfectly positively correlated image.

$$Correlation = \sum_{i,j} \frac{(i - \mu_i)(j - \mu_j)p(i,j)}{\sigma_i \sigma_j} \quad (4.6)$$

where μ_i and μ_j are the mean of the GLCM computed on the row and column respectively. Similarly, σ_i and σ_j are the standard deviations computed on the row and column respectively.

Energy or uniformity: Measures the uniformity of the pixels. It is defined as the sum of squared entries in the GLCM.

$$Energy = \sum_{i,j} p(i,j)^2 \quad (4.7)$$

Higher the uniformity, higher the energy value. Energy is 1 for a constant image.

Homogeneity: Measures the closeness or density of the distribution of elements in the GLCM to the GLCM diagonal. Homogeneity is 1 for a diagonal GLCM.

$$Homogeneity = \sum_{i,j} \frac{p(i,j)}{1 + |i - j|} \quad (4.8)$$

In addition to the GLCM textural features, two additional features (related to image brightness) were considered:

- $\frac{RMS}{SD}$ (Ratio of root mean square brightness to its standard deviation)
- Kurtosis (K) (Ratio of the fourth central moment of the distribution to the fourth power of standard deviation) depicts to what extent a distribution contain outliers compared to the normal distribution.

According to Ulanowski *et al.* (2014), the most robust measurements produced by *Energy*, $\frac{RMS}{SD}$ and base 10 logarithm of *Kurtosis* were used to define the ‘combined roughness’.

$$Combined\ Roughness = 0.7 - \left(\frac{2 \times Energy}{3} \right) - \frac{\log_{10}(K)}{6} + \frac{RMS}{4000 SD} \quad (4.9)$$

The flowchart for creating a GLCM and extracting features from the matrix to compute the ‘combined roughness’ value is given below (Fig. 4.11). The first step is image pre-processing in which the region of interest is looked at after cropping and masking the rest of the image. There are two paths: one for finding the image brightness features and the other for finding the textural features. In path 1, the mean image brightness is scaled to 10 (from the grey scale range 0-255) and all the non-zero elements are extracted from the image to calculate the image histogram which provides the distribution of pixel values in each grey level bins. Then the statistical parameters like standard deviation, root mean square, and kurtosis are computed using relevant equations. In path 2, the image, which is of ‘uint8’ datatype is converted into ‘single’ datatype first. The type conversion is necessary as ‘uint8’ cannot accept ‘NaN’ values and if the zero entries are not addressed, the statistical parameters’ values are affected. Once the image is converted into ‘single’ datatype, all the zero entries are replaced with ‘NaN’ values. Then the GLCM is created with the specified spatial relationship (adjacent pixels in direction 0°, 45°, 90° and 135° with distance 1 pixel and symmetrical). The GLCM features (only ‘Energy’ is required) are extracted and the mean value will be calculated. The results from the path 1 and path 2 are substituted into the Equation 4.9 to find the ‘combined roughness’ value.

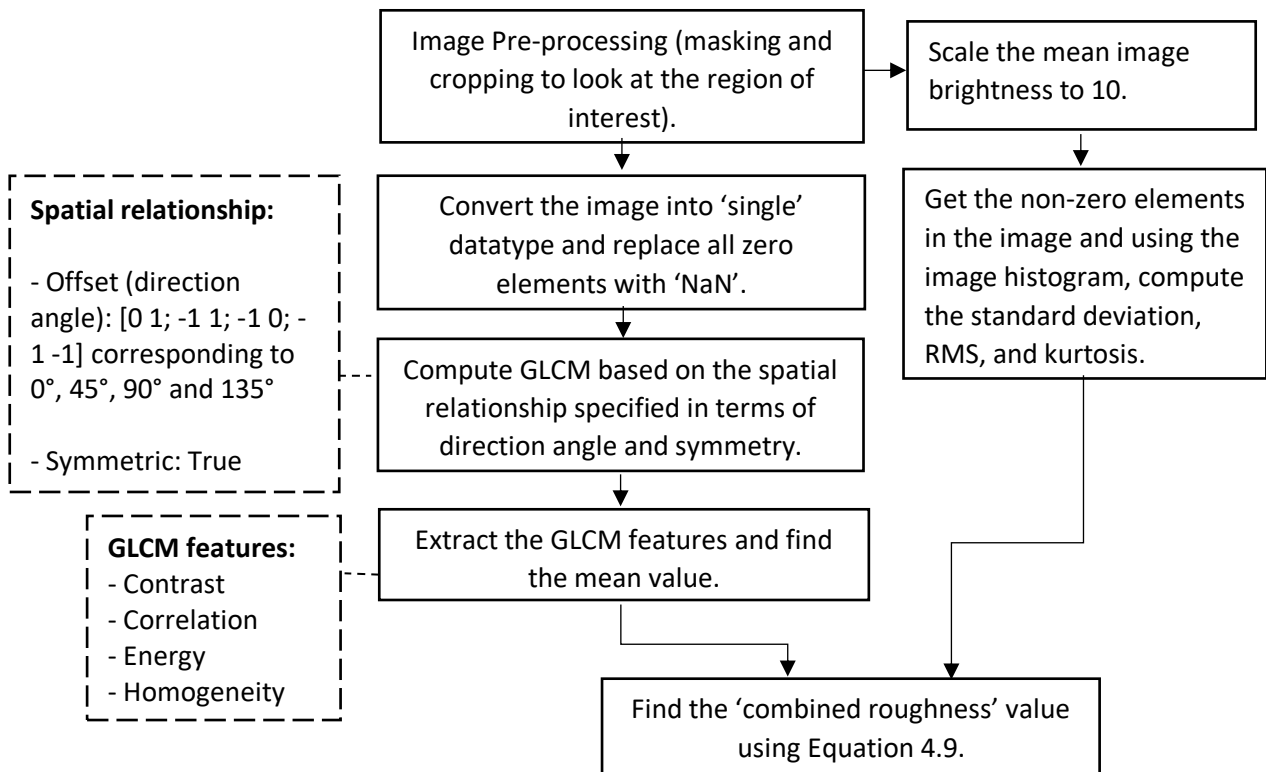


Fig. 4.11: Flowchart of the Combined Roughness algorithm.

The input images are AIITS images of unit8 type with 8 bits and $2^8=256$ grey levels. Even though the AIITS' image dimension is 512x640 pixels, only the area of interest (8-25°) represented by 458x458 were used to calculate the statistical features of GLCM. A few examples are given below (Table 4.3) representing different roughness of ice crystals. The first two crystals shown in the table have significant roughness (around 0.6) compared to the third one (0.3). The last image is a smooth needle crystal with combined roughness around 0.1. From Table 4.3, it is evident that the *combined roughness* values decreases as we go through the images from left to right. For the last image, *Energy* is higher (0.6979) implying a greater uniformity of the pixel values. In comparison, the first image has a lower *Energy* value implying a lesser pixel uniformity. On the other hand, there is high variance of pixel values in the first image, therefore a higher *Contrast*. *Energy* and *Contrast* are opposite to each other.

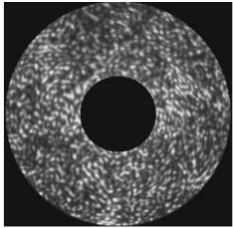
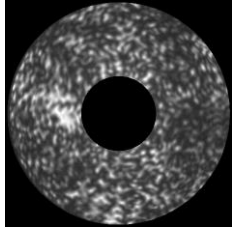
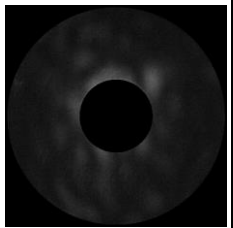
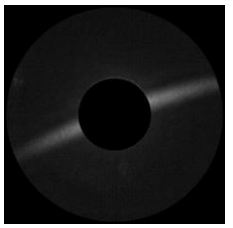
				
Image No:	2227	2376	10	1122
Contrast (Mean)	[0.34,0.46,0.33, 0.45] 0.3995	[0.28,0.33,0.26, 0.34] 0.3102	[0.156,0.16,0.15 6,0.159] 0.1582	[0.080,0.0826,0.0 804,0.0837] 0.0817
Correlation (Mean)	[0.88,0.84,0.88, 0.84] 0.8648	[0.91,0.89,0.91, 0.89] 0.9022	[0.682,0.675,0.6 83,0.675] 0.6793	[0.844,0.839,0.84 4,0.837] 0.8414
Energy (Mean)	[0.14,0.12,0.14, 0.12] 0.1338	[0.15,0.14,0.16, 0.14] 0.1530	[0.498,0.496,0.4 98,0.496] 0.4973	[0.698,0.697,0.69 8,0.697] 0.6979
Homogeneity (Mean)	[0.83,0.79,0.83, 0.79] 0.8170	[0.86,0.83,0.86, 0.83] 0.8501	[0.921,0.919,0.9 21,0.920] 0.9209	[0.959,0.958,0.95 9,0.958] 0.9591
Kurtosis (K)	4.2002	5.4383	10.89	17.41
log₁₀(K)	0.6233	0.7355	1.0371	1.2409
Root Mean Square (RMS)	2579	2609	2713	2799
Standard Deviation (SD)	3.79	4.35	4.44	6.05
RMS/SD	680.57	599.31	609.83	462.17
Combined Roughness	0.6771	0.6252	0.3480	0.1434
No. of Saturated Pixels	22	75	0	0

Table 4.3: A table showing details of four different images with different roughness scale along with other statistical parameters.

4.6 Dealing with weak images

It is difficult to get information from weak grayscale images. There is a wide range of functions available in MATLAB related to image enhancement. A built-in function 'adapthisteq()' has been found particularly useful for enhancing the image using Contrast-Limited Adaptive Histogram Equalization (CLAHE).

Fig. 4.12 shows a side-by-side comparison of an original and corresponding enhanced image. Many features that were hidden in the original image are revealed in the enhanced image. The ring-like structure in the enhanced image shows that it is likely to be the scattering pattern of a small quasi-spheroid crystal. In general, this type of enhancement might amplify the noise in the image too (which can be prevented using a 'ClipLimit' value in the range 0-1, default being 0.01); however, the additional parameters are not used as only the concealed features in a weak image are examined.

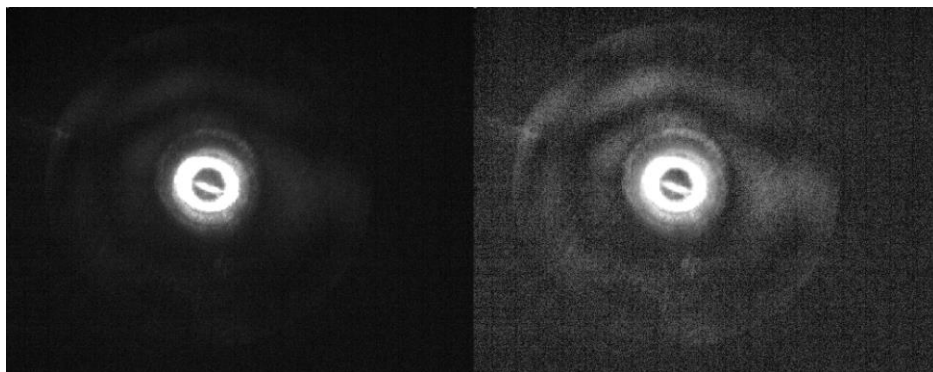


Fig. 4.12: A comparison of original image (left) and enhanced image (right) using contrast-limited adaptive histogram equalization.

The histogram plots are helpful for visualizing the intensity distribution of greyscale images. Even though they have 256 bins by default, it is evident that the distribution is concentrated in a small range, between 5 and 50 bins for the original greyscale image (Fig. 4.13 (a)). On the other hand, the distribution of intensities spread out up to 150 bins for the enhanced image (Fig. 4.13 (b)).

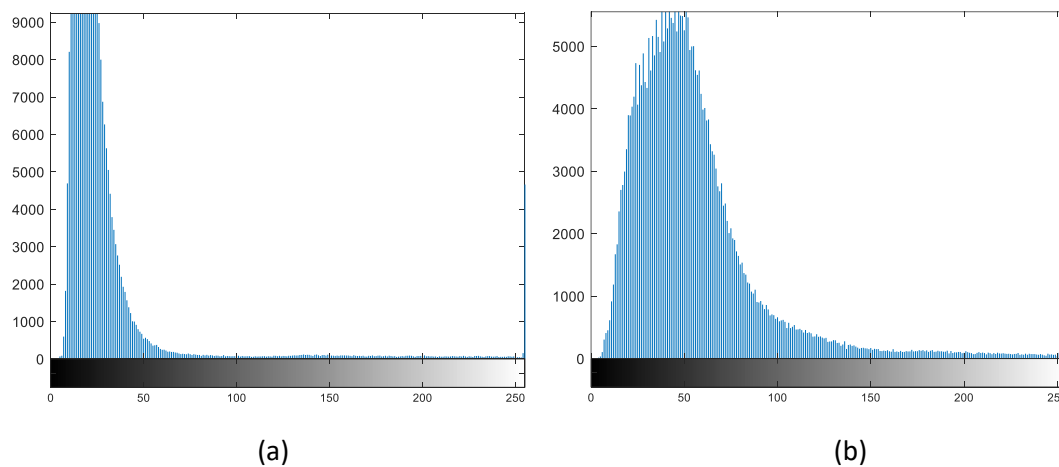


Fig. 4.13: A plot of histogram for the original greyscale image (a) and contrast-limited adaptive histogram equalization (b).

Compared to the regular histogram equalisation function, which does the contrast adjustment to the entire image, the CLAHE only performs the histogram equalization on smaller regions of the image in a controlled manner. On applying the regular histogram equalization function on the original image shown in Fig. 4.12, it is obvious in Fig. 4.14 that some parts of the image are oversaturated, and noises are amplified.

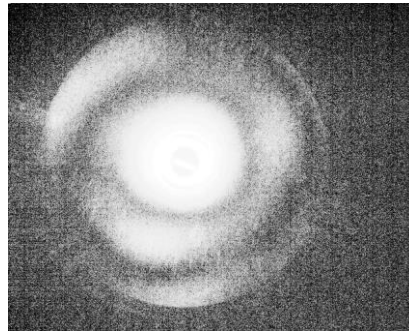


Fig. 4.14: The effect of applying the regular histogram equalization on the original image shown in Fig. 4.12.

This chapter outlined how to identify crystal types based on the features in their scattering pattern and estimate their size. The method used to simulate scattering pattern of model crystals was also discussed. In the next chapter, these are further explained using several examples.

5. MODELLING DIFFERENT TYPES OF CRYSTALS TO APPROXIMATE AIITS SCATTERING PATTERNS

As mentioned in Sections 4.4 and 4.5, the model crystals are generated using program specific to the crystal type, and the crystal orientation is represented in Euler angles (radians). The simulated scattering patterns of these models are obtained by running the 'Beam Tracing Model' program. By comparing them with the AIITS scattering pattern images and subsequent testing with different crystal sizes and orientations, crystal models are developed. The details of different crystal habits are explained in this section using various examples.

5.1 Plates

Plates usually have eight facets in total and are found orientating with their basal facets perpendicular to the laser beam. There are different types of plates, and some of them are addressed in this section.

5.1.1 Pristine, smooth hexagonal plates

The striking feature of a plate is the presence of six prominent scattering arcs in its scattering pattern. The six-fold symmetry arises from the hexagonal crystal symmetry. In the first example (Fig. 5.1), particle number 2342 in the AIITS data is shown (also in Fig. 5.2(a)).

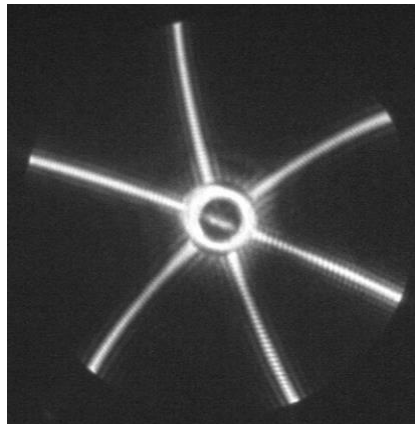


Fig. 5.1: Scattering pattern image of particle number 2342.

A model crystal and its scattering pattern, which resembles that of the AIITS pattern, are shown in Fig. 5.2(b) and (d) respectively. The crystal size was estimated as radius 40-45 μm (based on the scattering arc width) and thickness $\leq 5\mu\text{m}$ (based on patterns within the arcs). Because scattering patterns computed for thick plates show additional features like bright extra arcs, which are not visible in Fig. 5.2(a), presumably this pattern was generated by a thin plate. In the scattering pattern of a 20 μm thick plate with similar radius, but in a slightly different orientation, two additional scattering arcs which arise from the prism facets can be seen (Fig. 5.2(h)). Additionally, a higher number of minima can be seen within the six scattering arcs.

In general, all model crystals are generated in $\alpha=\beta=\gamma=0$ orientation. This is shown in Fig. 5.2 (c) using the model crystal in (b).

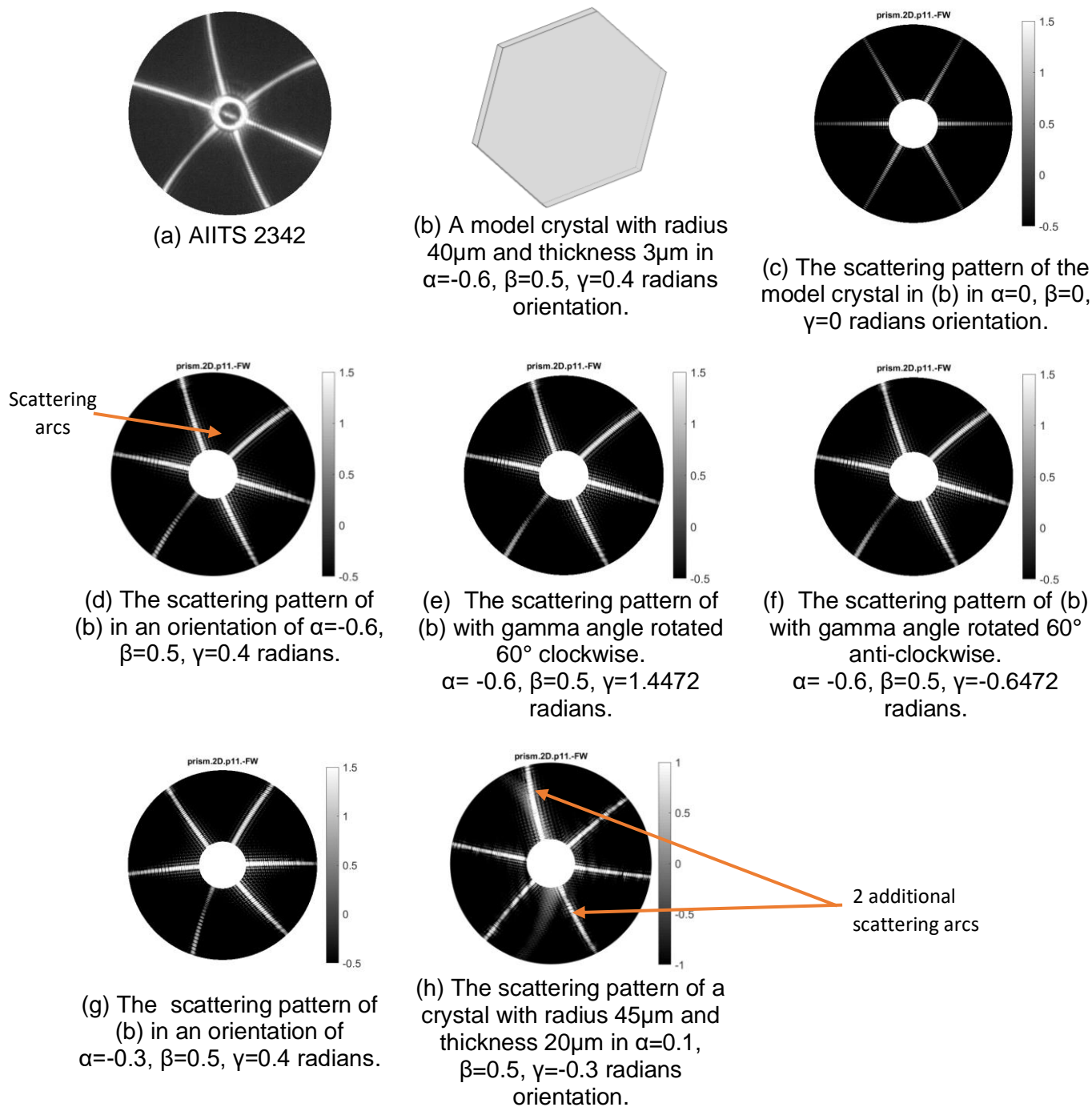


Fig. 5.2: A large, thin model plate (b) and its simulated scattering pattern (d) in comparison with the AIITS pattern (a). The same model crystal in (b) are shown in different orientations in (c-g). The scattering pattern of a thicker plate is shown in (h).

Through manual analysis of repeated runs of BTM by changing one Euler angle at a time, an optimal set of Euler angles is found. The Euler angles are selected based on the position of arcs, the direction of arc's bending as well as the width of the arcs. In this case, the optimum Euler angles were found to be $\alpha=-0.6, \beta=0.5, \gamma=0.4$ radians. When the values are slightly off the optimum values, the pattern changes. An example can be seen in Fig. 5.2 (g) where the alpha angle is changed by 0.3 compared to (d), that is, $\alpha=-0.3, \beta=0.5, \gamma=0.4$ radians.

Due to the 60° symmetry of a hexagonal prism, a particular scattering pattern can be reproduced by more than one set of Euler angles. This is shown in Fig. 5.2 (e) and (f), where the scattering pattern in (d) is replicated by rotating the crystal by 60° clockwise or anti-clockwise during the last rotation (gamma angle).

5.1.2 Hexagonal plates with rounded edges

Like the regular hexagonal plate discussed in previous section, the scattering pattern (given in Fig. 5.3) of particle number 2304 also displays six arcs. As the scattering pattern is dimmer and the arcs are wider compared to the previous one (AIITS no.2342), the scatterer is presumed to be a small hexagonal plate.

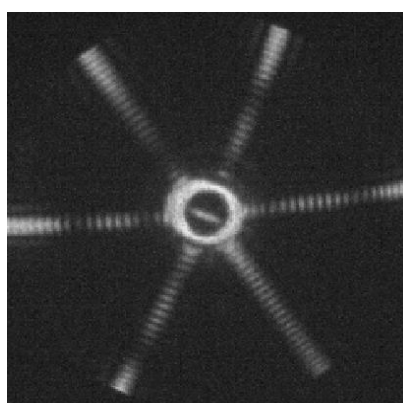
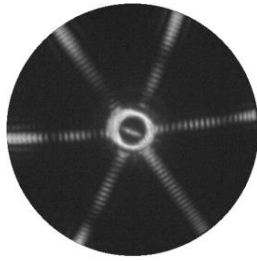
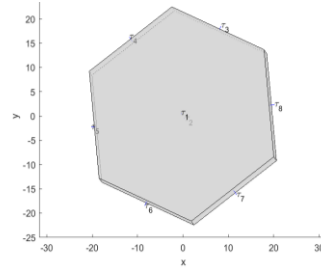


Fig. 5.3: Scattering pattern of particle number 2304 in the AIITS data.

After analysing a range of plates with different radii and thicknesses manually, crystal size was estimated based on the width of the scattering arcs. Since plates tend to orientate on their basal facets, it is almost impossible to estimate the thickness of the plate, which is out of view. However, after rigorous testing, plate models with thickness greater than or equal to radius were not used because of the increased probability of prominent additional features arising from its prism facets (like circular arcs in Fig. 5.4 (f), (g) and (h)). For plates with thickness less than the crystal radius, only six scattering arcs can be seen (Fig. 5.4 (c), (d), (e)). The edge length plays a major role in a plate crystals' scattering pattern. In a regular hexagonal crystal, both radius and edge length are equal. On decreasing the crystal radius, the width of the six prominent scattering arc increases (see for example, Fig. 5.4 (g) and (h)). Therefore, one can estimate the plate radius to be in the 20-25 μm range with thickness <20 μm (for thickness >20, prism facet features contribute like the example shown in Fig. 5.4 (g) (h)). This also rules out any likelihood of scatterer being a long column as they are found usually orientated with their long prism axis perpendicular to the laser beam. The Euler angles for the pristine hexagonal plate were found to be $\alpha=2.2$, $\beta=0.2$ and $\gamma=0$.



(a) AIITS 2304



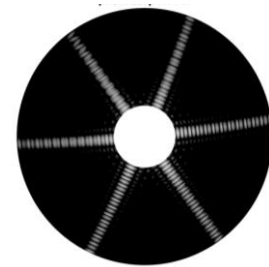
(b) A model crystal with radius $22.5\mu\text{m}$ and thickness $3\mu\text{m}$ in Euler orientation $\alpha=2.2$, $\beta=0.2$ and $\gamma=0$ radians.



(c) Radius $23\mu\text{m}$, thickness $7\mu\text{m}$



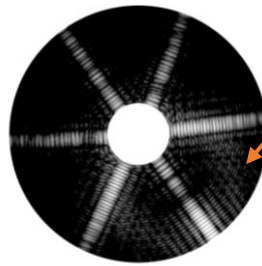
(d) Radius $20\mu\text{m}$, thickness $5\mu\text{m}$



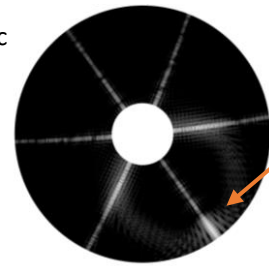
(e) Radius $23\mu\text{m}$, thickness $2\mu\text{m}$



(f) Radius $20\mu\text{m}$, thickness $20\mu\text{m}$



(g) Radius $19\mu\text{m}$, thickness $25\mu\text{m}$



(h) Radius $50\mu\text{m}$, thickness $50\mu\text{m}$

Fig. 5.4: Simulated scattering patterns of pristine plate models in comparison with AIITS pattern. Scattering patterns of thin plates (aspect ratio <0.5) and thick plates (aspect ratio ≥ 0.5) can be seen in (c), (d), (e) and (f), (g), (h) respectively.

Model crystals, with some rounding factors introduced to the above pristine plates, were also tested using another algorithm [E. Hesse, private communication], which takes the following input:

- i. Radius of the hexagonal plate.
- ii. Thickness (length) of the hexagonal plate.

- iii. Rounding factor for cylinder radius (f) or semi-minor axis length, value ranges between 0.867 (perfectly round) and 1 (no rounding or pristine hexagon).¹⁴
- iv. Number of rectangular sub-sections (n) parallel to the cylindrical axis.¹⁵
- v. Rounding factor for cylinder length (ff), value between 1.05(round) and 1.41(pristine), semi-major axis length or half the major axis length.¹⁶
- vi. Number of trapezoidal sections (s) which ranges between 1 and 10, (ellipsoid section replacing a corner is divided into s trapezoidal subsections).¹⁷

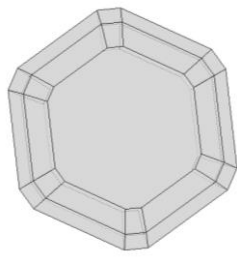
(The alpha angle of Euler orientation for rounded crystal is rotated by 90 degrees compared to pristine plates generated using 'Column_Plate' algorithm, therefore this should be subtracted, and the new set of Euler angle is $\alpha=0.629$, $\beta=0.2$, $\gamma=0$ in radians). A range of rounding factors were tested. Fig. 5.5 (a) shows an example of a rounded plate crystal with radius 22.5 μm , thickness 4 μm and rounding factors $f=0.95$, $n=1$, $ff=1.35$, $s=2$ and its scattering pattern (Fig. 5.5 (b)), which shows a much better agreement with the AIITS pattern (Fig. 5.5 (d)), than the patterns computed for pristine plate in (Fig. 5.5 (f)). Therefore, it is assumed that the scatterer is a plate crystal with slightly rounded edges. Even though the same rounding factors are used for another model crystal, the scattering pattern shows fringes or ring-like structure (see Fig. 5.5 (c)). This is because the thickness of model crystal is different and on applying the rounding factors, the overall shape of the crystal is changed. The scattering pattern of yet another model crystal with different rounding factors $f=0.95$, $n=1$, $ff=1.35$, $s=4$ is shown in (Fig. 5.5 (e)), in which a few ring-like structure can be seen. In comparison, the AIITS pattern (Fig. 5.5 (d)) is less rounded than the scattering pattern of model crystals shown in Fig. 5.5 (c) and (e).

¹⁴ These limits of the rounding factor correspond to inner circle and circumcircle of the hexagonal facet, respectively. The intersection lines of the prism with the circular cylinder of the corresponding radius are determined.

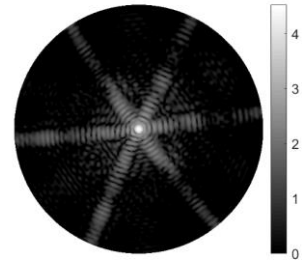
¹⁵ The new boundary of the prism between two such intersection lines is defined by n new rectangular facets of equal size, with vertices positioned on the upper and lower edges of the circular cylinder.

¹⁶ These limits of the rounding factors correspond to inner ellipse and circum-ellipse of the largest rectangular cross section through the prism containing the prism axis. The intersection points of this rectangular cross section with the ellipse are determined.

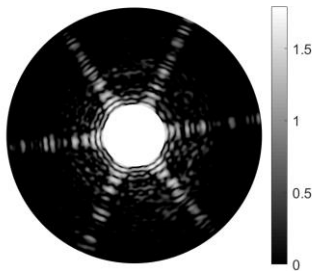
¹⁷ The new boundary of the prism between two such intersection points is defined by s equidistant points, which are positioned on the ellipse.



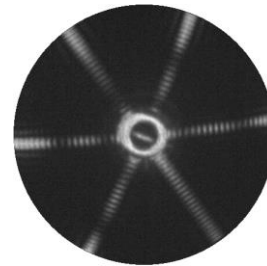
(a) A model crystal of radius $22.5\mu\text{m}$, thickness $4\mu\text{m}$, rounding factors (f 0.95, n 1, ff 1.35, s 2) with Euler angles: $\alpha=0.629$, $\beta=0.2$ and $\gamma=0$ radians.



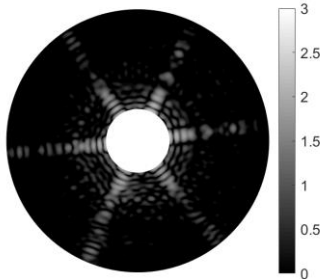
(b) The scattering pattern of the corresponding model crystal in (a). The maxima and minima show good agreement with those of AIITS in (d).



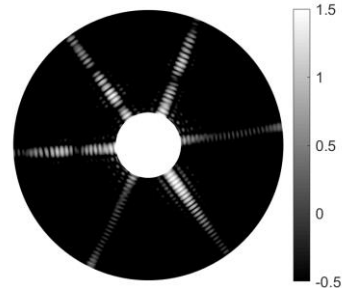
(c) Radius $23.5\mu\text{m}$, thickness $21.5\mu\text{m}$ and rounding factors (f 0.95, n 1, ff 1.35, s 2).



(d) AIITS 2304



(e) Radius $23.5\mu\text{m}$, thickness $6\mu\text{m}$ and rounding factors (f 0.95, n 1, ff 1.35, s 4).



(f) Radius $22.5\mu\text{m}$, thickness $4\mu\text{m}$ pristine hexagonal plate.

Fig. 5.5: Simulated scattering pattern of rounded plate models in comparison with AIITS pattern.

The highlighted plate in Fig. 5.6 looks very similar to the model presented in this section. The picture is taken from Tape (1994) and has been enhanced to provide a better view of the crystals. The ice crystals, shown in the picture, were collected on 4th January 1985 at the South Pole during a halo display. Note that the halo crystals possess diameters close to or exceeding $200\mu\text{m}$, considerably larger than those of the model crystals.

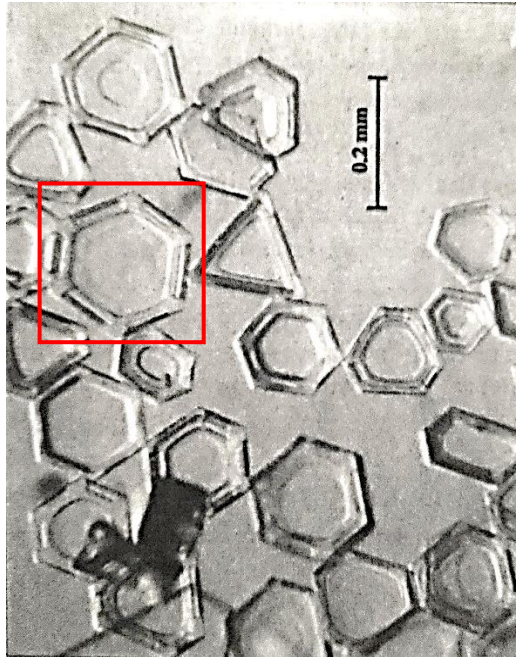


Fig. 5.6: An enhanced picture of ice crystals collected during a halo display at the South pole on 4 January 1985 taken from Tape (1994). A plate similar to the modelled crystal is highlighted in red.

5.1.3 Scalene plates

Consider Fig. 5.7. Six arcs are evident but two are much less prominent than the others (possibly) indicating a plate crystal with semi-regular hexagonal geometry. The process of modelling such a crystal is detailed below.

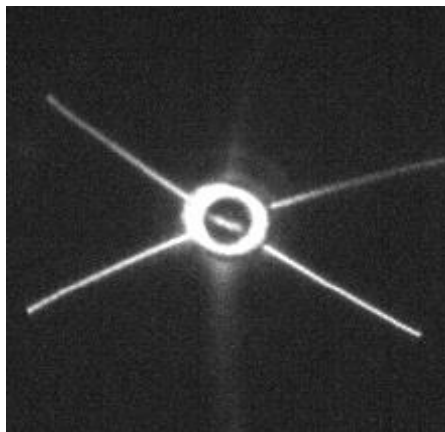


Fig. 5.7: Scattering pattern of particle number 2308 in the AIITS data.

The original algorithm could only generate a regular hexagonal plate with equal sides. This has been edited to incorporate sides with 2 shorter edges to make it scalene (semi-regular hexagon). The modified program takes an additional input: *edge_factor* (EF) which is a dimensionless factor. As ice crystals tend to retain their hexagonal structure, we wanted to avoid disrupting its internal 120-degree angle between 2 adjacent sides. The idea was to extend four sides (as depicted in Fig. 5.8).

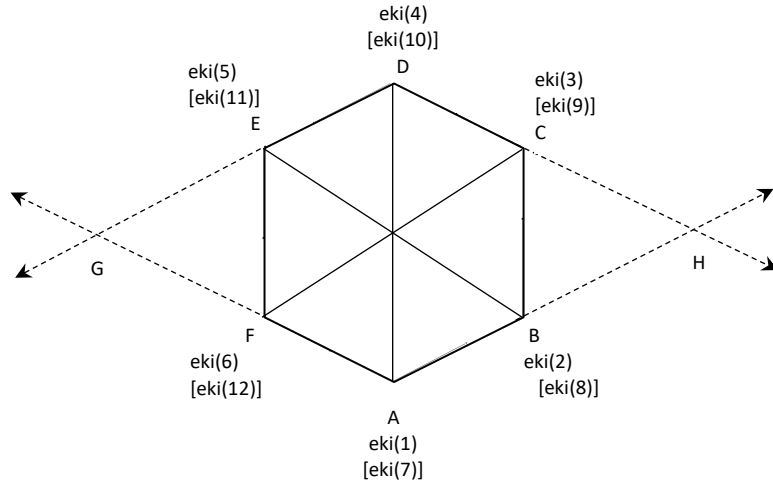
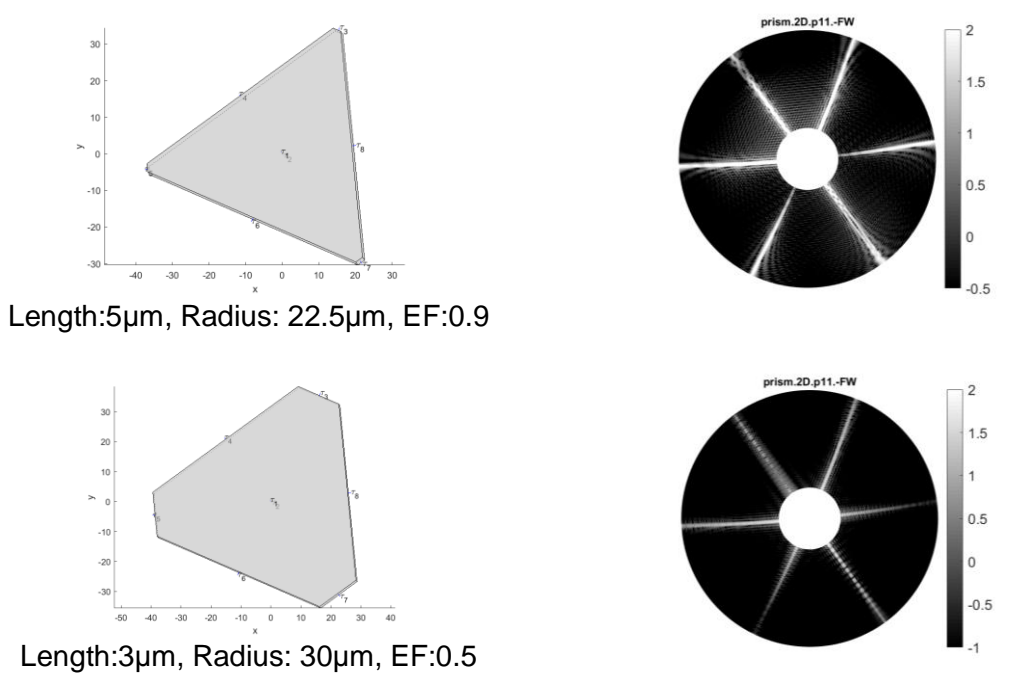
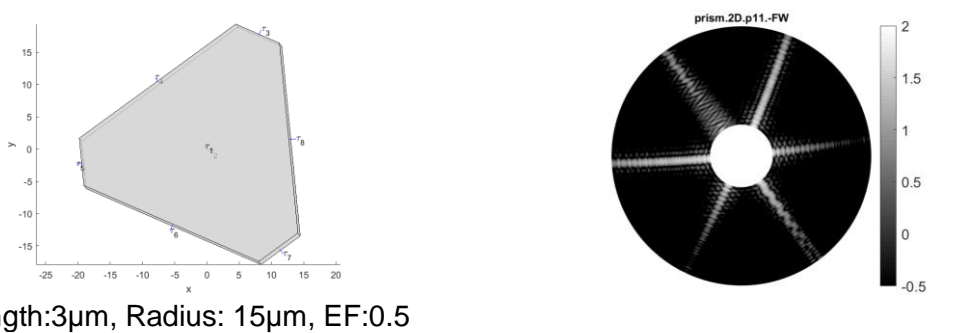


Fig. 5.8: Diagram of changing a hexagonal crystal to a rhomboidal one.

By making use of edge_factor (EF=factor times the edge length added to the original length), the desired length was acquired. The factor ranges between 0 (no effect: regular hexagon) and 1 (extreme point: creating a diamond or rhomboid shape). As EF increases, the crystal becomes more elongated (up to four longer sides). In the algorithm, the six vertices A to F were assigned eki (1) to eki (6) for top basal facet and eki (7) to eki (12) for bottom basal facet. The eki are position vectors (a set of 3 co-ordinates namely ek1, ek2 and ek3) corresponding to x, y and z values. The co-ordinates of the new points were calculated using vector algebra. For example, point H (in a rhomboid crystal with EF=1 in Fig. 5.8) can be found by, $H = ek(2) + \text{Edge Factor} \times (ek(2) - ek(1))$. This makes the vertices B and C to converge at H. Similarly, this algorithm was further edited to create the more common scalene plates (with three short and three long edges or three-fold symmetry) shown in Fig. 5.9. The existence of such crystals is noted in Murray *et.al* (2015).





Length:3 μ m, Radius: 15 μ m, EF:0.5

Fig. 5.9: Models of plates with three-fold symmetry (left) and their corresponding simulated scattering patterns (right). All crystals are in $\alpha=2.2$, $\beta=0.2$ and $\gamma=0$ orientation.

The Fig. 5.10 shows a more detailed transformation from regular hexagonal (solid blue) to a semi-regular hexagonal (red dot and line) and further to a rhomboidal crystal (green dash). The equations used to find the edge lengths and long radius of the semi-regular hexagonal prisms, based on Fig. 5.10 are given below:

Long Edge (LE): The long edge, $AB = \text{Hexagonal Radius} + EF \times \text{Hexagonal Radius}$.

Short Edge (SE): $BC = \sin 30^\circ \times AB$, since ACB is a right-angled triangle.

$$OC = BO - BC, \text{ where } BO \text{ is the Hexagonal Radius.}$$

The short edge, $AE = 2 \times AD$ (since $AD = OC$)

Long Radius (LR): $ED = AD = \frac{AE}{2}$

$$OD = \left[\frac{\sqrt{3}}{2} \text{Hexagonal Radius} + EF \frac{\sqrt{3}}{2} \text{Hexagonal Radius} \right] = \frac{\sqrt{3}}{2} AB$$

The long radius, $OE = \sqrt{ED^2 + OD^2}$

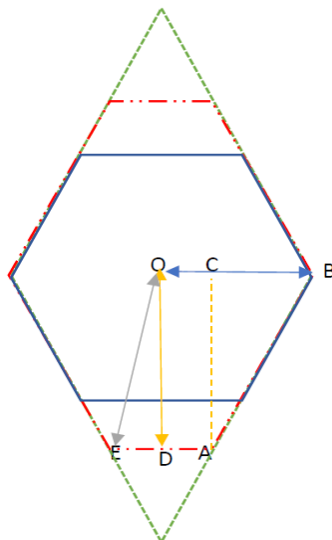
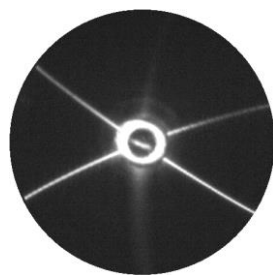


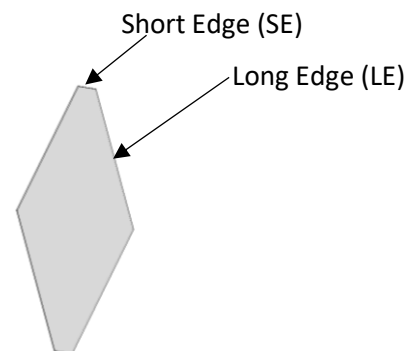
Fig. 5.10: Three different crystal geometries are shown: the pristine regular hexagon (blue solid line) with hexagonal radius (OB), semi-regular hexagon (red dot and line) and a rhomboid (green dash).

The model crystal (in Fig 5.11 (b)) has a hexagonal cross-section with 4 long and 2 short sides. The four bright and the two faded arcs in the AITS image (Fig 5.11 (a)) are linked to the 4 long edges and 2 short edges of the semi-regular hexagonal plate respectively (the hexagonal shape can be considered as three sets of parallel edges, i.e., two sets of long edges and one set of short edges).

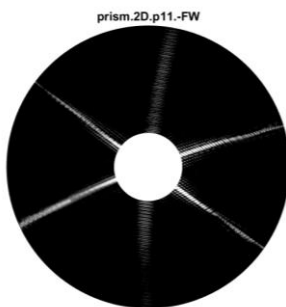
The next step is to find the correct crystal orientation specified in terms of the Euler angles. Fig 5.11 shows simulated scattering patterns using different sets of Euler angles and crystal sizes. The patterns in Fig 5.11 (c), (d) and (e) look almost the same, but 3 different sets of Euler angles are used (whose sum of alpha and gamma is equal to 1.45). However, on careful inspection one can see that the arc running from top left to bottom right straightens up with increasing gamma and decreasing alpha, while beta angle is kept constant. Therefore, the 4 major arcs find a middle ground at $\alpha=-0.2$, $\beta=0.4$ and $\gamma=1.65$.



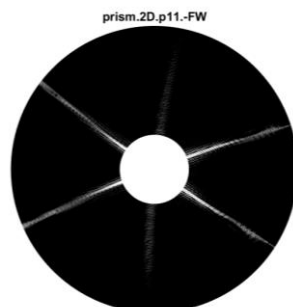
(a) AITS 2308



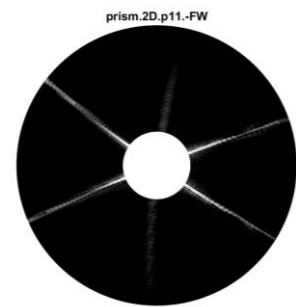
(b) A model crystal with Rad45, len2, $\alpha=-0.2$, $\beta=0.4$, $\gamma=1.65$, EF 0.7, SE:13.5, LE:76.5



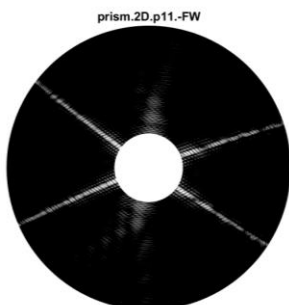
(c) Rad40, len5, $\alpha=-0.45$, $\beta=0.4$, $\gamma=1.9$, $\alpha+\gamma=1.45$, EF 0.6, LE:64, SE:16, LR:56



(d) Rad50, len5, $\alpha=-0.2$, $\beta=0.4$, $\gamma=1.65$, $\alpha+\gamma=1.45$, EF 0.6, LE:80, SE:20, LR:70



(e) Rad50, len5, $\alpha=0$, $\beta=0.4$, $\gamma=1.45$, $\alpha+\gamma=1.45$, EF 0.6, LE:80, SE:20, LR:70



(f) Rad35, len18, $\alpha=-0.2$, $\beta=0.4$, $\gamma=1.65$, EF 0.65, LE:58, SE:12, LR:50.38



(g) Rad45, len2, $\alpha=-0.2$, $\beta=0.4$, $\gamma=1.65$, EF 0.7, LE:76.5, SE:13.5, LR:66.59

Fig. 5.11: Forward scattering pattern of different crystal sizes in comparison with AITS 2308.

Looking at the scattering arc's width, the long edge can be estimated between 55-80 μm and short edge between 10-14 μm . In this case too, the thickness of the plate should be less than half the regular hexagonal plate radius. Otherwise, additional features will become prominent in the scattering pattern (Fig. 5.11 (f)). The scattering pattern of the model crystal (Fig. 5.11 (g)) shows a good agreement with the AITS pattern. Existence of such (scalene) semi-regular hexagonal plates are recorded in Tape (1994). One such sample of crystals collected during a halo display at South Pole is given in Fig. 5.12, which includes plates ranging from rhomboid to regular hexagonal symmetry.

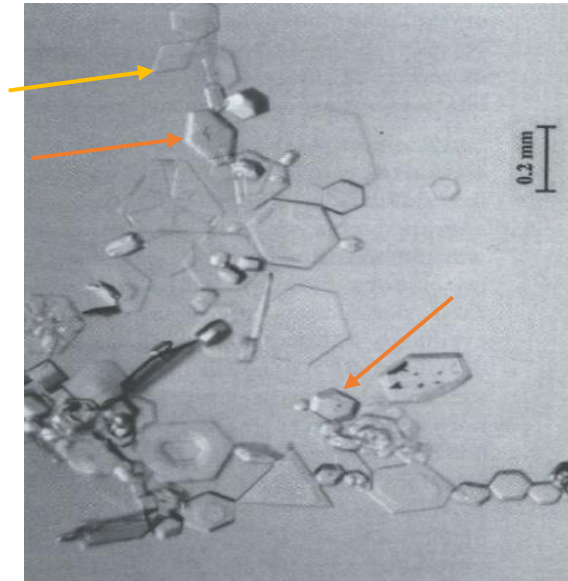


Fig. 5.12: Ice crystals collected during a halo display at the South pole on 2 January 1990 (Tape 1994). Semi-regular and rhomboid crystals are shown in orange and yellow arrows respectively.

From the scattering pattern of the modelled plate crystal, altogether, six scattering arcs were seen and the width of the scattering arc was highly dependent on the edge length of the plate. Increased edge length results in narrow scattering arcs. This agrees with far-field diffraction in which the diameter of the slit (or object) is inversely proportional to the angle of diffraction. Therefore, the larger the particle, the smaller will be the divergence of the diffracted beam. In hexagonally symmetric crystals, the width of all the six scattering arcs were the same, whereas in semi-regular hexagonal plates or scalene plates, there were manifestations of scattering arcs of dissimilar width. Estimating the particle size in terms of edge length (both long and short edges) is highly recommended for scalene plates (as edge length is not equal to radius). While estimate can be made either by radius or edge length for regular hexagonal plates (as edge length is equal to radius).

5.1.4 Droxtals

Droxtals are a variant of plates with tapered upper and lower prism sections. Consequently, droxtals have 20 facets while plates only have eight (Yang *et al.* 2003). A microscopic photograph of a droxtal taken from Kikuchi *et al.* (2013) and a model droxtal with 20 faces are shown in Fig. 5.14 (d) and (f). They are formed by direct freezing of supercooled liquid droplets with little growth directly from the vapour (AMS Glossary of Meteorology, 2012). So far, the scattering patterns of different varieties of plates were discussed. The scattering patterns of droxtals show a similar appearance to that of plates; however, the former have bright spots or halos in addition to the scattering arcs. The number and position of bright spots depends on the crystal orientation. There were a few AITS images which appeared to be the scattering pattern of droxtals. One such example is shown in Fig. 5.13.

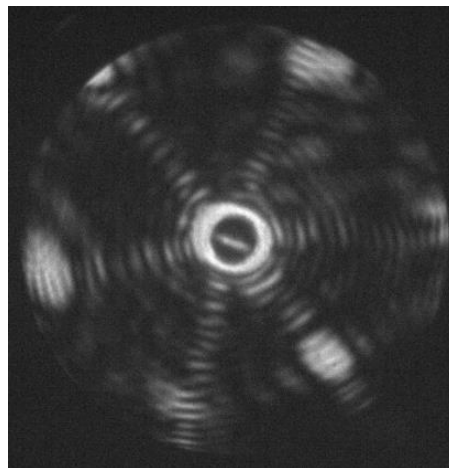
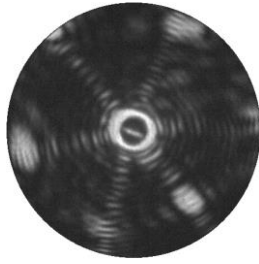
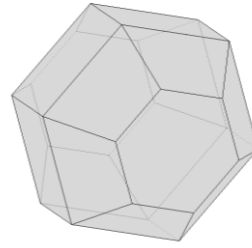


Fig. 5.13: Scattering pattern image of particle number 2315 in the AITS data.

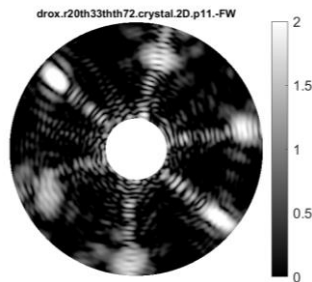
A droxtal with radius $20\mu\text{m}$ and an aspect ratio nearly equal to unity (height or length: $33.6\mu\text{m}$) is shown in Fig. 5.14 (b). This model was found to be a good approximation for the scatterer of the pattern (in Fig. 5.14 (a)), in an orientation of $\alpha=-0.6$, $\beta=0.5$, $\gamma=0.4$ radians. The simulated pattern (Fig. 5.14 (c)) contains features like scattering arcs, concentric rings as well as bright spots, all in the right places. The droxtal has an estimated radius of $15\text{-}20\mu\text{m}$ and length $25\text{-}34\mu\text{m}$. Though features like scattering arcs and bright spots are usual appearance for droxtals, the concentric ring like feature may not be evident in some orientations like the one in Fig. 5.14 (f).



(a) AIITS 2315



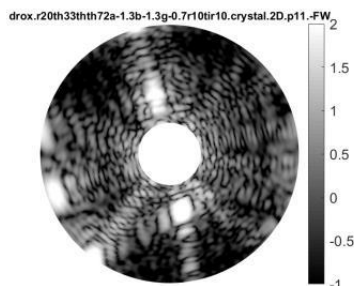
(b) A droxtal with radius $20\mu\text{m}$ and length $33.6\mu\text{m}$, $\alpha=-0.6$, $\beta=0.5$, $\gamma=0.4$ radians



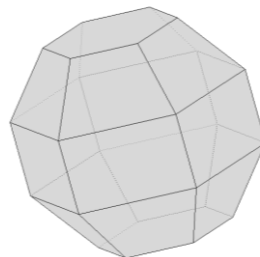
(c) The simulated pattern of the model crystal in (b)



(d) Microscopic photograph of a droxtal taken from Kikuchi *et al.* (2013)



(e) The simulated pattern of the model crystal in (f)



(f) A droxtal with radius $20\mu\text{m}$ and length $33.6\mu\text{m}$, $\alpha=-1.3$, $\beta=-1.3$, $\gamma=-0.7$ radians

Fig. 5.14: Model of a droxtal and its simulated scattering pattern in comparison with the AIITS pattern

In addition to regular droxtals, those of scalene nature were tested. The simulated pattern of a model crystal with radius 20 μm and height 40 μm showed a greater resemblance to particle number 2337 (Fig. 5.15).

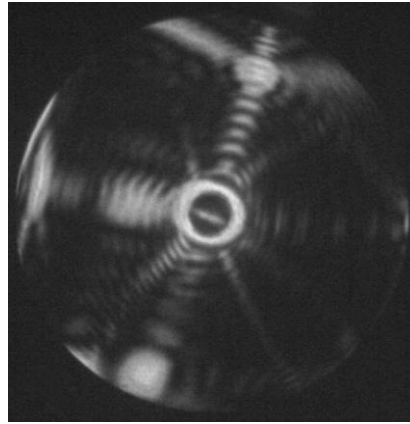


Fig. 5.15: Scattering pattern of particle number 2337 in the AIITS data.

An enhanced image is shown in Fig. 5.16 (a) for a better view of its minor arcs. The striking features that match the AIITS image with the simulated scattering pattern are the major and minor arcs (wider and thinner arcs), and the three halo-like features on the central cross-like arc. The vertical and horizontal arcs forming a cross-like structure was indicative that both the diameter and height of the crystal might be roughly the same. The orientation of the droxtal was found to be $\alpha=1.3$, $\beta=-1.3$, $\gamma=0.7$ radians after testing with several orientations.

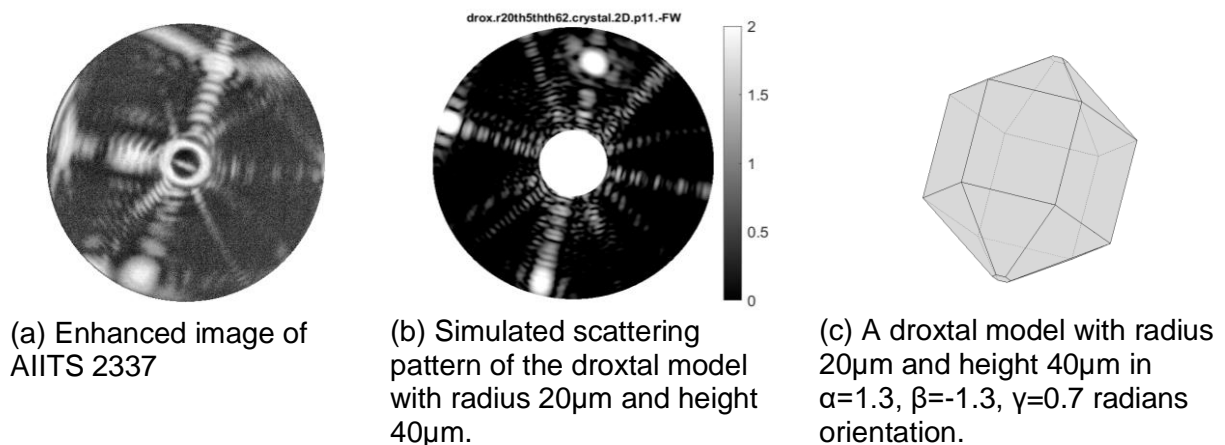
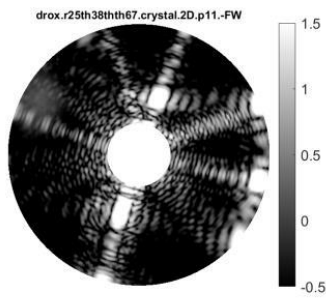
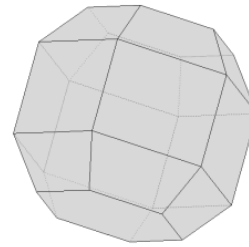


Fig. 5.16: (a) AIITS pattern, (c) a model crystal of droxtal and (b) its simulated pattern.

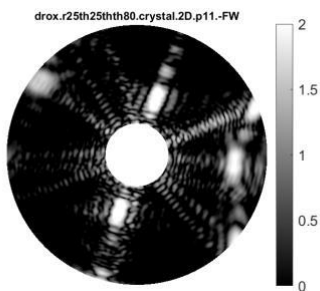
Several variations of scalene droxtals were tested like the examples in Fig. 5.17. Since the models shown are in the same orientation of $\alpha=1.3$, $\beta=-1.3$, $\gamma=0.7$ radians, the positions of arc are also nearly in same places as in Fig 5.16 (a); however, the halos are in different places which might be due to the difference in tilt angles of the facets. The simulated pattern shown in Fig 5.16 (b), shows the closest resemblance to that of Fig 5.16 (a), and the scalene droxtal has an estimated radius of 20-25 μm with height=2 x radius.



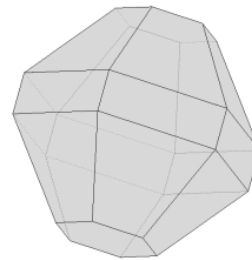
(a) Simulated scattering pattern of the droxtal model in (b).



(b) A droxtal model with radius 25µm and height 48µm.



(c) Simulated scattering pattern of the droxtal model in (d).



(d) A droxtal model with radius 25µm and height 50µm.

Fig. 5.17 (b) and (d): Model crystals of scalene droxtals; (a) and (c): their respective simulated patterns.

5.2 Columns

Columns are hexagonal prisms like plates, but unlike plates, they orientate with their prism axis perpendicular to the laser beam. There are different varieties of columns, like solid or hollow columns, and they can be thick or thin with smooth or rough surfaces. Columns with very high aspect ratio are referred to as needles (see Section 5.2.3).

5.2.1 Smooth solid columns

Smooth columns are those with a smooth surface texture. The scattering pattern of such crystals display two scattering arcs (a major central arc) with or without accompanying parallel lines. The AITS image number 2351 (Fig. 5.18 (a)) appeared to be the scattering pattern from a column crystal. Therefore, smooth columns of several sizes were tested and the scattering pattern from a model crystal (Fig. 5.18 (b)) with radius 10µm and length 25µm was found to be a match. On testing, the model crystal was found to be in $\alpha=2.8$, $\beta=-1.3$ and $\gamma=-0.7$ radians' orientation. It was understood that as the column becomes longer (increasing length or growing on its prism axis), the width of the central arc decreases and as the column gets wider (increasing diameter or growing on its basal axis), the number of minima within the arc increases (as long as diameter \leq length). Based on this, the crystal was found to have an estimated basal radius of 2-10µm and prism length of 20-30µm.

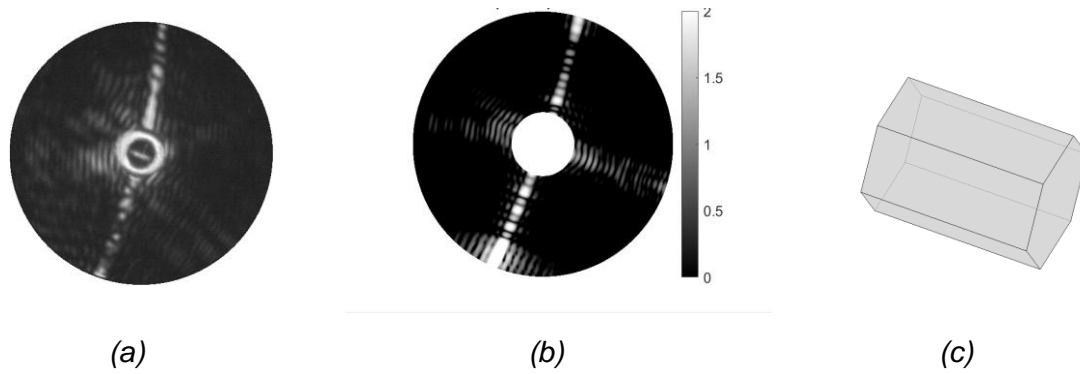


Fig. 5.18: (a) AIITS pattern number 2351, (c) the model crystal of a smooth solid column with radius $10\mu\text{m}$ and length $25\mu\text{m}$, and (b) its simulated pattern.

5.2.2 Rough solid columns

A rough column, as the name implies, has a rough texture on its surface. In the scattering pattern of such a crystal, speckle-like feature will be evident as with any rough crystal. In addition, solid column's feature of major central arc will also be visible. On analysing the AIITS image number 1906 (Fig. 5.19 (a)), a combination of speckles as well as the major central arc were seen, which indicates that the crystal is a rough solid column. The crystal size was estimated to have a basal radius $10\text{-}15\mu\text{m}$ and prism height of $30\text{-}40\mu\text{m}$ after testing with different column sizes with varied surface roughness. As with smooth solid column, the rough column's central arc become wider in the scattering pattern, as the column length gets shorter, and fewer number of minima will be seen inside the arc. As discussed in Section 4.5.1, the speckle size is inversely proportional to the crystal size. The model crystal and its simulated pattern are in orientation: $\alpha=0.5$, $\beta=1.2$ and $\gamma=0.2$ radians (Fig. 5.19 (c) and (b)).

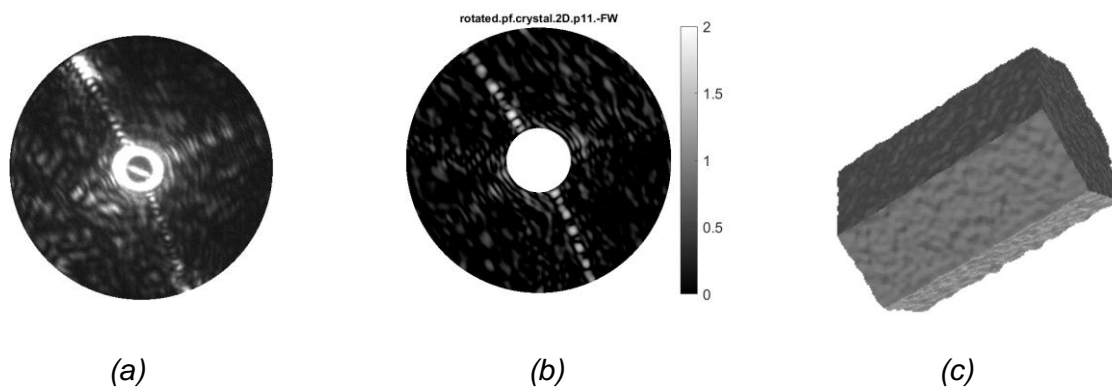


Fig. 5.19: AIITS pattern number 1906 (a), the model crystal of a rough solid column with radius $10\mu\text{m}$ and length $30\mu\text{m}$ (c) and its simulated pattern (b).

5.2.3 Needles

Needle crystals are column-like crystals that are extremely thin. Fig. 5.20 shows the scattering pattern of such a crystal.

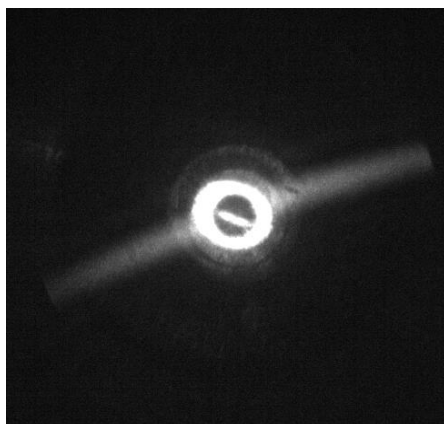


Fig. 5.20: The scattering pattern image of particle number 1122 in the AIITS data.

Fig. 5.21 (b) and (c) show a model crystal with radius $0.5\mu\text{m}$, length $13\mu\text{m}$, and its corresponding scattering pattern respectively. This pattern is the best fit obtained. The process to obtain it was as follows: Since the scattering pattern exhibits the properties of a long column (orientating on its long prism axis), a column crystal was generated first. After a sequence of testing with different crystal sizes and Euler angles, a model crystal was developed. It was understood that the width of the scattering arc increases as the crystal length decreases, and by increasing the radius of the crystal, a greater number of minima (dark bands) will be visible in the pattern.

The crystal length was estimated based on the width of the scattering arcs, and its radius, based on the presence/absence of minima. For crystals with radius $\geq 1\mu\text{m}$, minima will be present within the central arc of the scattering pattern. One such example is shown in Fig. 5.21 (d). As column radius increases, greater number of minima will be visible. Likewise, when the length of the column is increased, the width of the central arc decreases. As AIITS can only detect crystal sizes with diameter $\geq 1\mu\text{m}$, the lower range was ignored. The only radius which displayed similarity was $0.5\mu\text{m}$. Therefore, the crystal type was identified as needle like crystal with an estimated basal radius $0.5\mu\text{m}$ and prism height of $10\text{-}20\mu\text{m}$.

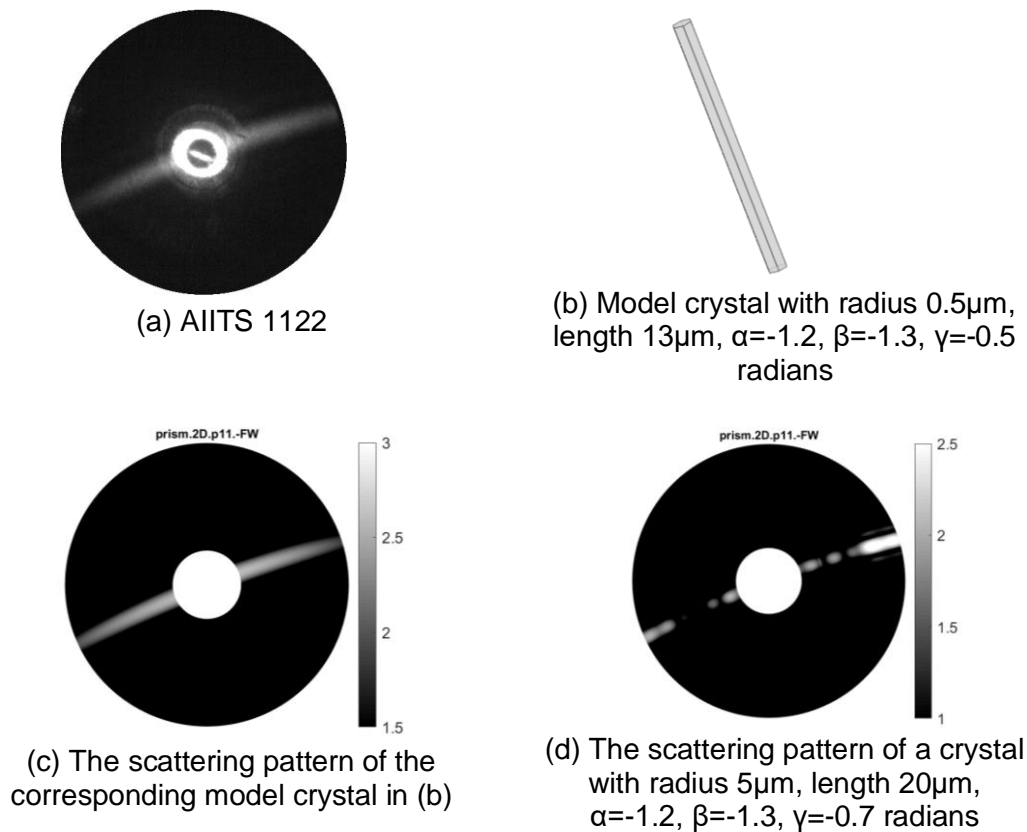


Fig. 5.21: Simulated scattering pattern (c) of thin solid column model (b) in comparison with the AIITS pattern (a). The scattering pattern of a thicker column is shown in (d).

According to Lee and Magono (1966), microscopically needle-like crystals can be further classified as:

1. Extremely thin solid columns.
2. Extremely thin hollow columns (called Sheaths).
3. Needle-like structure with a pointed or knife edged tip.

The model crystal belongs to the first category, or type 'N1e needle crystal' according to the nomenclature in Lee and Magono (1966). Based on observations noted in Lee and Magono (1966), these types of crystals are formed at temperature below -30°C ; however, it was also noted that these types of crystals can be experimentally obtained around -50°C . It is also mentioned that "minute solid columnar crystals are frequently observed in the early stage of mature columnar crystals" (Lee and Magono 1966). Examples of thin solid columns are shown in Fig. 5.22.

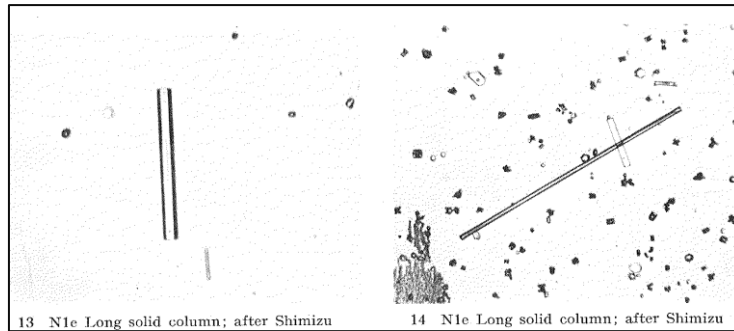


Fig. 5.22: Microscopic photographs of thin solid columns from Lee and Magono (1966).

5.3 Quasi-spheroids

Quasi-spheroidal crystals are crystals with significantly rounded edges and an aspect ratio close to unity. The striking feature in the scattering pattern of this type of crystal is the presence of a ring-like structure. Based on the number of rings and the ring's width, it is possible to estimate the crystal radius. A perfectly spherical crystal has a diffraction pattern with concentric intensity peaks very similar to that of water droplets. Two types of quasi-spheroids were observed in the AITS images: smooth and rough. The smooth quasi-spheroids only contained ring-like structure in its scattering pattern, while the rough quasi-spheroids displayed the same with an additional speckle-like pattern.

In general, the models of Quasi-spheroid crystals are generated using the *gsphere* (Muinonen *et al.* 1996) program with specific radiuses, and the scattering patterns are simulated using Hesse *et al.* (2018) Beam Tracer method. Since there is a relationship between the number of rings and the crystal size, the number of rings is counted from the 2D simulated patterns for each crystal size. The larger the crystal, the more rings are visible in the scattering pattern. As an example, a model of smooth sphere of radius 10 μm along with its simulated 2D scattering pattern is shown in Fig. 5.23. For this sized crystal, 8-12 rings are visible in the scattering pattern plotted between 6° - 25° . Likewise, different sized crystals are tested to find the number of rings, and the results are given in the last column of Table 5.1.

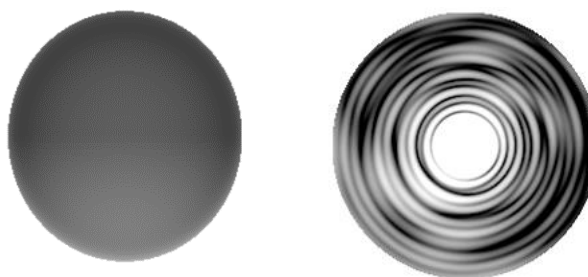


Fig. 5.23: A model of smooth sphere with radius 10 μm (left) and its simulated 2D scattering pattern (right).

For validation, the number of rings visible in the simulated 2D scattering pattern is compared with the phase function generated using both the Mie and Beam Tracer program. This is given in the second and third column of the Table 5.1. The phase function provides a plot of the azimuthally integrated P11 element of the scattering matrix, which corresponds to intensity, versus the scattering angle. As an example, the phase function of smooth sphere of radius 10 μm created using Mie program and Beam Tracer program are given in Fig. 5.24 for a side-to-

side comparison. 10 peaks can be seen in the phase function plot generated via Mie program and 11 peaks can be counted from the Beam Tracer-generated phase function plot.

Radii (μm)	Mie: Number of intensity peaks in P11 (6° - 25°)	Beam Tracer: Number of intensity peaks in P11 (6° - 25°)	Beam Tracer: Number of rings visible in the 2D scattering pattern (6° - 25°)
5	5	5	5-6
10	10	11	8-12
15	14	15	12-17
20	19	20	17-20
25	24	26	20-24

Table 5.1: The number of bright diffraction rings or intensity peaks in different sphere radiuses.

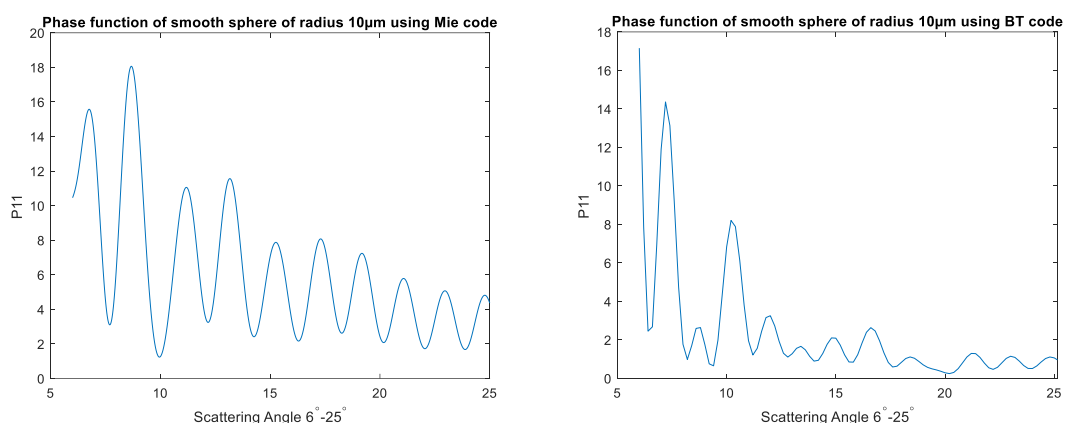


Fig. 5.24: The phase function of a smooth sphere with radius $10\mu\text{m}$ generated using Mie program (left) and BT program (right).

In general, the number of intensity peaks in the phase function or the rings in the 2D scattering pattern increases with increasing crystal radius. On comparing the number of intensity peaks in the phase function plot of Mie and Beam Tracer program, only ± 2 difference can be seen. Note that, a maximum of 22 rings were spotted in the AIITS images of quasi-spheroids. Hence, the Table 5.1 contains information of the radius up to $25\mu\text{m}$. With the help of this table, the radius of crystals is estimated by counting the number of rings in the AIITS images. Also note that the information provided here is for forward scattering pattern of 6° - 25° . Obviously, the number of rings increases if the forward scattering pattern covers more than this region.

So far, the process of estimating the radius of a quasi-spheroidal crystal from its scattering pattern were discussed. Let us look at some of the AIITS example images next.

The AIITS scattering pattern of a smooth quasi-spheroid crystal is shown in Fig. 5.25 (a) and about 5-8 prominent rings are visible. In comparison, the simulated scattering pattern of the model crystal with radius $5\mu\text{m}$ shown in Fig. 5.25 (c) has 4-5 rings and therefore smaller than the one in AIITS pattern. The crystal size is therefore estimated as 5-10 μm in radius. It is obvious that the model is too spherical compared to the AIITS pattern; nevertheless, for an approximate size estimation, the model is deemed to be sufficient. The actual crystal is likely

to have a slightly oval shape with rounded edges (and not perfectly spherical as in the model). The model crystal in correct orientation and its side view are shown in Fig. 5.25 (b) and (d) respectively.

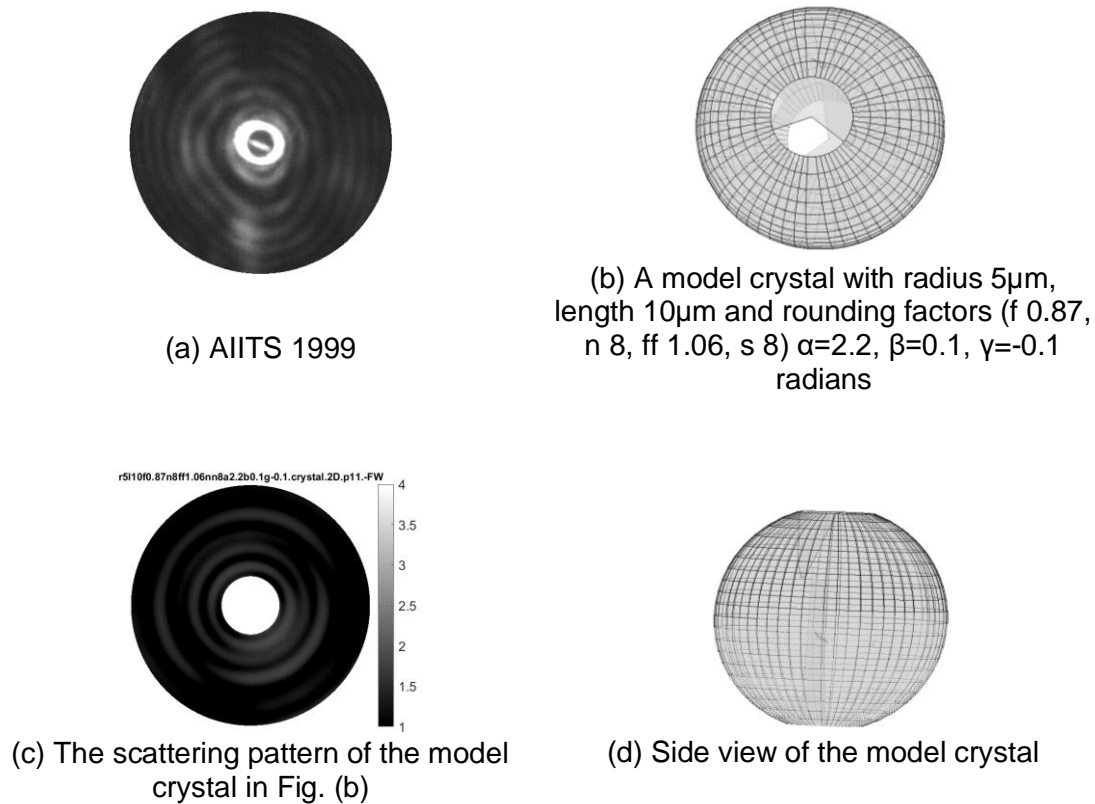


Fig. 5.25: (b) and (d): Quasi-spheroid model and simulated scattering pattern (c) in comparison with the AIITS pattern (a).

To replicate the AIITS pattern, equiaxed (approximately equal in diameter and length) model crystals are used.

In the next example, Fig. 5.26 (a), image number 2411 in the AIITS dataset is shown, in which around 12-14 rings can be seen. This is also a quasi-spheroidal crystal as the previous one, but a greater number of rings indicates that the crystal is bigger. Also, some speckle-like feature can be seen indicating that this is a rough quasi-spheroid. The model crystal has a radius and length of $15\mu\text{m}$ and $25\mu\text{m}$ respectively, with rounding factors of $f=0.87$, $n=8$, $ff=1.06$, $s=8$. Rounding factors were explained in Section 5.1.2. In Fig. 5.26 ((c) top row) and (b), the original crystal orientation which was found to be $\alpha=2$, $\beta=0.1$, $\gamma=0$ radians as well as its simulated scattering pattern are shown. The side view of the model crystal is given in the bottom row of (c). Estimated size of this quasi-spheroid is 10-15 μm radius. The roughness of the crystal was computed as 0.5073 based on the method described in Section 4.5.2.

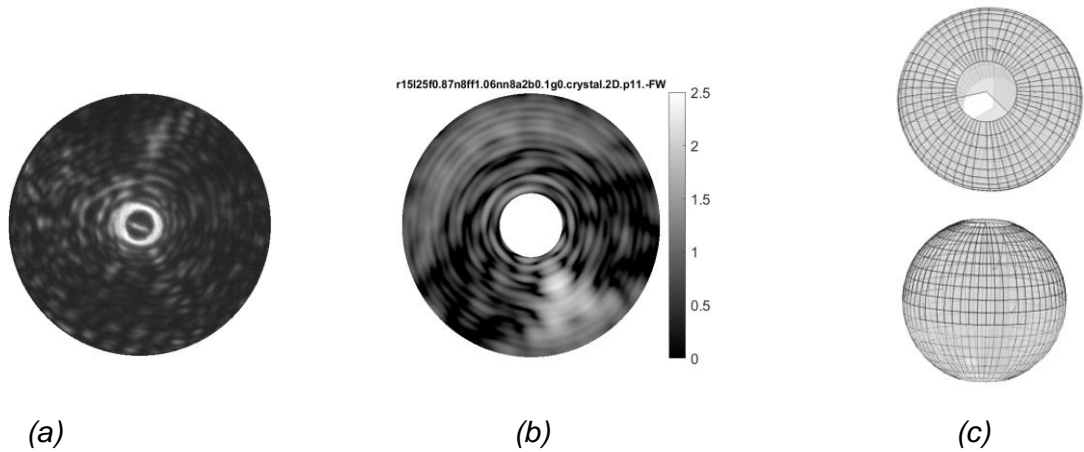


Fig. 5.26: (a) The AITS image number 2411, (c) a model crystal with radius $15\mu\text{m}$ and length $25\mu\text{m}$ rounding factors (f 0.87, n 8, ff 1.06, s 8) in correct orientation (top) and its side view (bottom), and (b) the simulated pattern of the model crystal in correct orientation.

In general, for both smooth and rough quasi-spheroids, the crystal sizes were calculated based on the number of rings visible in their scattering pattern. For rough quasi-spheroids, additionally the roughness of the crystal was computed using the Combined Roughness program.

5.4 Rough crystals

For some rough crystal morphologies, despite the scattering patterns being dominated by speckle, shape information is still visible. For example, Fig 5.27 presents the scattering pattern of a rough column with radius $20\mu\text{m}$ and length $50\mu\text{m}$, where the distinct horizontal arc can be clearly seen.

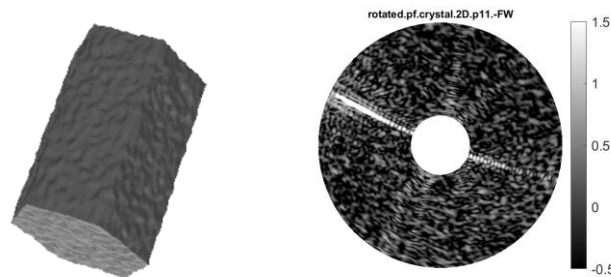


Fig. 5.27: A rough solid column model of radius $20\mu\text{m}$ and length $50\mu\text{m}$ (left) and its simulated scattering pattern (right).

Another example is given in Fig. 5.28. Six prominent arcs can be seen distinctly in the scattering pattern of a rough, thin plate of radius $50\mu\text{m}$ and length $40\mu\text{m}$, along with the speckles.

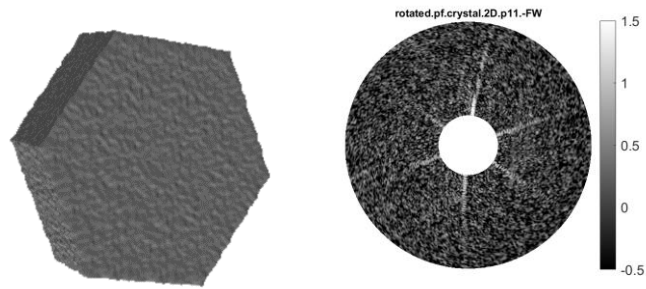


Fig. 5.28: A rough, thin plate model of radius $50\mu\text{m}$ and length $40\mu\text{m}$ (left) and its simulated scattering pattern (right).

However, this is not always the case. Sometimes, the speckle pattern eradicates other features. One such example is a rough sphere¹⁸. Usually, rings can be seen in the scattering pattern of a smooth sphere. However, these are lost in the scattering pattern as the surface of the sphere roughens. Fig. 5.29 demonstrates this phenomenon, comparing a slightly rough sphere with a smooth sphere. These models have a radius of $15\mu\text{m}$, and their simulated scattering patterns are shown in the bottom row.

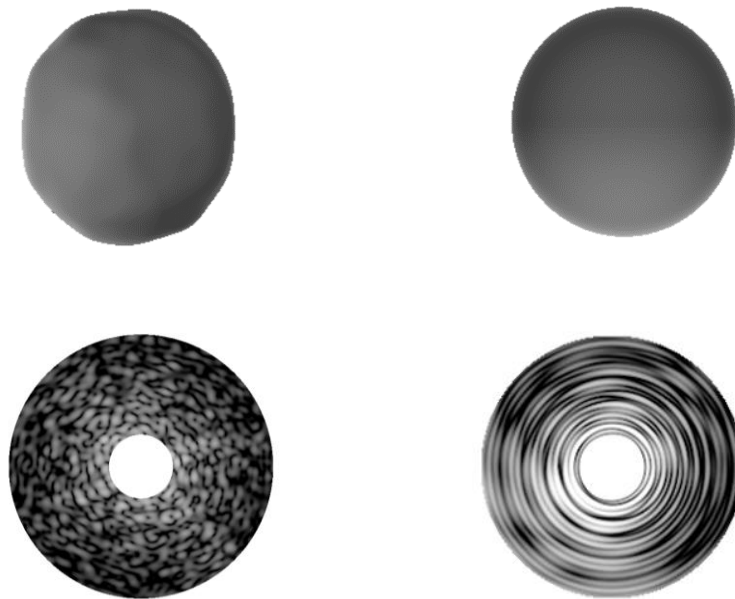
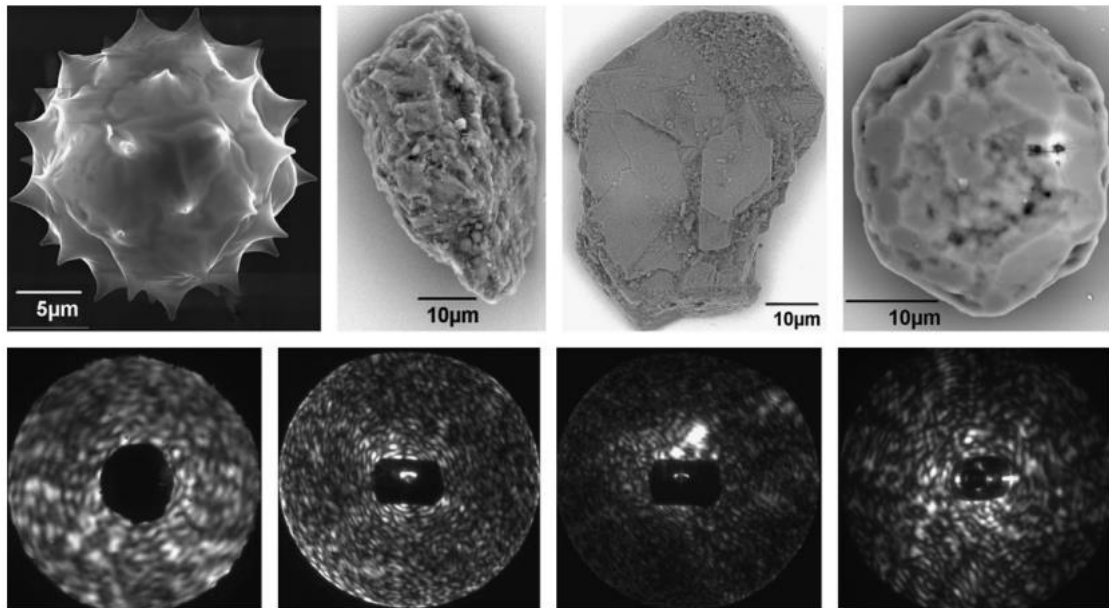


Fig. 5.29: Models of rough sphere with standard deviation 0.15 and correlation angle 30° (top left) and a smooth sphere (top right), both of radius $15\mu\text{m}$ along with their simulated scattering pattern (bottom row).

Thus, it is not always possible to retrieve shape information from a crystal with rough surfaces. Ulanowski *et al.* (2012) states, “The complexity of these particles and of the resulting patterns, which exhibit speckle-like appearance, makes characterization difficult and in extreme cases prevents particle shape retrieval by direct comparison with theory”. For example, in Fig. 5.30

¹⁸ Rough surfaced sphere crystals are modelled using a program for generating crystals with a Gaussian random surface (Muinonen *et al.* 1996).

taken from Ulanowski *et al.* (2012), the particle types and shapes are all different, yet their scattering patterns look similar and do not provide much information other than speckles.



*Fig. 5.30: (top) SEM images of a pollen, rough and slightly rough mineral dust grains, and a rough ice analogue respectively (from left to right), with their corresponding scattering patterns (bottom), taken from Ulanowski *et al.* (2012).*

In general, the roughness of all types of crystals can be assessed by exploiting the textural features in the images using Grey Level Co-occurrence Matrix (Ulanowski *et al.* 2014). Further details on the method can be found in Section 4.5.2. When speckles occur alongside distinct features indicative of the crystal shape, the patterns are classified in the specific crystal category such as ‘rough plates’, ‘rough columns’ etc. For rough plates and rough columns, the size estimation is done based on the width of the scattering arc as mentioned in Sections 5.1 and 5.2. In cases where only speckles (but no shape structure) are visible, patterns are grouped into the general ‘Rough crystal’ category. The size estimation of such crystals is based on the Speckle Analysis method presented in Section 4.5.1.

5.4.1 Testing the Speckle Analysis code using AIITS images

AIITS images require a different value for ‘z’ (Equation 4.1). This is because, the image dimensions differ from the simulated images used in Section 4.5.1. Native AIITS images have a dimension of 640x512 pixels. For easier manipulation, a cropped version of 458x458 pixels is used in which the outer ring (scattering angle 25°) just touches the border of the image. Therefore, z=491 pixels are obtained from the equation below:

$$z = \frac{458/2}{\tan 25^\circ} = 491 \text{ pixels}$$

On substituting $\lambda=532\text{nm}$ and $z=491\text{pixels}$, Equation 4.1 becomes:

$$D = \frac{332.7}{D_s} \mu\text{m} \quad (5.1)$$

D_s , which is the average speckle diameter (in pixels), is calculated from the image using the Speckle Analysis code.

The investigation of the Speckle Analysis algorithm in Section 4.5.1.1 with simulated scattering patterns demonstrated that the accuracy of the analysis was highly sensitive to the Marker value. The same investigation was repeated with real (AIITS) scattering patterns to determine the optimum Marker value.

There were 91 images in total and Marker values between 0.6 and 0.9 were used. Table 5.2 shows the result of how many crystal sizes were predicted correctly using different marker values. Out of the other Marker values, 0.75 is still the best with a prediction accuracy of around 55% within one standard deviation.

Marker values	No. of correct predictions	Percentage
0.6	35	38.46%
0.7	48	52.75%
0.75	50	54.95%
0.8	48	52.75%
0.9	4	4.40%

Table 5.2: The percentage of correct crystal sizes predicted by the Speckle Analysis code while using different Marker values.

These results clearly indicate that a Marker value between 0.7 and 0.8 is optimal. Though the authors of Ulanowski *et al.* (2012), recommend using 0.6 as the constant Marker value, based on testing both modelled crystals' simulated patterns and AIITS scattering pattern images, it was found that the Marker value should be 0.75 instead of 0.6 for this dataset. However, as mentioned in Section 4.5.1.1, rather than relying on a constant Marker value, it is recommended to find the optimum Marker value based on the dataset and image dimension.

The accuracy of the predicted rough crystal diameter obtained from the Speckle Analysis code is tested by visual inspection, comparing the simulated scattering pattern of rough spheres of different sizes of 5 μm radius apart. For example, the AIITS image is compared with the simulated scattering pattern of a rough sphere of radius 10 μm . If the AIITS image shows smaller speckle size, it will next be compared with the simulated scattering pattern of a rough sphere of radius 15 μm . Otherwise, it will be compared with the simulated scattering pattern of a rough sphere of radius 5 μm .

Fig. 5.31 shows the simulated pattern of rough spheres of radiuses 5, 10 and 15 μm respectively. The speckle size of AIITS no.166 in Fig 5.32 is smaller than the simulated pattern of rough spheres of radiuses 5 μm and larger than 10 μm and hence, radius 5-10 μm will be estimated. Similarly, for AIITS no.83 in Fig 5.32, the speckle size lies between the speckles in the simulated patterns of 10 and 15 μm radius ranges and thus, 10-15 μm will be estimated.

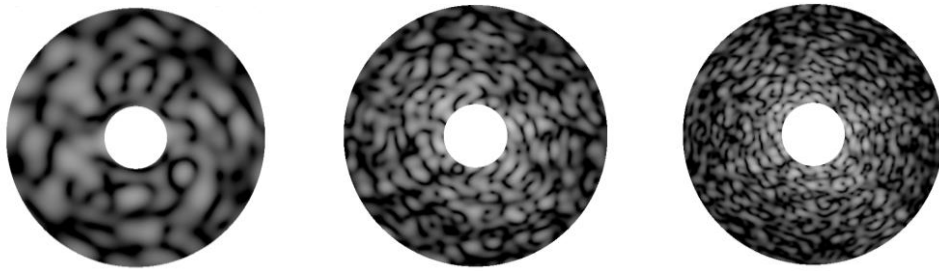


Fig. 5.31: Simulated scattering patterns of rough spheres of radiuses 5, 10 and 15 μ m (left to right).

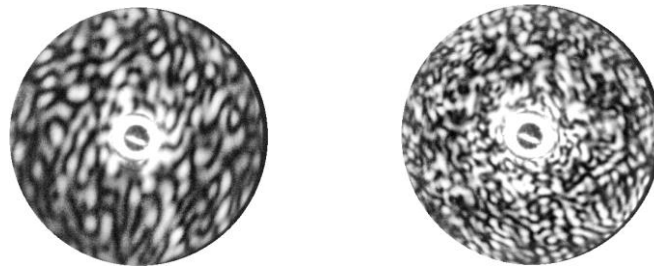


Fig. 5.32: AIITS no. 166 and no. 83 (left to right).

Until now, modelling and analysis of scattering patterns of different types of crystals as well as their comparison with the AIITS scattering pattern images were discussed in detail using several examples. The result of analysing the AIITS images taken on 5th March 2015 ATTREX are discussed in the next chapter with statistics.

6. RESULTS AND DISCUSSION

6.1 AIITS results from the 2015 ATTREX mission and their interpretation

In this research, the AIITS patterns were classified based on visual inspection depending on the overall size, shape, and surface texture of the crystals. Based on the analysis, out of 2426 patterns, only a subset of 876 images (36.10%) can be used; the others were either blank or only the artefacts between 0° and 8° were visible, and hence discarded. The resulting proportion of different crystal categories are given in Table 6.1, which is a summarized table. For a more detailed information see Table 6.4.

Crystal Categories	Number	Percentage
Very small crystals	409	46.69%
Columns	27	3.08%
Plates	43	4.91%
Rough crystals	106	12.10%
Quasi-spheroids	291	33.22%
Total	876	100%

Table 6.1: Classification of AIITS images into different crystal types and textures.

Each category from the table is explained in detail below.

6.1.1 Very small crystals

From Table 6.1, the most common crystal type is 'very small crystals' (46.69%) comprising crystals in the radius range 1-5 μ m. Most of the crystals (237) in this group showed features similar to the ones arising from quasi-spheroids, that is about 1-4 ring-like structure in their scattering pattern. Small droxtals and any small crystal with rounded edges and/or slightly rough surface texture are also likely to be in this group, as their scattering pattern show similar features and it is often difficult to distinguish them from the actual quasi-spheroidal crystals. For particles in this size range, the features in the scattering pattern will be quite spread out. As a result, it is impractical to accurately classify them into finer categories such as quasi-spheroids, droxtals, small crystals with rounded edges or rough surface texture. The rest of the crystals (172) out of 409, exhibited an arc-like feature or elongated oval shape with parallel lines in the scattering pattern which could indicate that they are columns. The former and latter type are shown in Fig. 6.1 and Fig. 6.2 respectively.

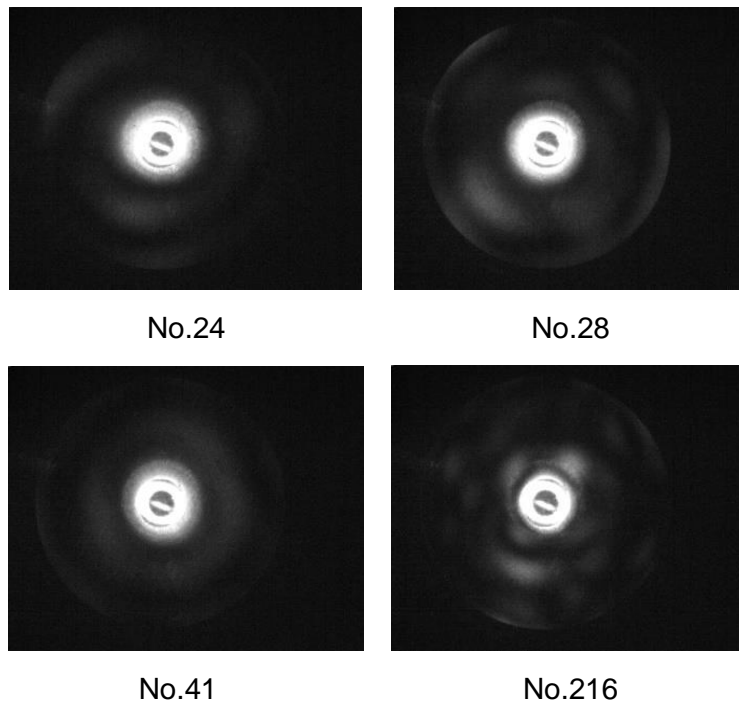


Fig. 6.1: Very small crystals displaying quasi-spheroidal features (above).

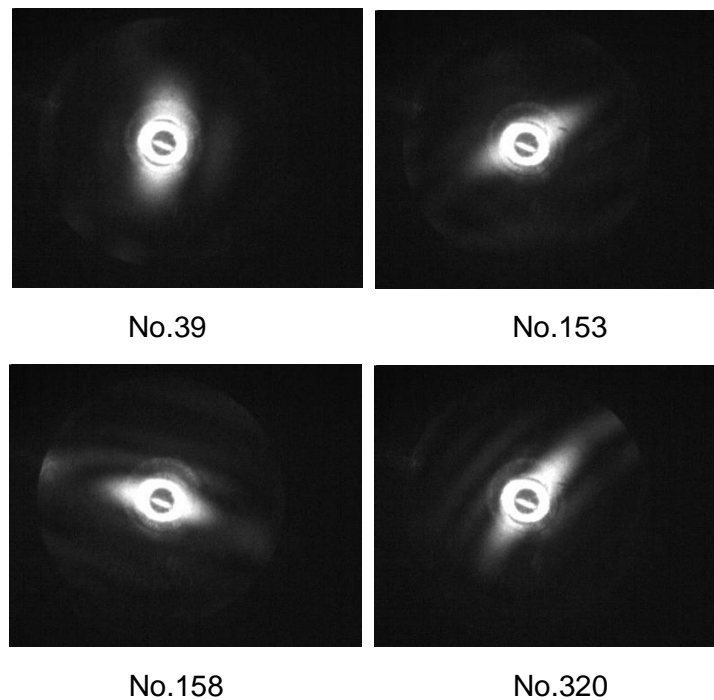


Fig. 6.2: Very small crystals displaying columnar features (above).

6.1.2 Columns

27 of the total data set (3.08%), were identified as 'Columns' and these were the least common type of crystal. The prism height ranged between 10-40 μ m. This category was further divided into needles, rough solid columns and smooth solid columns comprising 1, 9 and 17 crystals respectively in each group. While, the height of the rough solid columns spread across the 10-

40 range, most of the smooth solid columns were found to be in the 10-20 μ m range. Based on the analysis, the aspect ratios of the columns were <1 (basal radius $<$ half the prism length) indicating that they are thin columns. The only exception was for a rough column with an aspect ratio of 1, which implies a thick or equiaxed column. The details are given in Table 6.2.

Prism height (μ m)	Needle	Rough Column	Smooth Column	Total number of crystals in each size range
10-20	1	3	13	17
20-30		2	4	6
30-40		4		4
Grand Total	1	9	17	27

Table 6.2: Sub-categories of column crystals.

An example crystal from each sub-category is shown below (Fig. 6.3).

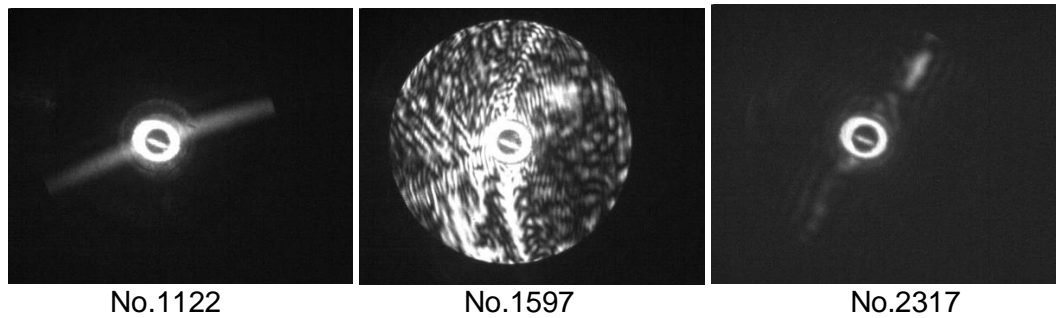


Fig. 6.3: Crystals representing the sub-categories of columns: Needles, rough solid columns, and smooth solid columns respectively (left to right).

Fig. 6.4 shows the height of the rough columns in different size ranges along with the combined roughness parameter using a box and whisker chart. (See Section 4.5.2 for combined roughness parameter). This chart is one of the best graphical methods to display the summary of variation in a dataset and it represents the following:

- The box represents the interquartile data range with lower and upper quartile values on the lower and upper end of the box. (Lower and upper quartile implies the median of the lower and upper half of the dataset respectively. The difference between these two is the interquartile range).
- Within the box, 'x' marks the mean of the dataset.
- The horizontal line inside the box is the median of the dataset.
- Lines extending from the either side of the box, called whiskers indicates the minimum and maximum values in the dataset.

The three rough columns in the 10-20 μ m size range have their combined roughness value roughly between 0.3 and 0.6. The two mid-sized (20-30 μ m) rough columns have roughness values of 0.37 and 0.48. For the rest of the four rough columns in the 30-40 μ m size range, the roughness value varied from 0.40 to 0.68.

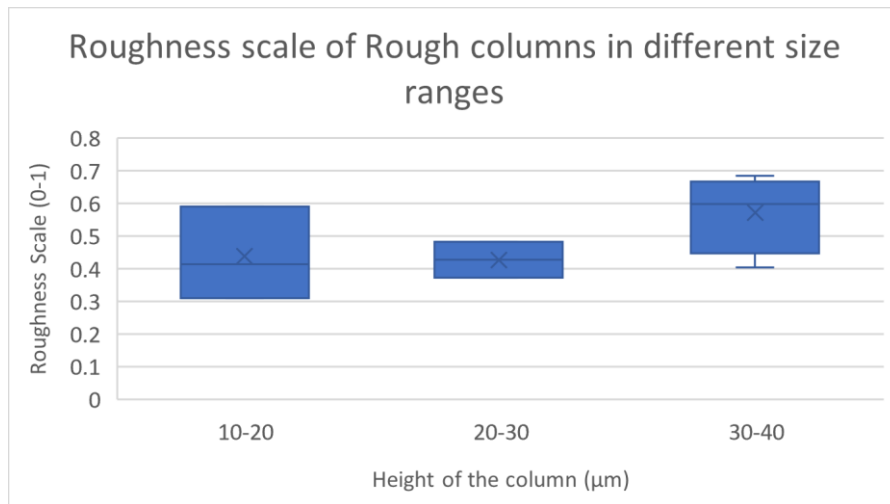


Fig. 6.4: The roughness parameter and size ranges of rough columns.

6.1.3 Plates

The third category in Table 6.1, 'Plates', are comprised of 43 crystals contributing 4.91% of the overall crystal population. It is the second least common type of crystal. The sub-categories of plates are given in Table 6.3, along with their frequency of occurrence and size estimation (the total number of crystals found in a particular size range is given in brackets in the 3rd column). As plates orientate on their basal facet, it is difficult to estimate how thick they are, since this dimension is out of view. However, based on the analysis of tilted plates, they were thin, with their prism length less than or equal to basal radius. In terms of aspect ratio, this will be ≤ 1 (thickness/diameter). The droxtals were usually equiaxed, with an aspect ratio close to 1.

Types of Plate	Occurrence	Size estimation in μm
Pristine, smooth regular hexagonal plate	5	(2) rad:15-20 (1) rad:35-40 (1) rad:40-45 (1) rad:45-50
Regular hexagonal plate with rounded edges	7	(4) rad:25-30 (1) rad:45-50 (1) rad:20-25 (1) rad:30-35
Rough (regular hexagonal) plate	1	(1) rad:25-30; combined roughness:0.39
Pristine Scalene plate	2	(1) rad:20-25, ef<0.4. (1) rad:40-45, ef:0.7
Scalene plate with rounded edges	10	(4) rad:20-25; ef:0.4-0.7 (2) rad:15-20; ef:0.4-0.5 (1) rad:10-15; ef:0.2 (3) rad:5-10; ef:0.7
Rough scalene plate	4	(1) rad:10-15; ef0.7, combined roughness:0.6499 (1) rad:20-25; ef0.7, combined roughness:0.6933 (1) rad:20-25; ef:0.7, combined roughness:0.689

		(1) rad:5-10; ef:0.7, combined roughness:0.5423
Droxtals	14	(8) rad:15-20 (5) rad:20-25 (1) rad:25-30

Table 6.3: The sub-categories of plates, and their size estimation (rad: radius estimated in microns; ef: Edge Factor, a dimensionless value (between 0 and 1) used to change the regular hexagonal crystal to a rhomboid crystal, see Section:5.1.3; for combined roughness, see Section 4.5.2).

Examples of sub-categories of plates are shown in Fig. 6.5. Based on the features in the scattering pattern, these are regular hexagonal plates, scalene plates and droxtals in the top, middle and bottom panels respectively.

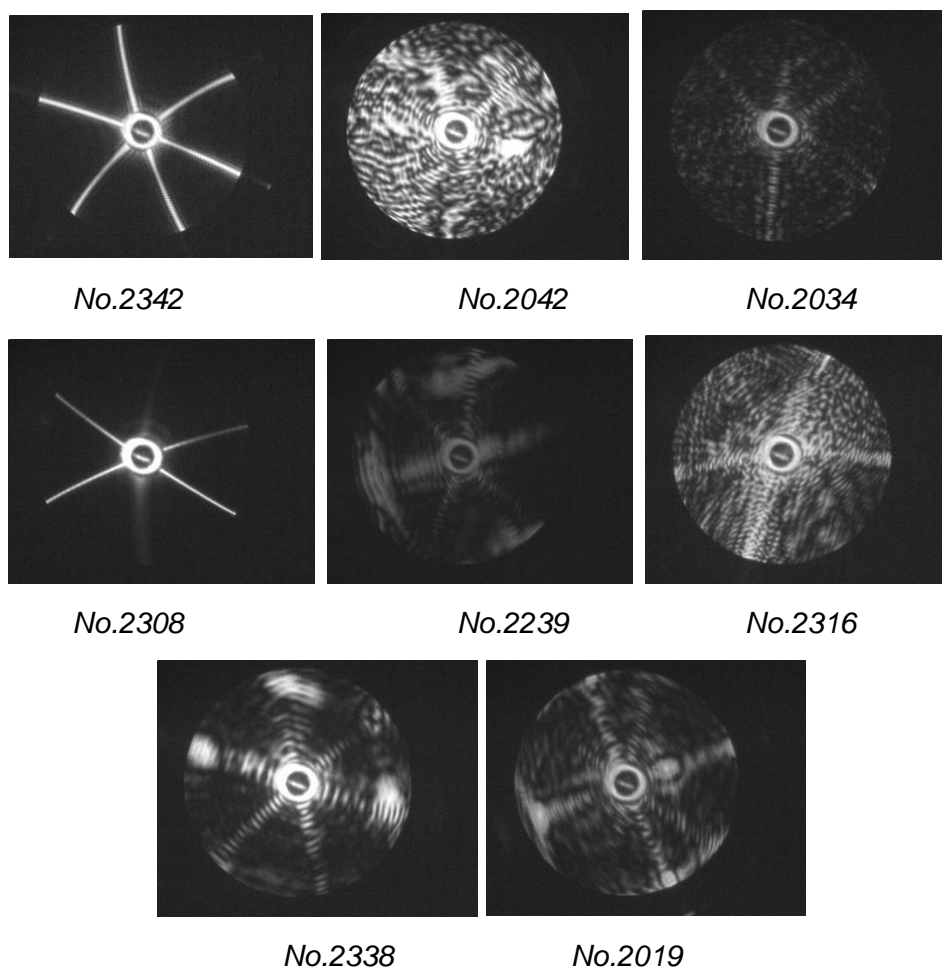


Fig. 6.5: Different types of plates. **Top panel:** regular hexagonal plate, regular hexagonal plate with rounded edges, regular hexagonal plate with rough surface (left to right). **Middle panel:** Pristine smooth scalene plate, smooth scalene plate with rounded edges, scalene plate with rough surface (left to right). **Bottom panel:** Regular droxtal (left), Scalene droxtal (right).

The Fig. 6.6 shows a doughnut chart representing the percentage contribution of different types of plates. Over half of the 'Plates' (56%) were droxtals and scalene plates with rounded edges, followed by smooth regular hexagonal plates without (12%) and with (16%) rounded edges. The scalene plates and regular hexagonal plates with rough texture were the least common types among the 'Plates', contributing 5% and 2% respectively.

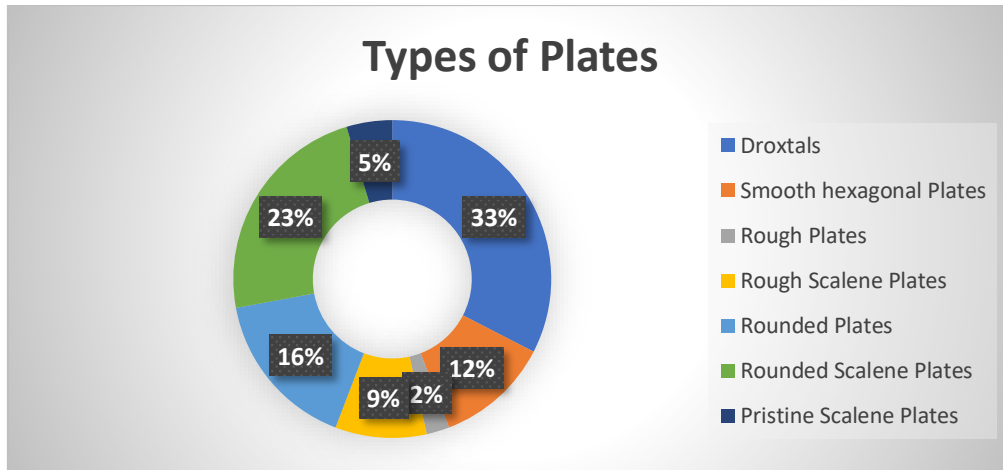


Fig. 6.6: The different types of plates based on their percentage contribution.

Using the stacked column chart, the subcategories of plates in various size ranges along with the frequency in which they appeared are shown in Fig. 6.7. Most of the plates, in general, were sized in 15-30 μm radius range. The pristine, smooth hexagonal plates have larger size ranges of 35-50 μm . On the other hand, both scalene plates with rounded edges as well as rough texture have smaller radius range of 5-25 μm . Interestingly, apart from a scalene plate in the 40-45 μm range, there are no scalene plates beyond 25 μm radius. Nearly all varieties of plates were found to be around the mid-range of 20-25 μm .

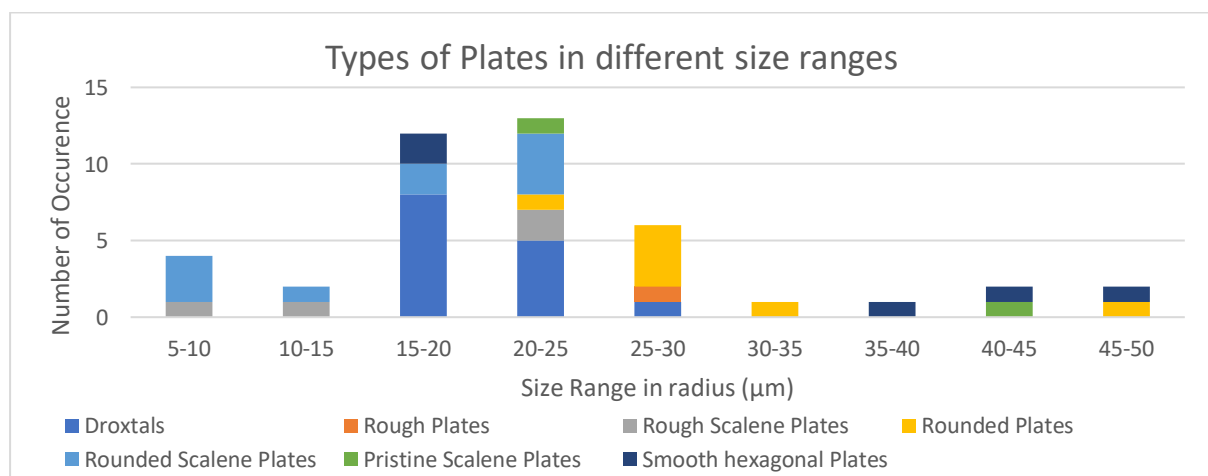


Fig. 6.7: The subcategories of plates in different size ranges.

6.1.4 Rough crystals

The 'Rough crystal' category, consisting of 106 crystals representing 12.10%, are crystals with unknown shape, but with rough surface texture. The size of the crystals as well as their

roughness are obtained using Speckle Analysis (Section 4.5.1) and Combined Roughness (Section 4.5.2) code respectively.

Overall, the combined roughness parameter ranges between 0.2-0.9 and hence the category is split into three groups based on roughness, namely, slightly rough, medium rough and very rough crystals ranging from 0.2-0.4, 0.4-0.6 to 0.6-0.9 respectively. An example from each category is shown in Fig. 6.8. They have a combined roughness of 0.63, 0.45 and 0.36 corresponding to very rough, moderate rough and slightly rough crystals respectively.

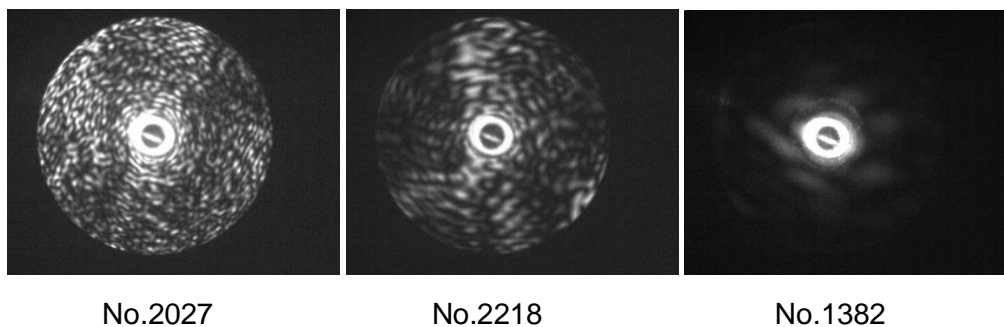


Fig. 6.8: Examples of very rough, moderate rough and slightly rough crystals.

The three groups are shown in Fig. 6.9 using the 'box and whisker' chart. The description on chart is mentioned under the 'rough column' in Section 6.1.2 with Fig. 6.4. The dots are outliers or significantly different values in the dataset. The size of the slightly rough crystals was found to be between 5-20 μm radius. However, for the very rough crystals it extended from 10 to 30 μm radius. The medium rough crystals covered both size ranges, that is, 5-30 μm radius.

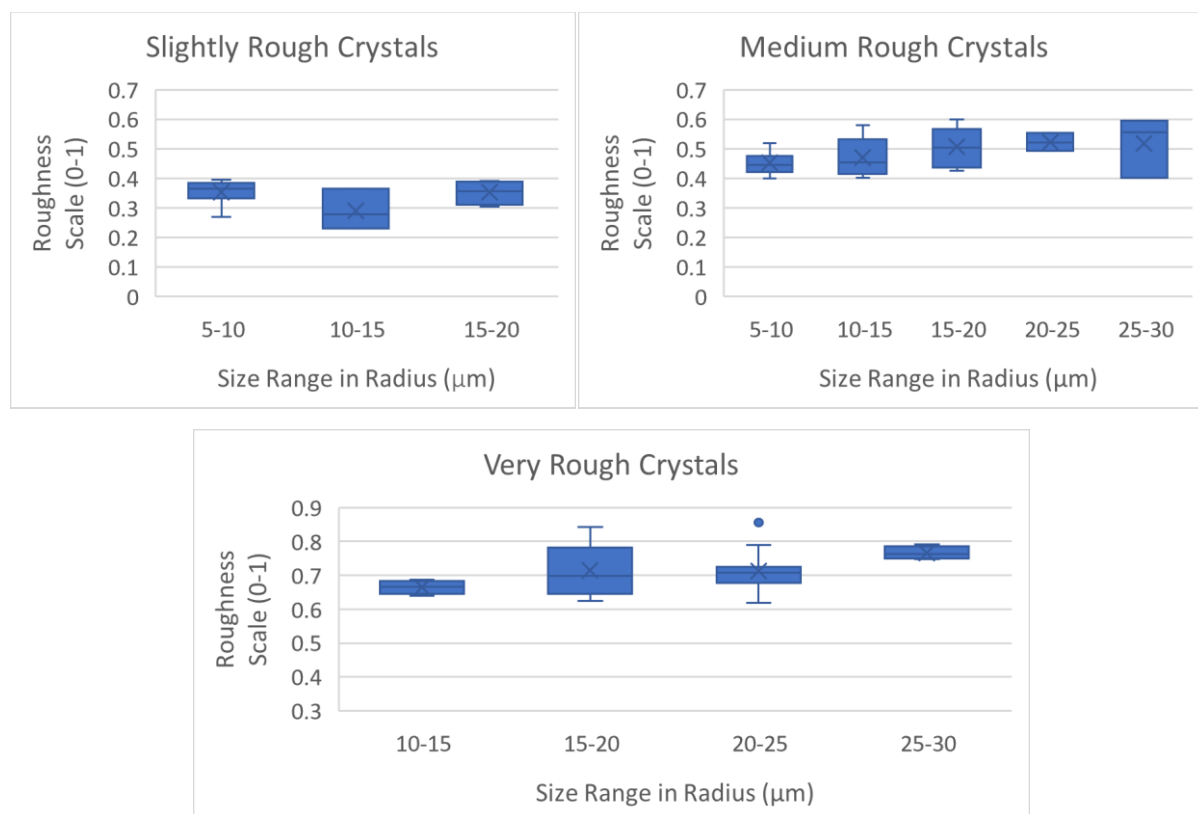


Fig. 6.9: The three varieties of rough crystals with varied sizes and roughness parameters.

The Fig. 6.10 shows all the crystals in the rough category with different roughness parameter and sizes. Apparently, the surface roughness increases with crystal sizes. Note that it has not been investigated whether the increasing roughness with crystal sizes is an artefact or not. This goes beyond the scope of the present study and hence further studies would be beneficial.

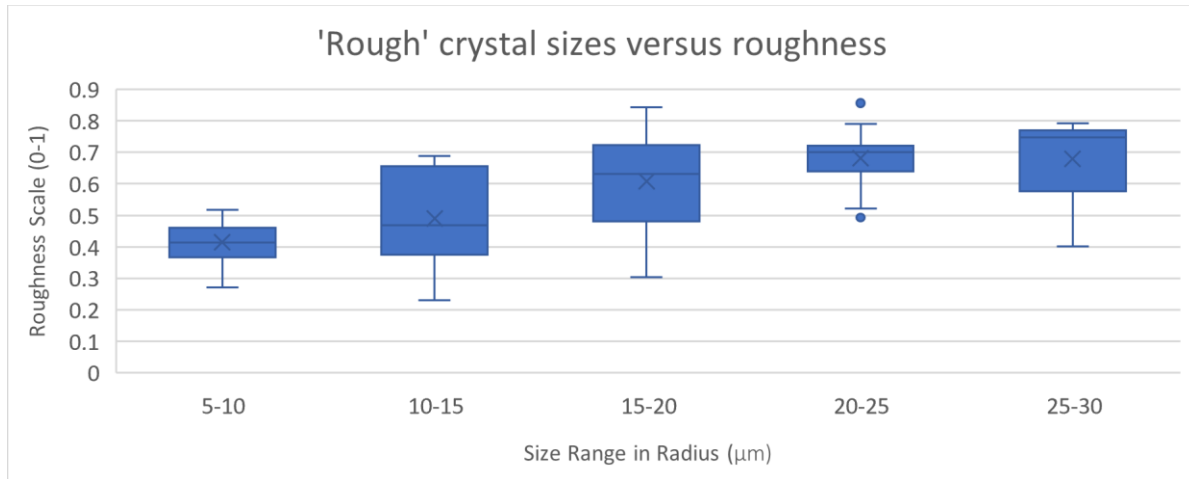


Fig. 6.10: The roughness parameter of different sized rough crystals.

There were 22 slightly rough crystals, 42 medium rough and 42 very rough crystals, making a total of 106. In Fig. 6.11, it is clear that very rough crystals are indeed larger in terms of size which implies that larger crystals have overall rougher surface texture. None of the slightly rough crystals were found above 20µm radius. The majority of the crystals were found to be in 5-10µm radius range with slight or medium roughness.

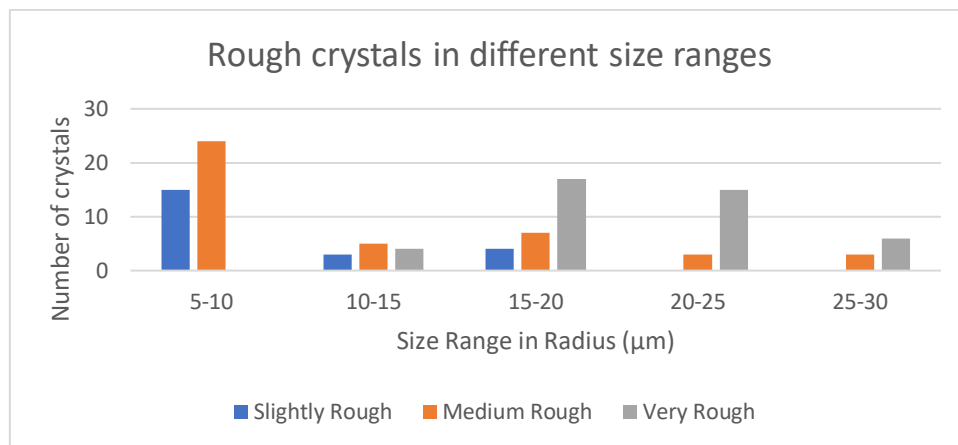


Fig. 6.11: The frequency of rough crystals in different size ranges.

6.1.5 Quasi-spheroids

The 'Quasi-spheroid' category is the second common type of crystal with 291 crystals representing 33.22% of the overall crystal population. These crystals are further divided into two groups, smooth and rough quasi-spheroids, based on their surface texture. The smooth quasi-spheroids are crystals with smooth surface as well as significantly rounded edges, and they feature ring-like structure in the scattering patterns. The rough quasi-spheroids are rough surfaced crystals with significantly rounded edges. Therefore, a combination of both ring-like and speckle-like structures are noticeable in their scattering patterns.

(a) Smooth quasi-spheroids:

Overall, 178 smooth quasi-spheroid crystals were found in the radius range 5-25 μm . Among them, over half of the crystals, that is 55% (98 crystals), were in the small radius range of 5-10 μm . 42%, represented by 74 crystals, were found to be in the 10-15 μm bin. The smaller portion of 3%, correspond to 5 crystals in 15-20 μm and just 1 crystal in 20-25 μm bin. The distribution of different sized quasi-spheroid crystals represented using a bar chart is illustrated in Fig. 6.12.

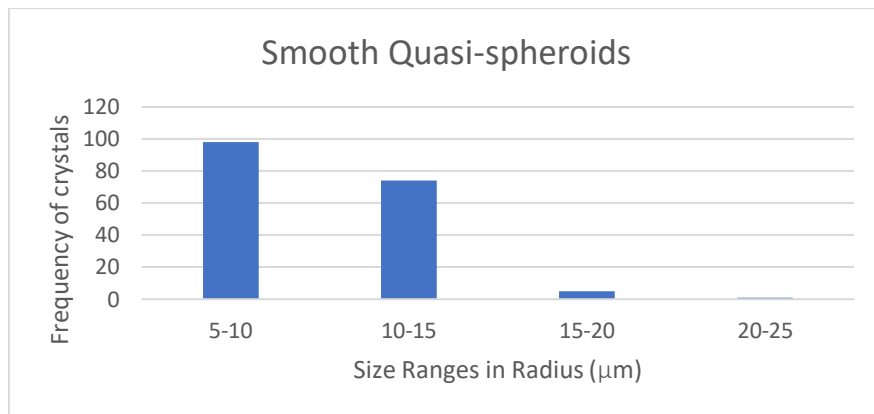


Fig. 6.12: The frequency of 'smooth quasi-spheroid' crystals in different size ranges.

The size of these crystals was estimated by manually counting the rings in the scattering pattern as well as using the speckle Analysis code. Fig. 6.13 shows some examples of Smooth Quasi-spheroids of various sizes. The No.1981 and No.2024 has 5-6 and 9-12 rings and they fall into the 5-10 μm and 10-15 μm sizes respectively. In the bottom panel of Fig. 6.13, there are 14-18 rings in No.2324 and 18-24 rings in No.2410. The former and latter belongs to size ranges of 15-20 μm and 20-25 μm radius ranges respectively.

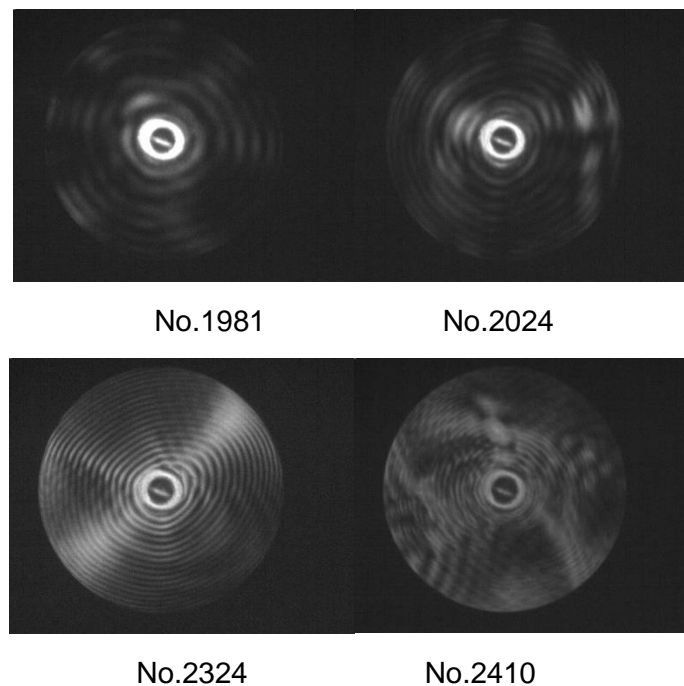


Fig. 6.13: Examples of quasi-spheroid crystals in different radius ranges.

(b) Rough Quasi-spheroids:

There were 113 crystals which showed both features like rounded edges as well as rough surface texture based on the image analysis. These are included in the 'rough quasi-spheroids' category which contributes 12.9% to the total crystal population. Examples are shown in Fig. 6.14. While No.2072 has 16-18 rings implying a crystal radius of 15-20 μm , the No.2357 has 10-14 rings inferring a crystal radius of 10-15 μm . The former and the latter have a roughness of 0.69 and 0.38 respectively.

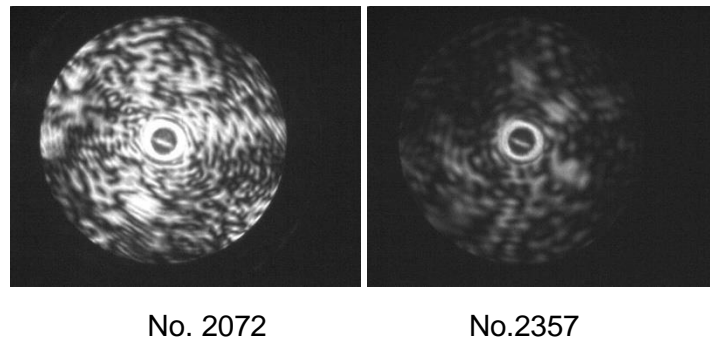


Fig. 6.14: Examples of rough quasi-spheroid crystals.

The bar chart in Fig. 6.15 shows the number of 'rough quasi-spheroid' crystals in different size ranges. There are 49 crystals (43%) in the 10-15 μm radius range making it the most populated size range. On its either side, 5-10 μm and 15-20 μm represented 19% with 21 crystals and 22% with 25 crystals respectively. The lowest number, with 18 crystals (16%) were found in the 20-25 μm size range.

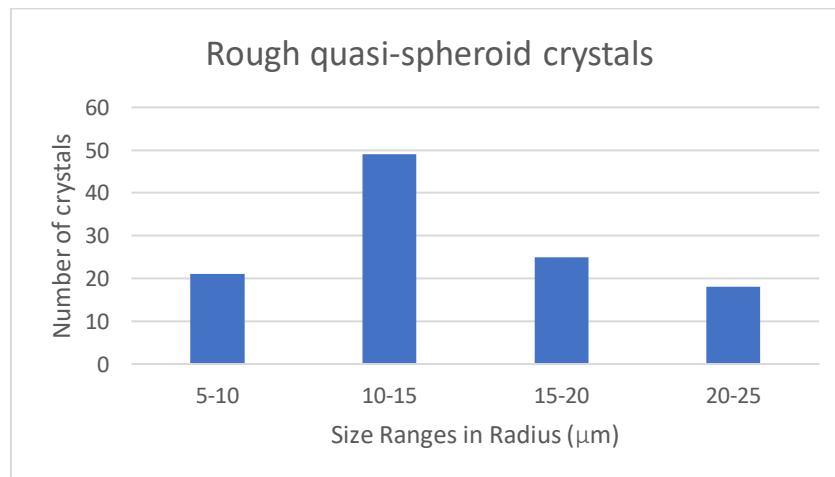


Fig. 6.15: The frequency of 'rough quasi-spheroids' crystals in different size ranges.

Just like smooth quasi-spheroids, the size estimation of this type of crystals were also done by counting the number of rings as it is more robust and easier compared to Speckle Analysis. The Speckle Analysis code was also applied on unsaturated images (93 out of 113 images of rough quasi-spheroids). The 10 saturated images are excluded from the comparison of these two methods.

The Fig. 6.16 shows the comparison of crystal size estimation by testing 93 rough quasi-spheroidal crystals based on manual ring counting and automated speckle analysis (using marker value 0.75). The two methods agree reasonably well for small crystal sizes. As crystal size increases (diameter > 40 μm), speckles merge to form larger speckles and hence the sizes were underpredicted by the Speckle Analysis code. For instance, in Fig. 6.16, the Speckle Analysis code predicted between 18 and 37 μm for crystal sizes between 40 and 50 μm. As an example, a cropped version of original image of AIIITS No.2048 is shown in Fig. 6.17 (left), along with reconstructed image used in Speckle Analysis code, Fig. 6.17 (right). It can be seen that some of the highlighted speckles (or rings) are merged and while predicting the crystal diameter from the median of these speckles, there will be inaccuracies. A particle size of 33.17 μm was predicted by the Speckle Analysis code. However, based on manual ring counting, 18-22 rings can be seen and has an estimated diameter of 40-50 μm (see Table 5.1).

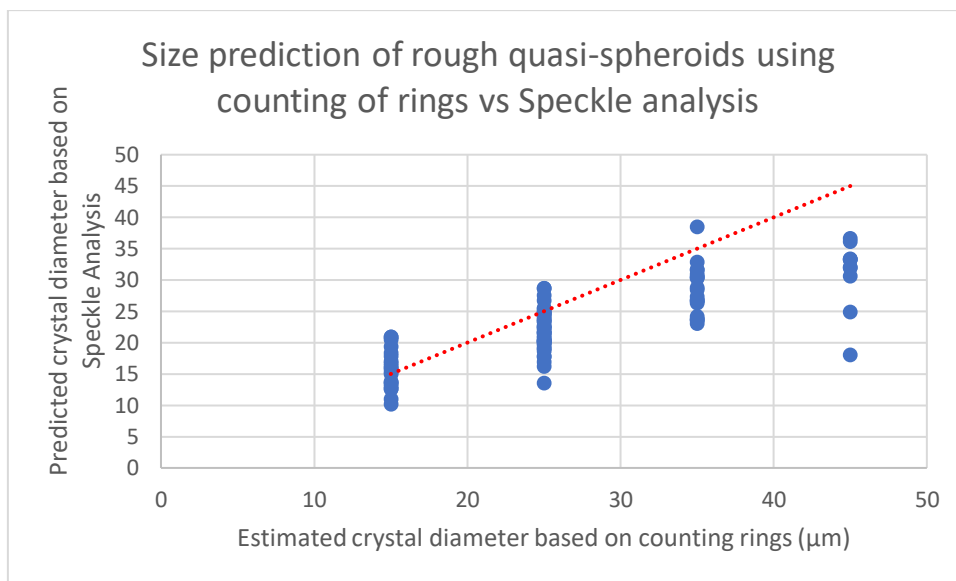


Fig. 6.16: Comparison of crystal size (diameter) prediction based on manual ring counting and automated speckle analysis code (using 0.75 marker value). The trendline is shown in red dotted line.

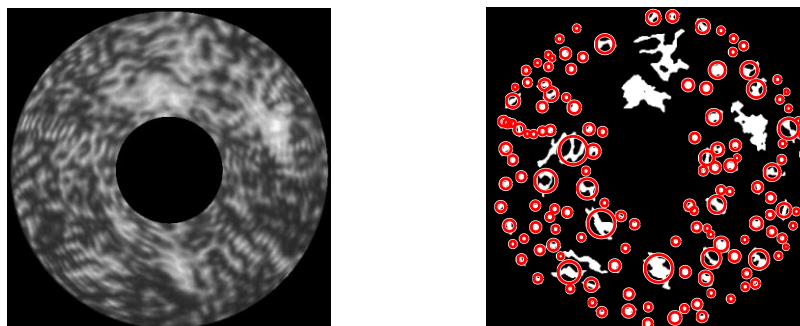


Fig. 6.17: (left) cropped and masked image of AIIITS number 2048; (right) highlighted speckles in reconstructed image used in Speckle Analysis code.

The combined roughness values of these crystals were also determined to find out how rough these crystals were. This is given in Fig. 6.18. Even though there are a few outliers represented by the dots, overall, the data shows an increasing trend of roughness with crystal size as expected. The mean roughness rises from 0.4 to 0.7 as the size ranges between 5-25 μm .

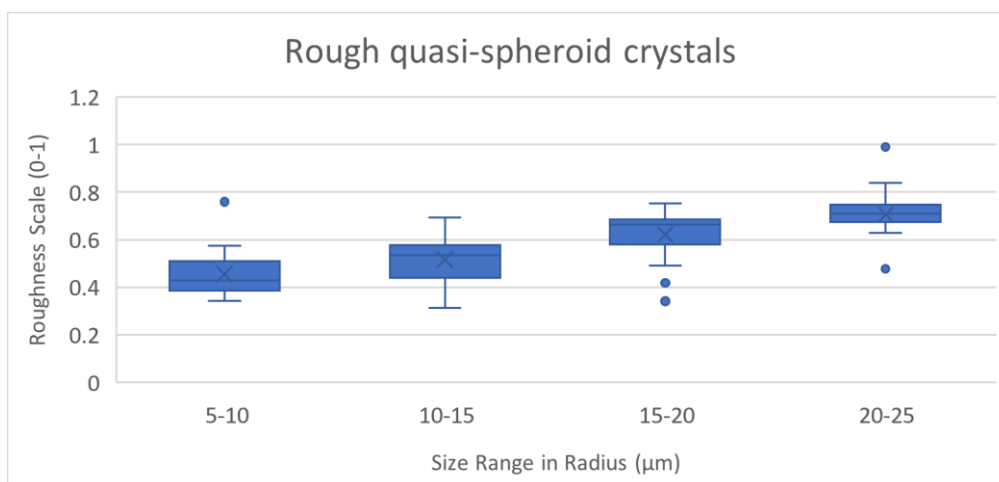


Fig. 6.18: The combined roughness value of 'rough quasi-spheroid' crystals.

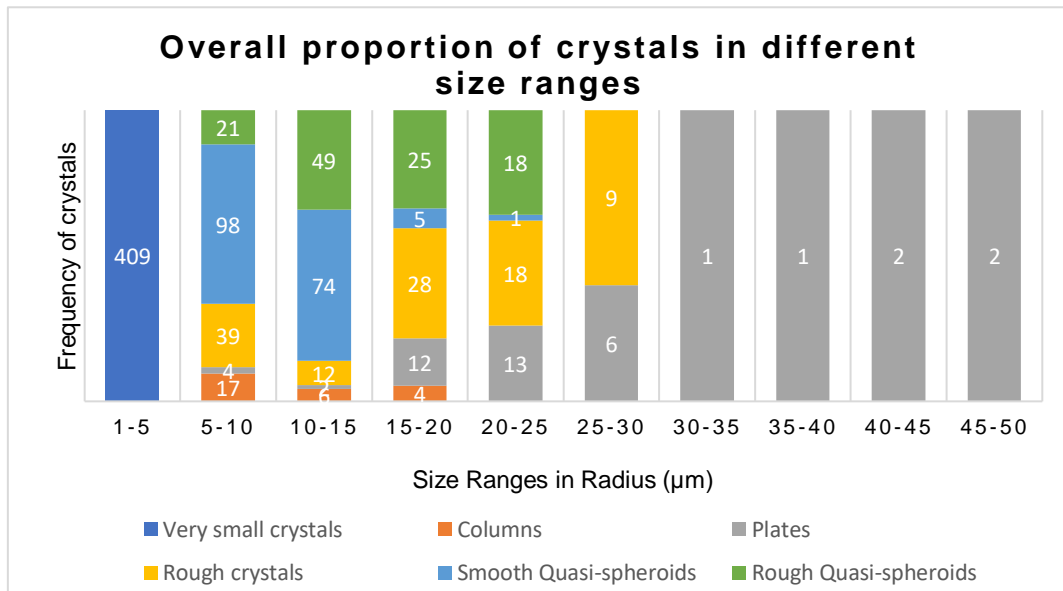
A more detailed table (compared to Table 6.1) with sub-categories of crystals is given below (Table 6.4). The same-coloured rows belong to the same crystal type.

Crystal Types	Sub-categories of Crystals	Number of crystals
Very small crystals	Very small crystals (rounded) (Rad:1-5 μm)	237
	Very small crystals (column-like) (Rad:1-5 μm)	172
Columns	Smooth columns (length:10-30 μm)	17
	Rough columns (length:10-40 μm)	9
	Needles (length 10-15 μm)	1
Plates	Pristine, smooth plates (Rad:15-50 μm)	5
	Plate with rounded edges (Rad:20-50 μm)	7
	Scalene plates (Rad:20-45 μm)	2
	Scalene plates with rounded edges (Rad:5-25 μm)	10
	Rough plates (Rad:25-30 μm)	1
	Rough scalene plates (Rad:5-25 μm)	4
	Droxtals (Rad:15-30 μm)	14
Rough crystals (unknown crystal shape)	Slightly rough (Rad:5-20 μm)	22
	Medium rough (Rad:5-30 μm)	42
	Very rough (Rad:10-30 μm)	42
Quasi-spheroids	Smooth quasi-spheroids (Rad:5-25 μm)	178
	Rough quasi-spheroids (Rad:5-25 μm)	113
	Total	876

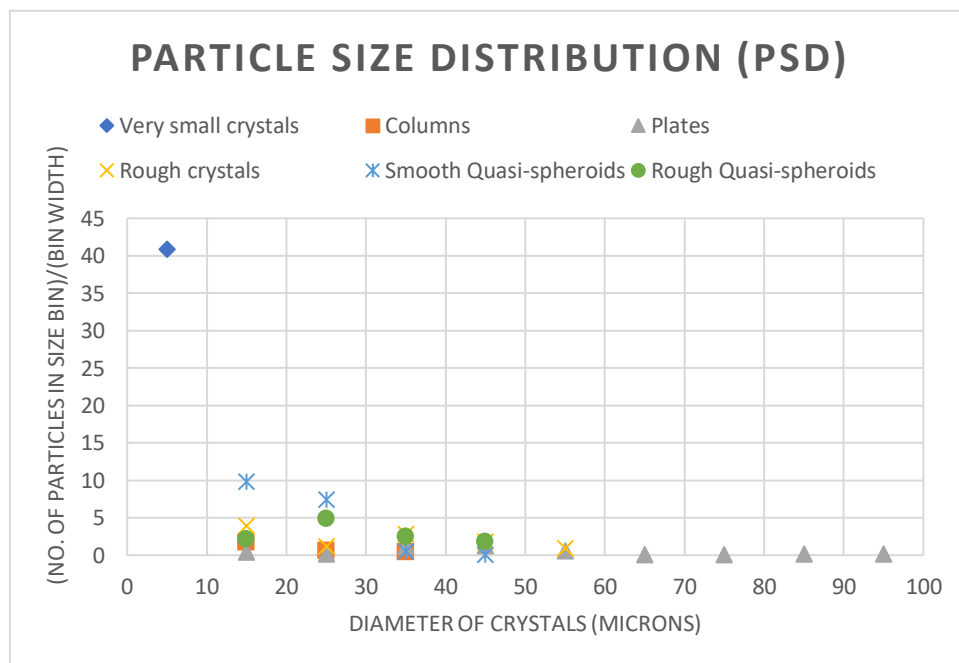
Table 6.4: A detailed table with the size and number of sub-categories of ice crystals.

In Fig. 6.19 (a), the proportions of different types of crystals in different size ranges are shown. The radius range 1-5 μm are classified as very small crystals. The four radius ranges between 30-50 μm on the extreme right are solely contributed by plates; even though there are only 6 plates in the specified size ranges. A wide variety of crystal types; including plates, columns,

rough crystals, smooth as well as rough quasi-spheroids, can be seen in the lower to mid radius ranges (5-30 μm). All the crystals are shown in terms of radius; for columns, half the prism length is used as 'radius' to incorporate it into the Fig. 6.19 (a). No aggregates were found in this scattering dataset. (The scattering patterns of aggregates are similar to columns, but additionally contain multiple scattering arcs running through the centre.) The Particle Size Distribution (PSD) is given in Fig. 6.19 (b). Note that the crystal diameter in microns is shown in the horizontal axis.



(a)



(b)

Fig. 6.19: (a) The overall proportion of various crystal types in different sizes. (b) Also plotted as a Particle Size Distribution (PSD).

Out of the 409 very small crystals, 237 are rounded crystals. Along with 291 (smooth and rough) quasi-spheroids, altogether there are 528 crystals with rounded edges, the most common crystal type (60%). They appear to be in the 1-25 radius range. This excludes plates with rounded edges and rough crystals which are of unknown type. The percentage further increases if these are counted in the rounded or quasi-spheroid group. In general, smaller crystals are predominantly quasi-spheroidal and as the size of the crystal increases, they become more and more complex.

A simplified representation of proportions of crystals in different size ranges is depicted in Fig. 6.20 using a 3D pie chart. The crystal sizes, indicated by different colours, are presented in percentages.

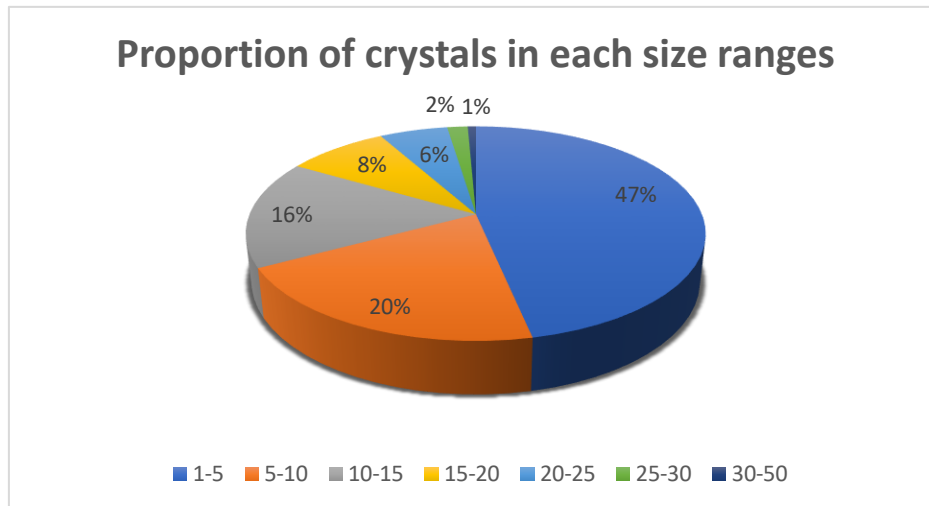


Fig. 6.20: The proportion of crystals in different size ranges. The sizes are in μm radius.

The most populous radius range is 1-5 μm with 409 crystals (47%). The numbers decrease with increasing size range. The second most populated radius range is 5-10 μm with 179 crystals (20%). The number of crystals decreases further to 143, 74, 50 and 15 in the radius ranges 10-15, 15-20, 20-25 and 25-30 μm respectively. The least populated bins extend from 30-50 μm . Two plates, one smooth with rounded edges and the other, regular smooth, pristine, were found in the 30-35 and 35-40 μm bins respectively. The same two crystal types were found again in the 45-50 μm range. A smooth, pristine and a scalene plate were found in the 40-45 μm range.

6.2 Imaging parameters which might have affected the particle classification results

This section includes some of the parameters which were noted during the image analysis procedure. The parameters like camera settings and combined intensity of the image are discussed below.

The camera parameters 'exposure time' and 'gain value' were set to 2 μs and 275 respectively and were not changed during the flight. However, some of the scattering patterns were weak (dim) and others were bright. One of the reasons for this difference in brightness level for images could be the following: Since the small crystals have small surface area there will be less scattering, and therefore, result in a weaker scattering pattern image; while the large crystals scatter strongly, and as a result, their scattering pattern image will be brighter. Even though this is not always the case, the general trend is that larger crystals have bright

scattering patterns compared to the smaller crystals. One of the disadvantages of the dim image is that the features, which helps to identify the crystal type, may be vague and hence less information can be processed. However, there are various functions that can be used in MATLAB to improve the image sharpness or brightness, and these are applied on weak images to get as much information as possible. One such method is described in Section 4.6.

In terms of size estimation of crystals, it is a common practice to find the combined intensity of a scattering image. The combined intensity is the total intensity or brightness in an image and is used as the usual sizing method for scattering probes that do not record scattering patterns. In general, the larger the crystal, the brighter the image will be and hence, greater the combined intensity value. For a dim image, the combined intensity value will be small corresponding to a smaller crystal. Therefore, by just sorting the combined intensity values, presumably the crystal sizes can be sorted. However, this is not a completely reliable method, and the reason is illustrated using examples. Two plots of combined intensity versus illuminated area are shown in Fig. 6.21 and Fig. 6.22 corresponding to regular hexagonal plates and smooth rounded crystals respectively.

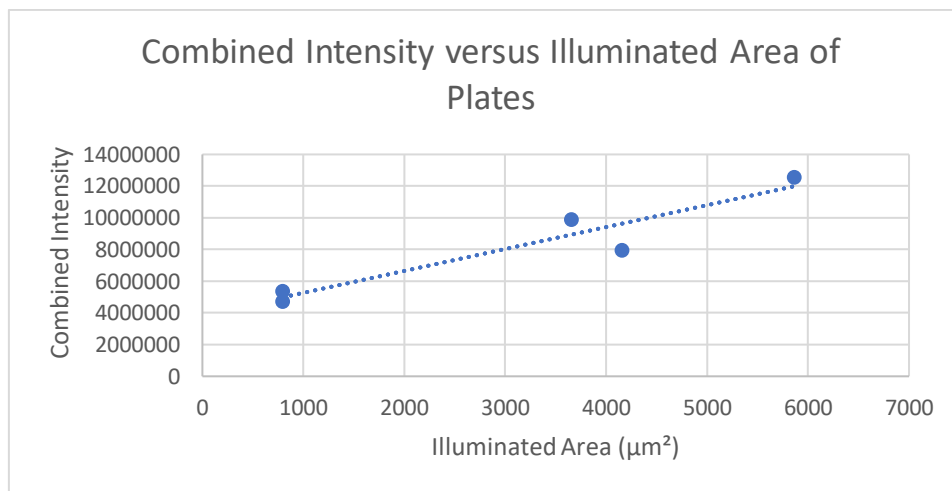


Fig. 6.21: Combined Intensity plotted against illuminated area of plates.

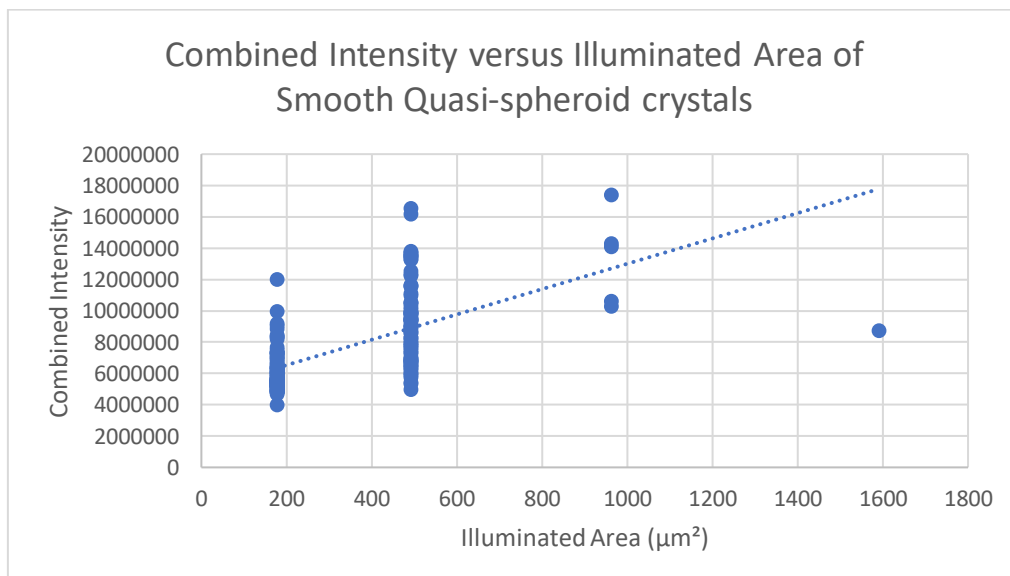


Fig. 6.22: Combined Intensity plotted against illuminated area of smooth quasi-spheroids.

The illuminated area refers to the area of the crystal that is illuminated by the beam. Hence, the illuminated area of plates implies the hexagonal area, which is $\frac{3\sqrt{3}}{2} r^2$, where r is the radius of the hexagonal plate, and the illuminated area of rounded crystals are approximated to the area of a circle, πr^2 , where r is the radius of the rounded crystals (circle).

In Fig. 6.21, five plates with radiuses between 15 and 50 μm were analysed. Based on the figure, the combined intensity increases with the illuminated area implying that the larger crystal scatter light more. The Fig. 6.22 is plotted using 178 smooth Quasi-spheroid crystals with four radius ranges of 5-10, 10-15, 15-20 and 20-25 μm . In this case as well, there is a general trend of combined intensity being proportional to the surface area of the crystal. Nevertheless, there are exceptions like the largest crystal with 22.5 μm (taken as the average of 20-25 μm) seems to have a lower combined intensity value despite of its size (illuminated area around 1600 μm^2). This is due to the lower overall brightness value of the image.

Any change in the overall brightness will affect the crystal size prediction. As an example, two images representing crystals with similar size and/or roughness but with different brightness values are shown in Fig. 6.23.

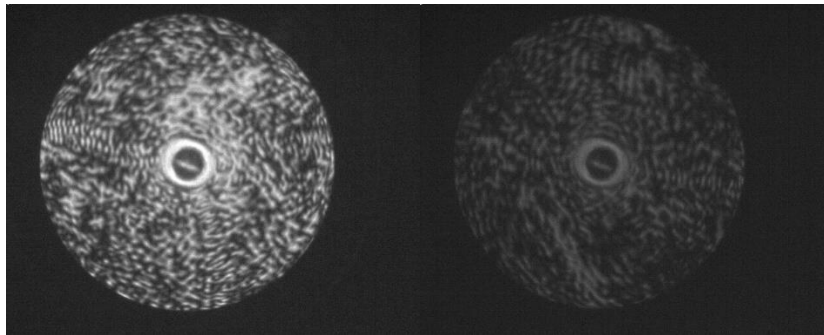


Fig. 6.23: (left) AITS image no. 2399 and (right) 2391.

Both the scattering pattern image no.2399 and 2391 are classified as rough crystals in the size range of radius 20-25 μm . The speckles in the image look similar in size indicating that they have similar size. The right image in Fig. 6.23 has a combined intensity of only 6,850,645 while the left one has over twice the amount of brightness (14,892,656). Determining the crystal sizes by sorting the combined intensity alone might lead to an inaccurate result of crystal size.

Therefore, as mentioned earlier, there were inconsistencies in terms of brightness and size of the crystals and cannot be relied on this process alone. Hence, individual visual inspection of scattering pattern images (by eye) is advisable.

6.3 Results from NASA probes

This section describes the results obtained from the NASA probes, taken during the CAST-ATTREX Global Hawk flight on 5th March 2015.

There were 3 data files in total with similar information format: the PSD (particle size distribution) number, Time stamp (in seconds), Latitude ($^{\circ}$ North), Longitude ($^{\circ}$ East), Altitude (m), Temperature (K), Mean maximum dimension of bin (μm), Number concentration ($\text{m}^{-3}/\mu\text{m}$) and Bin width (μm). The *first set* was solely from the 2D-S probe consisting of 282 PSDs, the *second set* contains the recordings from both FCDP and 2D-S consisting of 382 PSDs and

the *third set*, with 344 PSDs, was similar to the second set except that the first 2 bin sizes (10 and 20) of the 2D-S data were replaced by the FCDP data (as FCDP provides a more accurate measurement for smaller crystals).

PSDs represent the distribution of sizes of different particles. The timestamps recorded by the NASA instruments are in seconds (more specifically, Coordinated Universal Time (UTC) since 1st Jan 1970 00:00:00). (For example: A time stamp of ‘1425528704’ stands for ‘16499 days 04:11:44’). However, the AIITS records real time for its the scattering pattern images. Therefore, AIITS times were converted to these time stamps first. An algorithm, which automates the process of extracting the date and time from images (individual images or a folder of images) and converts them to UTC is given in Appendix 11.3. These UTC times are then directly searched in any of the above 3 datasets to check whether the ice crystals of similar size have been recorded by other probes at the same time. However, only few crystals were found at the exact same timestamp recorded by AIITS and NASA probes. Hence their average PSDs over the entire flight were investigated which is described below.

6.3.1 Particle size comparison between AIITS and NASA probes’ measurements

The analysis is limited to the UTC time between 04:07 and 15:55 on 5th March 2015. During this time range, both the AIITS and the NASA probes recorded the presence of some particles. Also, this study is limited to crystals with a mean maximum dimension of 100µm as that is the AIITS’ maximum measurement range. Therefore, the recordings with mean maximum dimensions above 100µm are excluded from the analysis. The particles are binned according to their size and the bin sizes are different for different NASA probes: for the *third dataset*, they range from 10 to 3105µm and have a bin width of 10µm for a mean maximum dimension up to 200µm. The mean maximum dimension of the bin refers to the maximum dimension (length or diameter) of the particle across its projected area. The number concentration specifies the count frequency of a specific bin size for each second. More specifically, the (particle) number concentration, given in Equation 6.1, depends on the count frequency or number of counts (f), the air speed (v), the sampling area of the triggering zone (A) and the time interval (t) (Thornton 2016).

$$N = \frac{f}{Avt} \quad (6.1)$$

Fig. 6.24 shows the PSDs (in logarithmic scale) measured by the NASA probes in comparison to the AIITS instrument. The size distribution of different types of crystals are shown in different colours for the AIITS and the primary y-axis is given in number of particles in size bin/width of the bin. The PSD measured by the NASA probes are shown in triangles and the secondary y-axis is given in number concentration. Regarding the crystal size, there are higher concentrations of crystals in smaller bins and negligible amounts in higher bins based on AIITS data. This agrees with the NASA probe measurements.

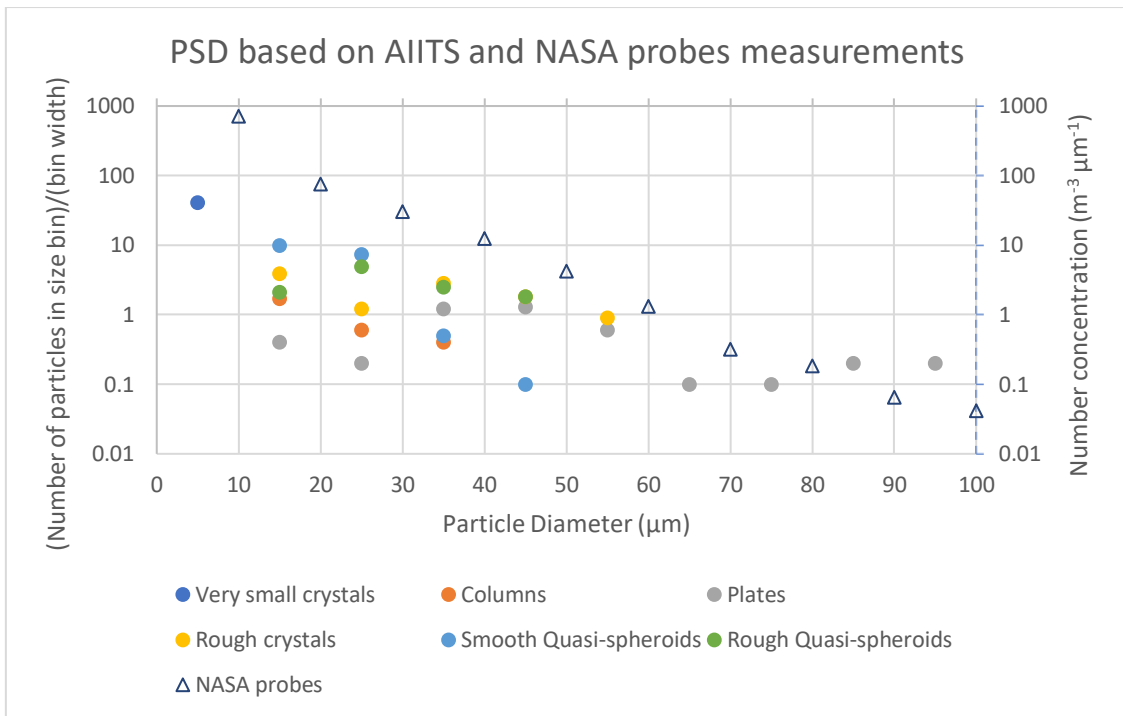
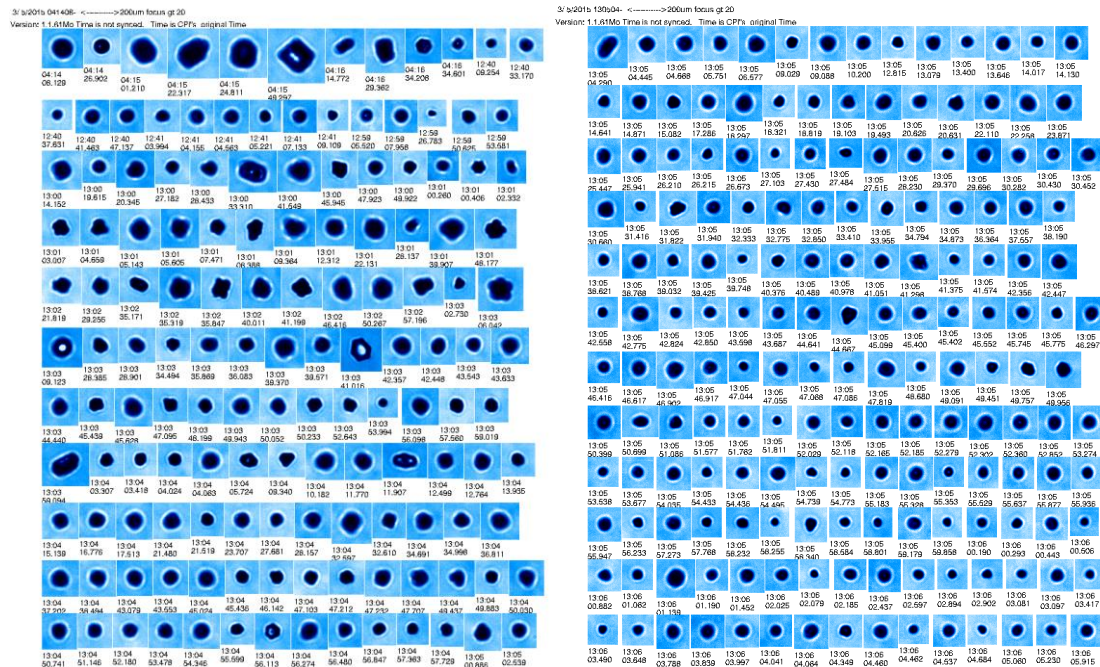


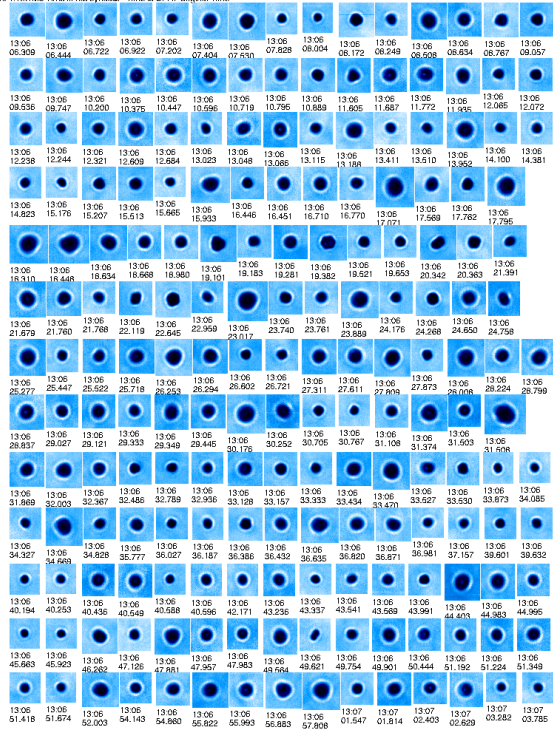
Fig. 6.24: PSDs measured by the NASA probes (triangles) and the AIITS (coloured based on crystal types) for the entire flight. Note that particle sizes ≤ 100 are only analysed.

A collection of ice crystal images taken by the CPI instrument during the 5th of March 2015 flight are given below (Fig. 6.25):



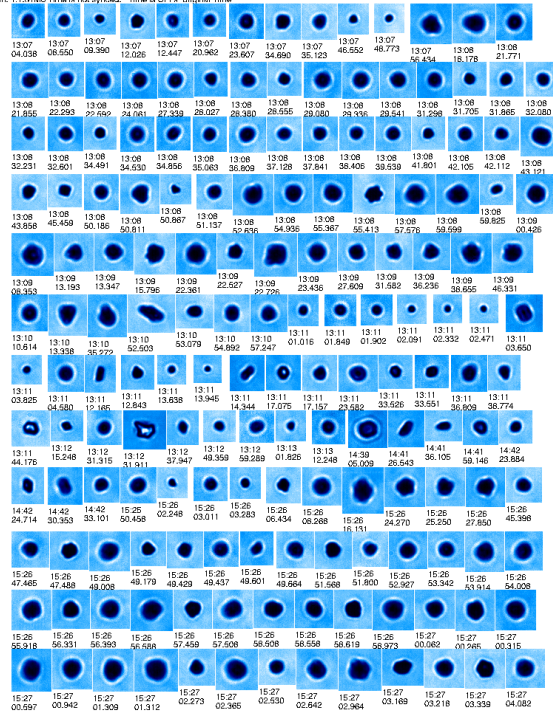
3/ 5/2015 130906: <----->200um focus qt 20

Version: 1.1.61Mo Time is not synced. Time is CPI's original Time



3/ 5/2015 130704: <----->200um focus qt 20

Version: 1.1.61Mo Time is not synced. Time is CPI's original Time



3/ 5/2015 152704: <----->200um focus qt 20

Version: 1.1.61Mo Time is not synced. Time is CPI's original Time

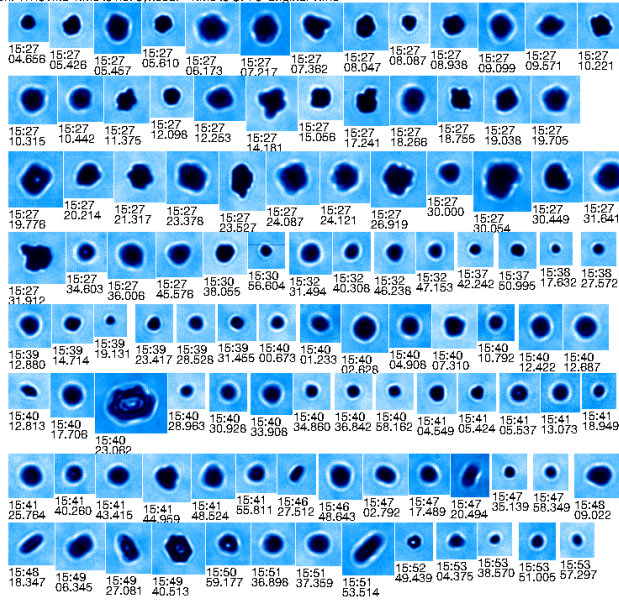


Fig. 6.25: Ice crystal images taken by the CPI instrument on 5th March 2015.

Regarding the crystal shape, it is evident that the CPI images in Fig. 6.25 are populated by plates, columns, and quasi-spheroids, which agrees with the AITS images (see Table 6.4).

6.3.2 Temperature and supersaturation

The temperature values were noted from the data files mentioned in Section 6.3 based on the timestamps and altitude. Between 8 and 18km, the temperature ranged between -83°C and -40°C.

Apart from temperature, ice supersaturation is another parameter which determines the type of the ice crystal formed in the atmosphere. Unfortunately, the ice supersaturation values were not recorded in the data files mentioned in Section 6.3. However, since the current study shows that there is an abundance in smaller crystal sizes, the ice supersaturation is very likely to be <10%. According to the habit diagram (Fig.2.2), the smaller crystals are found at all temperatures (0° to -70°C) when ice supersaturation is <10%. The results from 2014 ATTREX show that the mode of the distribution in supersaturation in cloud was approximately 3–5% (Woods *et al.* 2018). Therefore, based on the habit diagram analysis and findings from previous ATTREX TTL cirrus sampling, it can be concluded that the ice supersaturation levels were low (<10%) during the ATTREX 2015.

6.4 Results from related studies

In this research it was found that around 60% of crystals in the TTL clouds were quasi-spheroidal in shape having a diameter of 50µm or below. 47% were very small with a radius range of 1-5µm (see Fig. 6.20). The results from previous studies in Cirrus cloud confirm these findings. One such study is 2014 ATTREX, the details of which are given in Section 3.1. The results from the study sampling over the TTL cirrus of the Western Pacific were summarized in Woods *et al.* (2018) as *“Observed ice particles were predominantly small (<30µm) and quasi-spheroidal in shape, with the percentage of quasi-spheroids increasing with decreasing temperature. In comparison to the large fraction of the population consisting of quasi-spheroids, faceted habits (columns, plates, rosettes, and budding rosettes) constituted a smaller percentage of the overall population and exhibited the opposite correlation with temperature.”*

Another study, the Costa Rica Aura Validation Experiment (CR-AVE), sponsored by NASA conducted near San Jose, Costa Rica in 2006, the subvisible cirrus (SVC) clouds in the TTL from -75°C to -90°C were sampled. SVC clouds are clouds with very low ice crystal number concentrations having an optical depth lower than 0.03 (Spreitzer *et al.* 2017). The result show that based on the CPI images, 84% ice particles were quasi-spherical and larger particles (>65µm) exhibited disk-shaped and hexagonal plate characteristics (Lawson *et al.* 2008). The Fig 6.26 shows the SVC layer, taken during the transit flight for the CR-AVE.



Fig. 6.26: The SVC layer, taken during the transit flight from Houston for the CR-AVE (Lawson et al. 2008).

In another in-situ measurement, conducted on 18th March 1994 in cirrus clouds over southern Germany, the authors (Strom et al. 1997) report that, “Crystal concentrations were high (median 2.5 cm^{-3} , STP) and sizes small with a diameter of mean mass (average diameter of the sample) of typically $16 \mu\text{m}$ ”. The temperature ranged between -35°C to -60°C . They also mention that the cloud consisted of numerous small crystals with no crystals larger than $50\mu\text{m}$. In comparison, based on the research conducted in this paper, 97% crystals were found to have a diameter of $50\mu\text{m}$ or less.

In the next chapter automation of light scattering images using deep learning network is discussed.

7. PATTERN CLASSIFICATION USING DEEP LEARNING NETWORK

The process of manual classification of light scattering images of ice crystals is laborious and time consuming. It can lead to many pitfalls such as human error due to fatigue, inconsistent or unreliable results due to biases. For this reason, a Deep Learning (DL) program using MATLAB (version R2020b) was developed to automate the classification procedure for light scattering pattern images of ice crystals.

7.1 Deep Learning Network

A Deep Learning Network (DLN) can be built from scratch. However, it will take time for designing and training processes. Hence, the Transfer Learning method was used. By using the 'Transfer Learning', the network can 'transfer the learning' (low-level features such as edges, contour etc.) it has gained previously through large datasets. A pre-trained network trained on one dataset (for example, different types of objects, animals etc.) can be 'fine-tuned' to make it usable for classifying another dataset. The fine-tuning is carried out by replacing the final few layers of the network (see Section 7.3.3) and re-training the network with a new dataset; so that the network can unlearn the features from previous images (trained on a different image dataset) and learn the features specific to the new dataset.

The most commonly used convolutional neural networks for image classification are AlexNet, GoogLeNet and ResNet-50 (*Sharma et al. 2018*). The convolution layer is the core component of these networks where the features of the image get extracted, hence the name convolutional neural networks. The network consists of several layers with serial and parallel connections between them, and the output from the previous layer is often used as the input for succeeding layers. The number of layers as well as their arrangement varies with networks. There are only 25 layers in AlexNet while GoogLeNet has 144 and ResNet-50 has 177 layers. The image input size of AlexNet is 227x227x3 and that of ResNet-50 and GoogLeNet is 224x224x3. *Sharma et al. (2018)* report that AlexNet performed poorest in terms of prediction accuracy compared to the other two networks. Also, the input size of ResNet-50 is the same as for GoogLeNet. These are the two reasons for choosing both GoogLeNet and ResNet-50 for image classification in this research.

In the next two Sections, two major phases in developing the DL programme - Data pre-processing and Network training - are explained. Both networks, GoogLeNet and ResNet-50, are trained using a training set of AIITS images. Once the training is complete, the networks are tested using a test dataset containing AIITS images and their prediction accuracies are compared in Section 7.4. Additionally, in Section 7.5, both networks trained on AIITS images were tested for their applicability to images taken by a different light scattering instrument, the Particle Phase Discriminator version 2 (PPD2). For this, a test dataset of PPD2 images (which cover the same angular range as AIITS images) was used. The networks' prediction accuracies based on both test datasets were evaluated in Section 7.6.

7.2 Data pre-processing

The images that are used to train the network need to be compatible with the input image size of the network. As mentioned in the previous section, the image input size of GoogLeNet and ResNet-50 is same (224x224x3), hence the same data pre-processing steps can be followed for both networks.

The AIITS 2D light scattering patterns are greyscale images of 512x640 pixels. These images were cropped to 458x458 pixels, so that the outer angular region just touches the image border. The angular regions outside the 'ring area' (8° to 25°) were masked, so that only the scattering pattern remains. The process of finding the relevant region of interest is described below.

The AIITS images are not centred, but slightly offset towards the left-hand side, as can be seen in the first columns of Fig. 7.1. It was necessary to centre the images as well as to eliminate the background region for easier image processing in later stages. Therefore, a MATLAB script was developed to find the beam-stop and its centre, as well as the inner and outer radii of the scattering pattern in each image.

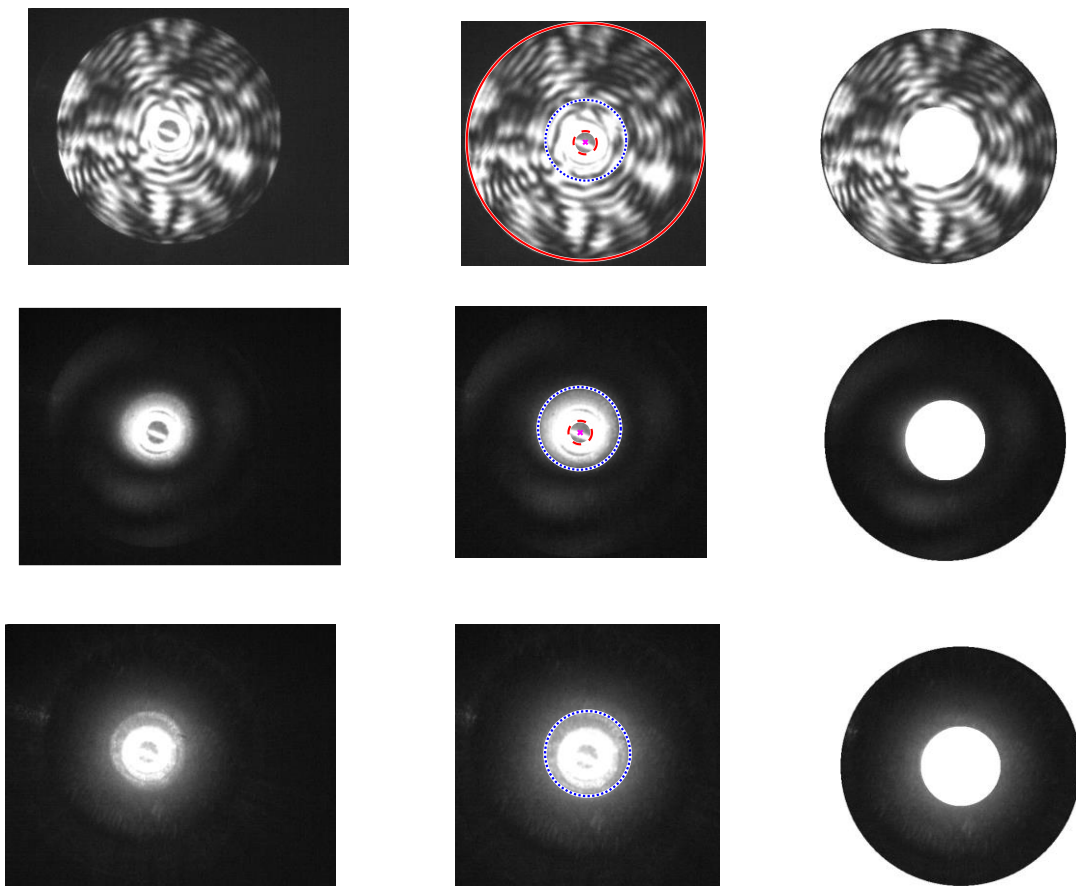


Fig. 7.1: Three different AIITS scattering pattern images are shown in each row. The first column shows the original scattering pattern images; the second column shows the cropped image with beam-stop, inner and outer circle marked in different colours; the third column shows the masked image with only the region of interest displayed.

Not all the AIITS images were identical regarding the visibility of parameters like the beam-stop, the inner and outer radii. That is, in some cases only one or two parameters were detectable. For example, three types of images are shown in the rows of Fig. 7.1. From left to right, the columns represent the original AIITS image, the cropped image with parameters marked, and the final, masked image, displaying only the area of interest. In the first example, which is AIITS no. 2190, all parameters were detected (see first row, second column). The solid red line represents the outer radius. The inner radius is shown in blue dotted lines, the beam-stop in red dotted lines and the beam-stop centre is marked by an 'X' in pink colour.

The images in the second row show AIITS no. 24, which has comparatively low overall brightness and is likely to be the scattering pattern of a very small crystal of size 1-5 μm in radius. All parameters except the outer radius were detected. Whereas only the inner radius was detected in the bottom row of Fig. 7.1 showing AIITS no. 6.

Since the detected parameters vary with images as mentioned above, the programme in Appendix 11.4 is used to find the mean values of the parameters. After running the programme for all the images in the AIITS database, the parameters of each image were saved to a text file and the mean value of the centre, the inner radius and the outer radius were found to be [229,229], 75 and 224 pixels respectively.

A built-in function *'imfindcircles'* in MATLAB has been used to detect the beam-stop centre as well as the inner and outer radii of the scattering pattern image automatically. (In MATLAB, by using this function on an image with explicitly stating the radius range, it will return the centres of the circles along with their radii within the specified radius range.) After the circles of specific radius ranges are detected, they can be visualised using a function *'viscircles'* with the relevant centres and radii. This is shown in the middle column of Fig. 7.1. The first and the last columns of Fig. 7.1 show the images before and after formatting, respectively. That is, the former represents the original AIITS image, and the latter represents the cropped and masked image containing the relevant information with other regions masked by setting the intensity to a maximum value of 255. Note that the inner angular region contains the artefact ring which is visible just outside the beam-stop. Even though AIITS captures the scattering pattern in the angular range of 6° to 25° of the forward scattering hemispheres, sometimes they contain artefacts up to 8° as can be clearly seen in the 2nd and 3rd row of Fig. 7.1. This is the reason for choosing the inner radius as 8° instead of 6°. Therefore, the evaluable information is contained between the two angles 8° and 25° (corresponding to 75 and 224 pixels).

There are also images in the AIITS database that do not contain any useful information. Examples are shown in Fig. 7.2. The first image is completely blank, the second image only contains the beam-stop at the centre and the third image shows the beam-stop along with an artefact or ring just outside the beam-stop. All three types of images are counted as 'Blank' as they do not contain any information related to crystal type.



Fig. 7.2 Images that are counted as 'Blank Images'.

As the final step of data pre-processing, resizing of images from 458x458 to 224x224 pixels and conversion to colour images was necessary to make them compatible with the input size of the networks, which is 224x224x3. An *'augmentedImageDatastore'* function is used for this purpose (see Section 7.3.3). The data pre-processing workflow is shown in Fig. 7.3. The resulting image was used in the Input Layer of the DLN.

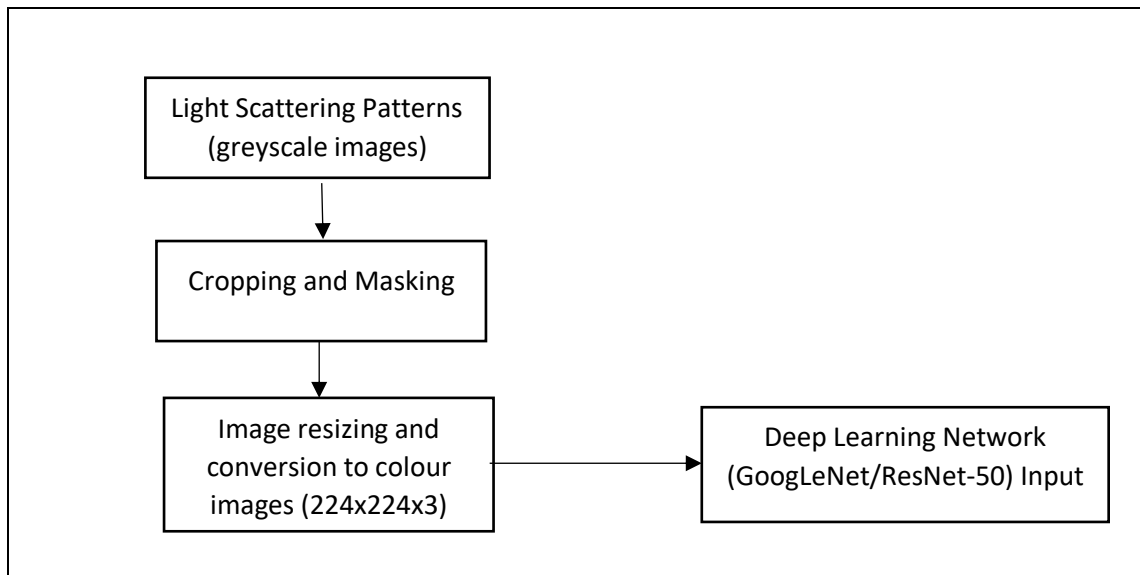


Fig. 7.3: The methodology of Data Pre-processing for DLN.

7.3 Network Framework and Training

A brief discussion on the training dataset and training options are presented in this section. Pre-requisites: Add-ons such as the Image Processing Toolbox and Deep Learning Toolbox should be installed in MATLAB.

7.3.1 Overcoming the data challenge

Some crystal morphologies are not well represented in the AIIITS database making it difficult to generate training sets of a suitable size. However, the training set can be artificially increased by replicating the images through flipping and 90° rotations. This, in turn increases the diversity of different crystal orientations in the training set. The replicated images were of RGB image type of bit depth 24 and the AIIITS scattering patterns were grayscale images (.jpg) of bit depth 8. The differences in image type are addressed in the pre-processing stage mentioned in Section 7.2 and all images are converted to RGB images.

7.3.2 Training dataset

The dataset which is used to train the network is important, as the network learns and performs based on this dataset. The criteria for selecting images for the training dataset was based on those mentioned in Lindqvist *et al.* (2012). That is, the images for the training set were selected to cover a variety of crystal size and orientation. Also, the selected images have features of crystal habits recognizable and representative of its class, thereby avoiding overlaps within the categories.

The training data set consists of a total of 80 images, including original AIIITS scattering pattern images as well as replicated images as mentioned in Section 7.3.1. The images were cropped and masked and there were 5 crystal categories (Blank, Patterned, Plates, Columns and Rounded) with 16 images in each category. It is also recommended to have equal number of images in each category to avoid biases towards certain categories. Due to time constraints, a small dataset with a few categories was chosen for training. Note that the 'Blank' category refers to images like the ones shown in Fig. 7.2. The rough crystals and quasi-spheroids are

referred as 'Patterned' and 'Rounded' categories respectively. The same training dataset consisting of AITS images is used to train both networks.

7.3.3 Designing the Network

The DLN was designed using the Deep Network Designer App in MATLAB. Prior to designing the network, the images for training were made available in the MATLAB workspace. To achieve this, these steps are followed: First, load the main folder (crystal category) containing the training dataset into the MATLAB workspace using the 'ImageDatastore' function. Set the parameters 'IncludeSubfolders' to 'true' and 'LabelSource' to 'foldernames'. This setting enables the network to follow supervised learning and use the subfolder names (Blank Images, Columns, Patterned, Plates, and Rounded) as the crystal categories. In supervised learning, the network is trained using a labelled dataset so that the network knows what features to expect in each category. Next, an 'augmentedImageDatastore' function is used to resize and convert the greyscale to RGB images to make it compatible to the input layer of the DLN (see Section 7.2). After executing these steps, the training dataset will be available in the MATLAB workspace.

In the next step, the pre-trained network is loaded using Transfer Learning. This can be achieved by following the options MATLAB-> Apps-> Deep Network Designer-> Pre-trained Network-> GoogLeNet (or ResNet-50). Then the network's final three layers are replaced by *FullyConnectedLayer*, *SoftmaxLayer* and *ClassificationOutputLayer*.

FullyConnectedLayer: As the name indicates, all neurons in this layer are connected to all the neurons in the previous layer. This helps to identify the larger patterns and classify the images (based on the output size) by combining the (smaller) features learned by the previous layers.

SoftmaxLayer: It converts the unnormalized prediction scores from the fully connected layer to a normalized probability distribution (between 0 and 1). The score across different categories adds up to 1.

ClassificationOutputLayer: This layer deduces the number of categories from the output size of previous layer and associates the categories with the scores. The category with the highest score will be chosen as the predicted class.

Drag and drop the layers from the Layer Library on the left side in the specified order to make the network specifically suitable for this research, to classify crystals. Set 'OutputSize' of the *FullyConnectedLayer* to 5 (the number of crystal categories). This is the design phase shown in Fig. 7.4, where the final layers of the network are zoomed in. Then click 'Analyze' which checks the network and displays any warnings or errors.

The next step is the Data importing stage in which the 'Data' tab, next to the 'Designer', is selected. From the drop-down list, select 'Image Datastore in workspace' as the data source and then 'Import'. This is shown in Fig. 7.5. The data for both training and validation can be set here, and the same pre-processed dataset is used for both. The default setting of 30% of images from the training set is used for validation. Validation data is a set of images that are used to test the network during the training process and is different from the test dataset (which is used to test the network after the network is trained).

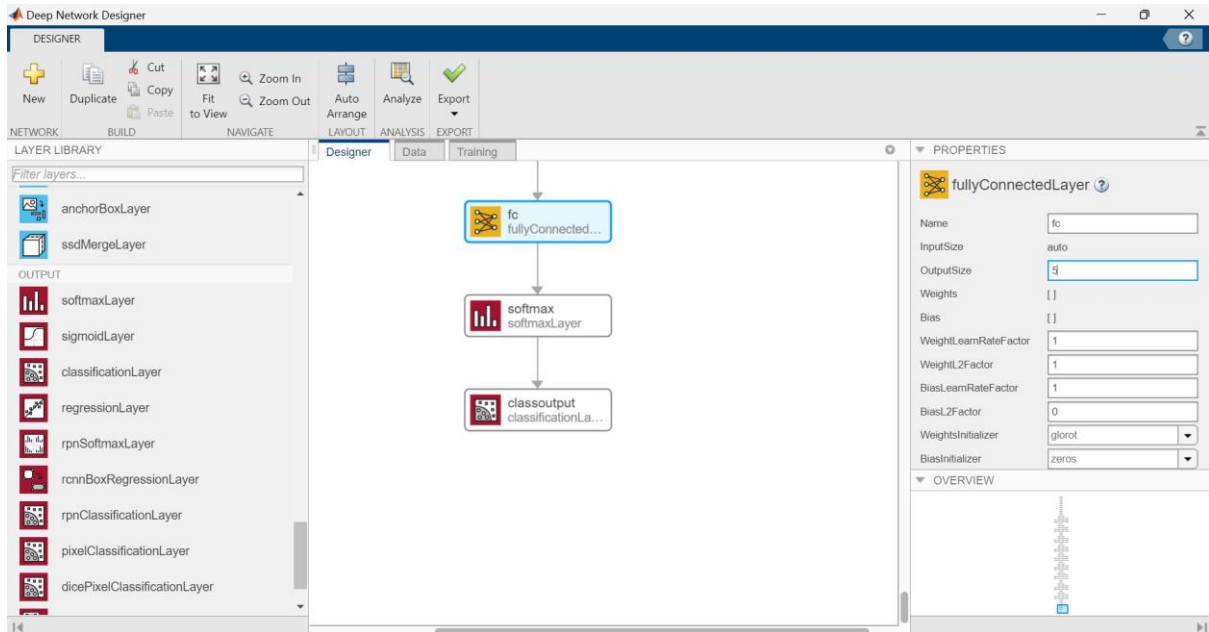


Fig. 7.4: The design phase where the final three layers are replaced, and the Output size is changed to five.

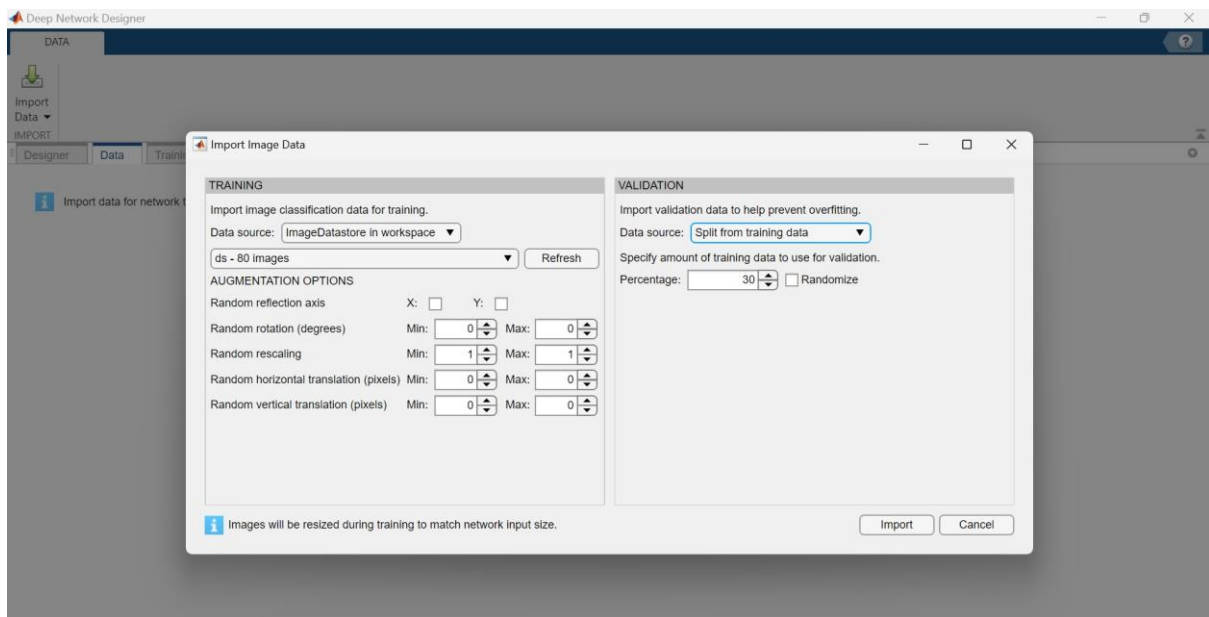


Fig. 7.5: Setting the training dataset.

The final phase is the training phase where several training options (like Initial Learning Rate and Epochs) are available. The Initial Learning Rate was set to 0.001, which helps the network to learn slowly. Its default value is 0.01. On increasing the Initial Learning Rate, the network training will be faster, but results in increased prediction inaccuracies. The training was done in 4 Epochs. An epoch is passing the entire training dataset through the neural network in one cycle. Here, 4 epochs correspond to passing the entire dataset 4 times through the neural network for training. Other parameters were set to default values. Then select 'Train' to train the network using the training dataset and 'Export' to export the trained network to the workspace. After training, the progress and results will be shown as in Fig. 7.6.

In the MATLAB editor write 'save <trainedNetworkName>' to save the trained network. The same process of data pre-processing, designing, and training is followed for both networks.

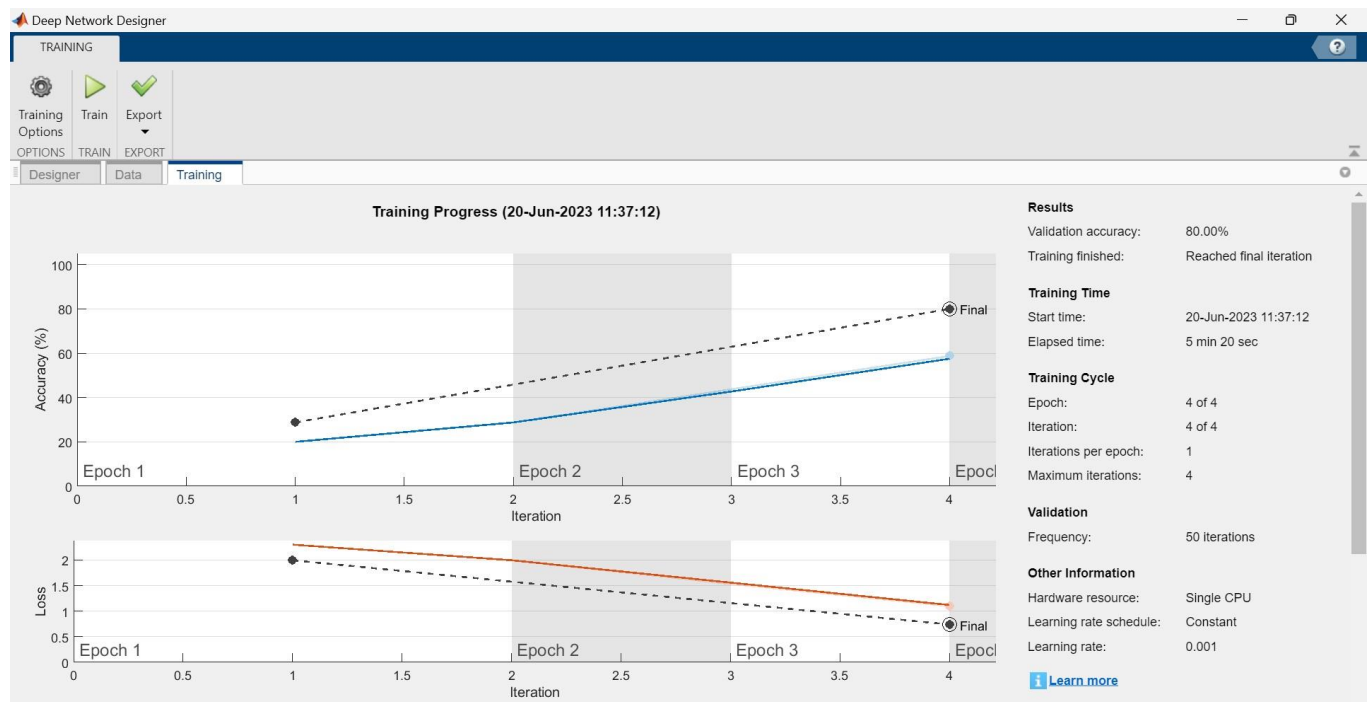
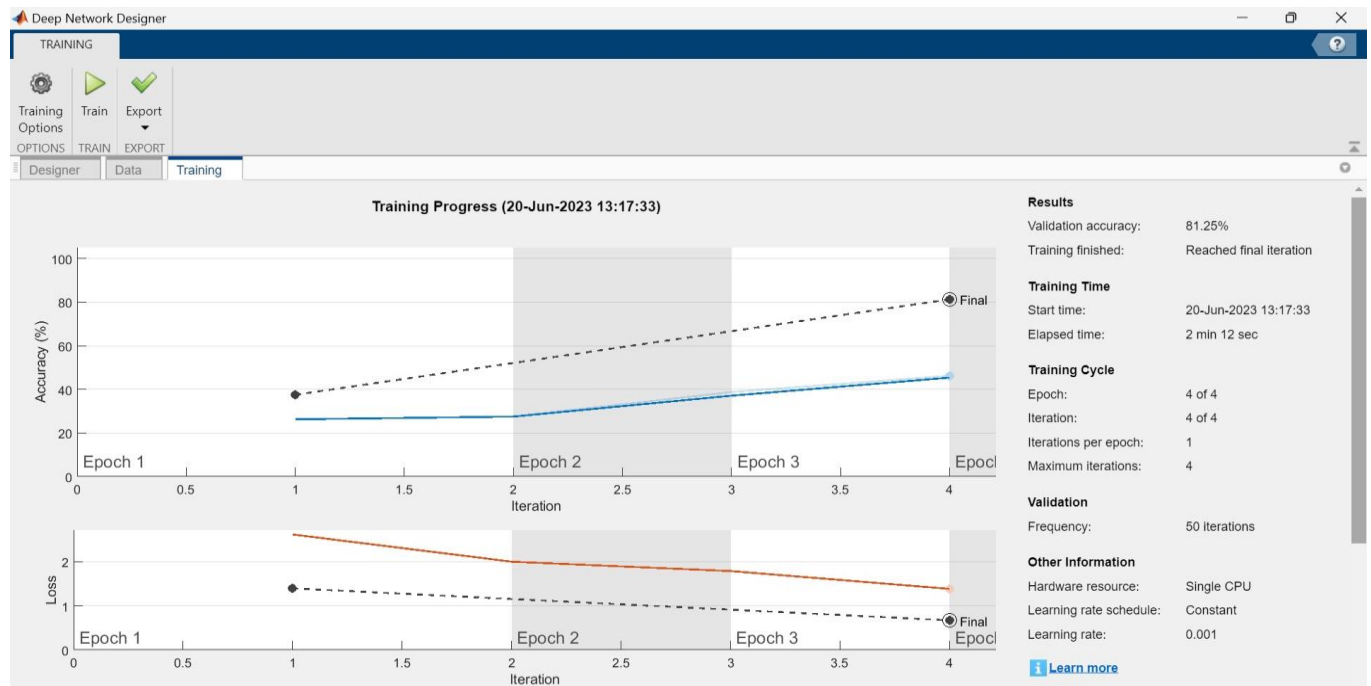


Fig. 7.6: The training progress results of GoogLeNet (top) and ResNet-50 (bottom). The black dotted line represents the validation dataset in both plots. The blue and red line represents the accuracy and loss of the training dataset, respectively.

Based on the training results, the training accuracy (blue line) of GoogLeNet is around 50%, while that of ResNet-50 is 60%. The training accuracy is the classification accuracy based on the images it was trained on. The training loss (red line) is the cross-entropy loss between network predictions and target values computed on the training set (*Matlab R2019b*). The training loss is around 1.5 for GoogLeNet and 1 for ResNet-50. The validation loss (dotted line), the cross-entropy loss computed on the validation dataset, is less than 1 for both networks. More simply, the loss is the predictive inaccuracy of the network (*Matlab R2021a*). The lower the loss, the better the prediction.

Overall, the validation accuracy of GoogLeNet is slightly higher (81.25%) than that of ResNet-50 (80%). The validation accuracy provides the fraction of the predicted category that matches the true category in the validation dataset. This can be further improved by increasing the number of images in the training dataset and by changing the training options (hyperparameters). The optimum values of the Initial Learning Rate, Epoch, and other training hyperparameters varies with the dataset and can only be found by testing with different values until training accuracy flattens (stops improving). Due to time constraints, these are not investigated further.

7.4 Assessing the Networks' prediction

All the images in the test dataset were manually classified as one of the five categories. Accuracy of the networks were assessed by comparing the predicted results of the network with that of manual classification. Some assumptions are made while assessing the networks' accuracies. It is assumed that the manual classification is 100% correct, just like in other applications (*O'Shea et al. 2016*).

As reported in Lindqvist *et al.* (2012), there are cases where the crystal habit becomes subjective. That is, more than one category can describe the crystal type equally well. For example, the rounded crystals often have uneven rings or a speckle-like pattern which can affect the network's prediction due to overlaps between categories. In such cases, images belonging to the 'Rounded' category are predicted as 'Patterned' by the network. Even manual classification is sometimes biased toward one category (*O'Shea et al. 2016*).

7.4.1 Test dataset

The test dataset comprises a total of 50 AIITS light scattering images of five crystal categories. If a network predicts too well or poorly for a specific category, the network's accuracy can be biased to that category. For this reason, the same number of (10) images in each category are used as test data. Also, the same test dataset consisting of AIITS images is used to test both networks. The data pre-processing steps are applied to the test dataset before it is fed to the trained network for testing.

7.4.2 The Networks' prediction

There are two versions of the program. The first version is for analysing an individual image after calling it from the test dataset. The network predicts the probability of crystal type in the form of a horizontal bar chart in descending order. An example is shown in Fig. 7.7, in which the program correctly categorizes the scattering pattern of a rough crystal as 'Patterned'. This is based on GoogLeNet; on changing the network to ResNet-50 in the program, the prediction (similar to Fig 7.7) based on ResNet-50 can be obtained.

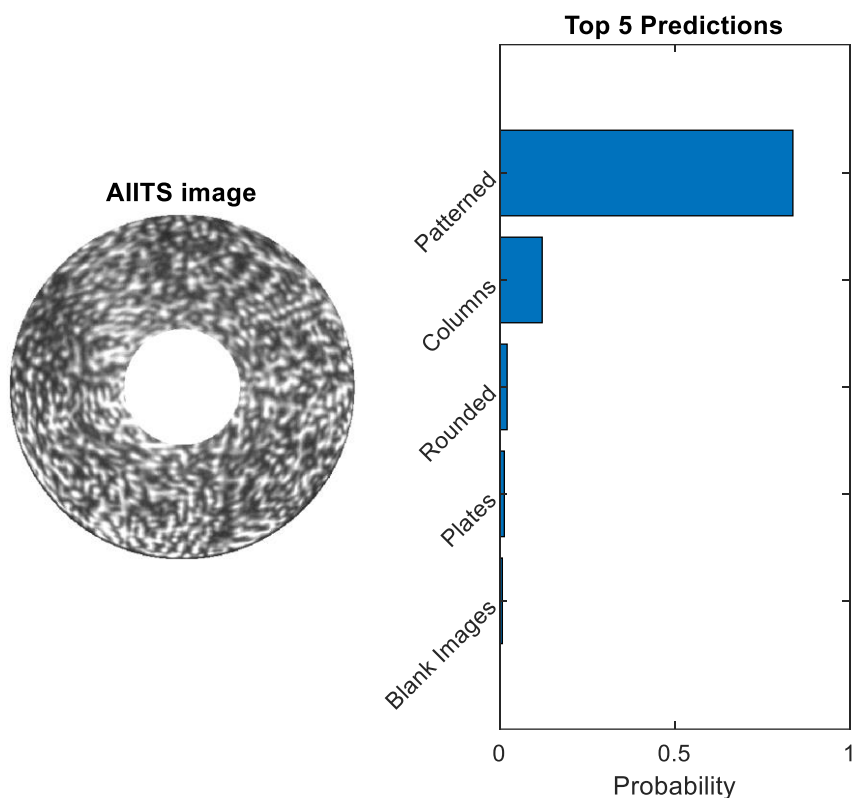


Fig. 7.7: AIITS light scattering pattern image (left) and the probability of crystal type predicted by the GoogLeNet (right).

In the second version of the DLN program, a folder of images is analysed and the prediction result (crystal type) with highest probability is written into an Excel sheet. This helps in a faster comparison of results and for checking the overall prediction accuracy of the network. Also, the results in the Excel sheet can be used to plot the manual classification (also called True Class) against the predicted classification (Predicted Class), which is often known as a Confusion Matrix. The Confusion Matrices of GoogLeNet and ResNet-50 are given in Fig. 7.8. The blue and orange colours correspond to correct and incorrect observations respectively. Also, the strength of the colour increases with cell value. The values in the Confusion Matrix cells add up to 50 corresponding to 50 images in the test dataset.

The diagonal cells (top left to bottom right) represent correctly classified categories, while the off-diagonal cells represent mis-classified categories. Overall, 32 out of 50 images were correctly predicted by the GoogLeNet resulting in 64% network accuracy. On comparing the manual classification of crystals with the prediction of ResNet-50, only 23 images were correctly predicted, resulting in 46% network accuracy. On the right side of the confusion matrix, row summary is also provided, in which a percentage of both correct and in-correct observations in each category can be seen. Category-wise, Blank Images, Columns, and Patterned were predicted with 100%, 80% and 90% accuracy respectively by GoogLeNet. In comparison, ResNet-50 predicted the categories Blank Images and Patterned with 100% and 70% respectively. Both GoogLeNet and ResNet-50 predicted the crystal classifications 'Plates' and 'Rounded' with an accuracy of 20% and 30% respectively. This shows that both networks need improvements to correctly predict the Plates and Rounded categories. Additionally, ResNet-50 needs improvement in the 'Columns' category.

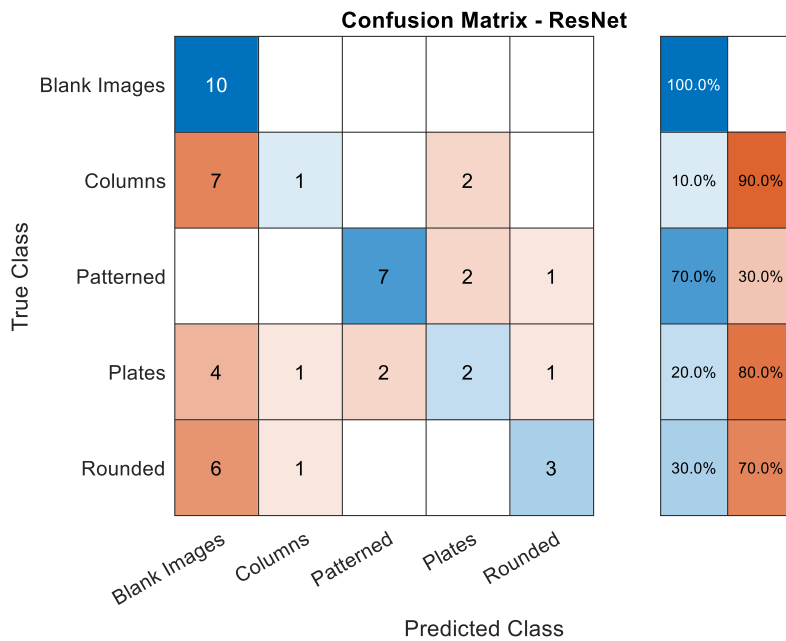
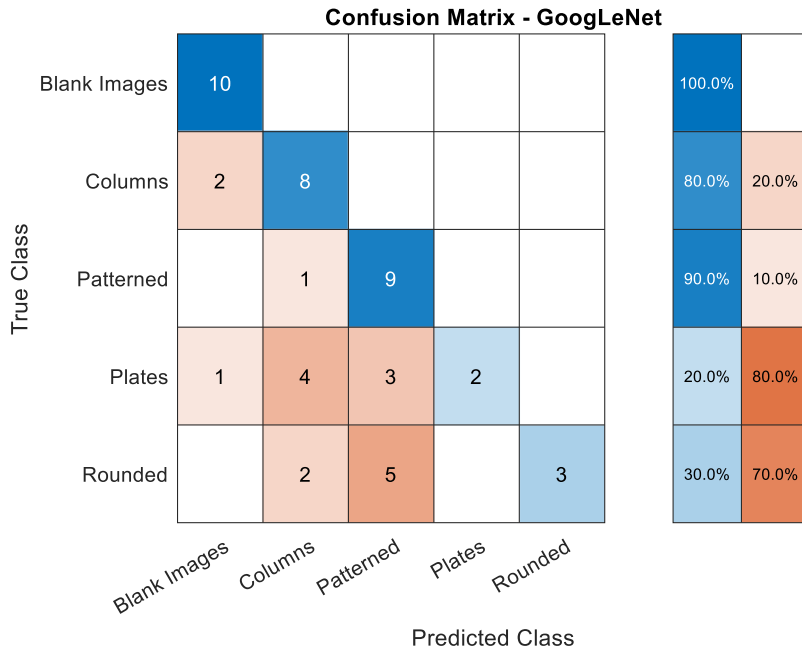


Fig. 7.8: The Confusion Matrix charts of GoogLeNet (top) and ResNet-50 (bottom) tested on AIITS images.

So far, the light scattering images taken by the AIITS (used for both training and testing) have been discussed. In the next section, the networks trained on AIITS images are tested on the light scattering images taken by another instrument to check the usability of the network. Note that, the new test dataset is solely for testing the network's usability and is not related to the research flight this paper is focused on.

7.5 Testing the trained networks with PPD2 images

The Particle Phase Discriminator (PPD) is an optical scattering instrument that takes high resolution light scattering patterns (Kaye *et al.* 2008). Just like AIITS, PPD captures the scattering pattern in the angular range of 6°-25°. Hence, images taken by the PPD, more specifically, the second version PPD (PPD2) are used as another test dataset to check the usability of the trained networks.

PPD2 images are .bmp type greyscale images (bit depth of 8) with 768x582 pixel dimension. Since the images vary in terms of dimension, compared to AIITS images, the parameters were re-calculated using the program in Appendix 11.4. The centre, as well as the inner and outer radius of the scattering pattern were found to be [290, 290], 76 and 289 pixels respectively. The images were also cropped and masked.

There were 140 PPD2 images in the test dataset with a random number of images belonging to each of the five categories. The confusion matrices of GoogLeNet and ResNet-50 are shown in Fig. 7.9. Overall, GoogLeNet predicted with 55.7% accuracy while ResNet-50 predicted with only 17.86%. In terms of categories, GoogLeNet predicted the 'Blank Images', 'Columns' and 'Patterned' with over 75% accuracy. However, ResNet-50 predicted with <20% for all categories except for 'Patterned' (92.3%).

The results show that it is possible to use the networks trained on AIITS images to categorize the PPD2 images. Since both images have information contained in the angular range of 6°-25°, the same trained networks can be used readily for classification purpose. The only additional step taken is regarding the data pre-processing. That is, due to the differences in image dimension, the AIITS and PPD2 images have separate lines of code in the data pre-processing program.

Confusion Matrix - GoogLeNet

True Class	Blank Images	23	7				76.7%	23.3%
	Columns		29	1	6		80.6%	19.4%
	Patterned		1	11	1		84.6%	15.4%
	Plates		4	11	10		40.0%	60.0%
	Rounded		9	20	2	5	13.9%	86.1%
		Blank Images	Columns	Patterned	Plates	Rounded		
		Predicted Class						

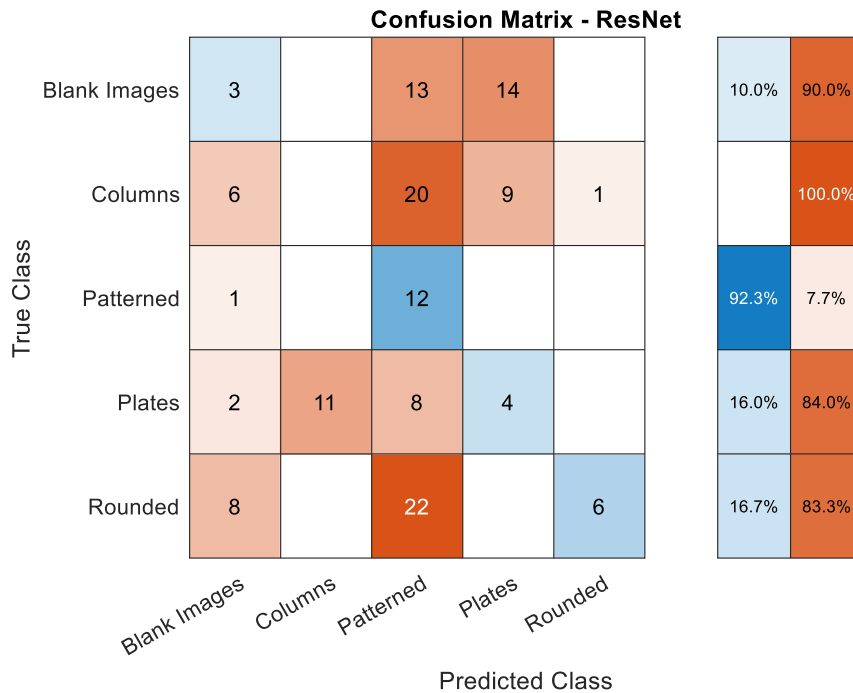


Fig. 7.9: The Confusion Matrix chart of GoogLeNet (top) and ResNet-50 (bottom) tested on PPD2 images.

7.6 Discussion of the results

The following trends are observed on analysing the images in the test datasets taken by two different optical scattering instruments (AIITS and PPD2), based on two neural networks (GoogLeNet and ResNet-50):

- The overall accuracy of the network varies with the test dataset.
- Different networks show different accuracy rates even though the same test dataset is used.
- The prediction accuracy varies between category levels. That is, some networks identify some categories (classes) within the test dataset better than others. For example, GoogLeNet performed well on categories like 'Columns' and 'Patterned' while it failed on the 'Rounded' category.

All of these trends can be seen in Sharma *et al.* (2018), as they analysed 10 categories from two popular datasets (containing images of furniture, vehicles etc.) using three trained networks, AlexNet, GoogLeNet and ResNet-50.

In general, the results show that the same trained network can be used to test images taken by AIITS as well as PPD2. For AIITS and PPD2 images, GoogLeNet predicted with an accuracy of 64% and 55.7%, while ResNet-50 predicted with 46% and 17.86% accuracy, respectively. On average, GoogLeNet predicted with a higher accuracy of 60%, compared to ResNet-50 (32%). This result is similar to the findings by Sharma *et al.* (2018), who report that the accuracy rate of GoogLeNet varied from 64.40% to 71.67% on two datasets and outdid the other networks (ResNet-50 and AlexNet).

If a crystal habit that is not included in the training set is used in the test set, the network will classify it as the best matched category. For example, in the test dataset containing the AIITS images, some droxtals and a pristine scalene plate were used to check whether the networks categorize them correctly. It was found that pristine scalene plate was correctly identified as

'plates' by both networks, even though the training set only contained scattering images of regular hexagonal plates. However, droxtals were misclassified as 'Blank Images', 'Patterned' or 'Columns'.

One of the reasons for misclassification is the insufficient number of images in the training dataset. That is, the networks were trained with very small numbers of images belonging to five categories due to lack of data and time constraints. This might be the reason for the failure of networks to classify 'Plates' and 'Rounded' categories correctly. By increasing the number of images in the training dataset, hopefully the network can learn more and predict with higher accuracy.

Another reason for misclassification is the overlap between categories. It is sometimes difficult to distinguish between the categories. For example, 'Plates' are sometimes misclassified as 'Columns', 'Blank images' or 'Patterned'. Manually, it is easy to identify 'Plate' patterns as the ones with four to six major arcs and 'Column' patterns as those with two arcs. However, the network may fail to detect these specific features in the scattering pattern. For instance, variations in the arcs' brightness may cause the network to detect only two out of six arcs and hence classify 'Plates' as 'Columns'. Weak (dim) images can result in predicting 'Plates' as 'Blank Images'. Slight imperfections in plates can make the scattering pattern of plates to contain features other than the arcs. In such cases, 'Plates' may be classified as 'Patterned'. Therefore, in reality, it may not always be possible to assign crystals to one specific category. Overlaps across different categories are expected in DLN and are reported by several authors (*Sharma et al. 2018, O'Shea et al. 2016, Lindqvist et al. 2012*).

GoogLeNet can be readily used to classify both AIITS and PPD2 images as the network performed with an average accuracy of 60% on image classification. However, the network need improvement for 'Plates' and 'Rounded' categories. Also, five categories do not adequately represent the variety of crystal types occurring in cirrus. Hence, network re-training is recommended by expanding the crystal categories as well as increasing the number of images in each category, to further increase the usefulness of the network in future.

8. CONCLUSIONS AND FUTURE WORK

Cirrus clouds play a crucial role in the Earth's radiative balance. The radiative properties of such clouds are very much determined by its constituents. The size, shape, and roughness of the ice crystals - all play an important role and this is the focus of the current study. *“The sizes and shapes of ice crystals affect fundamental microphysical processes, such as sedimentation, vapor growth, and aggregation, as well as cloud optical properties...Furthermore, microscale roughness structures on crystal surfaces and other crystal distortions appear ubiquitous and substantially affect crystal scattering properties.”* (Diedenhoven et al. 2020).

Although direct imaging instruments like the CPI can be used to determine the shapes of larger crystals, the surface texture may not be accurately assessed. Also, for smaller crystals ($<30\mu\text{m}$), the habit identification is difficult since the resolution of such instruments is insufficient. The light scattering instrument AIITS is particularly useful in such cases. In this thesis, the properties of individual ice crystals were investigated based on the light scattering pattern images taken by the AIITS at the wavelength of 532nm in the TTL cirrus over the Eastern Pacific during Airborne Tropical Tropopause Experiment on 5th March 2015.

Of the 2426 images obtained, only 876 images were suitable for analysis. The discarded images were either blank or only contained an artefact in the centre. The results presented in Chapter 6 were compared with CPI images and data obtained from other NASA probes during the same flight. Previous TTL cirrus studies also support the current findings.

In general, crystal habits like quasi-spheroids (60%), columns (23%), and plates (5%) were found. The crystal images taken by the CPI during the same flight (Fig. 6.25) also validate this finding. The results are consistent with previous studies: Based on the data from 2014 ATTREX campaign, the authors (Woods et al. 2018) state that *“The sparsity of aggregates in the CPI images obtained during ATTREX strongly suggests that particle aggregation is negligible in TTL cirrus”*. In agreement with this, no aggregates were found during the current investigation. The authors also state that the faceted habits constituted a smaller percentage of the overall population. In the current study, only 0.6% of the total crystal population comprised pristine plates. Another cirrus sampling flight conducted on the 11th and 13th March 2015 (O’Shea et al. 2016) report that *“Pristine plates were observed during both flights, but they only account for a small proportion of the total crystals (less than 2%)”*. In addition, during current study, it was found that 12% of the total crystal population were rough crystals with unknown shape. The percentage of rough crystals increases to 26.6% if rough surfaced columns, plates, and quasi-spheroids are also included. This is an important finding, that over a quarter of the crystal population possess a rough surface. This is a key microphysical property, which might have gone undetected if solely direct imaging was used.

In terms of crystal sizes, a general trend of the total number of crystals decreasing with increasing crystal size was observed. While 47% of crystals were found to have a diameter $\leq 10\mu\text{m}$, only 3% accounted for a diameter $\geq 50\mu\text{m}$. Majority of the crystals (83%) were found to have a diameter $\leq 30\mu\text{m}$. It was also found that over half of the crystal population possessed rounded edges. These findings agree with the results from 2014 ATTREX sampling over the TTL cirrus of the Western Pacific summarized in Woods et al. (2018), *“Observed ice particles were predominantly small ($<30\mu\text{m}$) and quasi-spheroidal in shape.”* The PSDs based on AIITS data and NASA probes have been analysed and the results agree that there are higher concentrations of small crystals.

The temperature varied between -40 and -83 °C at an altitude of 8-18 km. Though the ice supersaturation values are not available, the abundance of smaller crystals indicates ice supersaturation below 10%. This conclusion is based on analysing the habit diagram (Fig. 2.2) and results from 2014 ATTREX sampling. In both cases, smaller crystals were found at low ice supersaturation levels (<10%).

The morphology of the crystals was identified by analysing the features in the 2D light scattering patterns which carry information about their geometries. By successive testing and closely studying these features, crystals were classified. For this, a combination of analysis as well as computer modelling techniques were used.

If the scattering patterns only contain speckle-like features, the crystals are categorized as rough with unknown shape. The degree of roughness was computed using the 'Combined Roughness' method described in Ulanowski *et al.* (2014). The size of rough crystals was estimated by means of the 'Speckle Analysis' method (Ulanowski *et al.* 2012) based on greyscale morphological reconstruction. It was found that using a constant Marker value (=0.6xImage) may not work accurately for all images. While using 0.6 as the Marker value, the crystal sizes were underestimated especially for crystals larger than 30µm. On testing, overall, 0.75 is the best Marker value as the predictions were comparatively better for the crystal sizes between 10-100µm. However, rather than using a constant Marker value for all images, it is strongly recommended that the binary image created using the morphological reconstruction is compared with the original image to make sure the speckles are of same size to get an accurate estimate. It was also found that while using a constant marker value, the result varies with image dimension. As the Marker value increases, the window size (or the 'Marking' of speckles) decreases. Therefore, on using a larger Marker value like 0.9 for a smaller crystal, crystal size will be overestimated.

If features other than speckles can be seen in the scattering pattern, the crystals are categorized as quasi-spheroids, plates, columns etc. depending on their unique features (rings, arcs etc.) in the scattering pattern. The size estimation process varies with habit. For example, in a quasi-spheroid crystal's case, the sizes are estimated based on the number of rings. As the crystal size increases, a greater number of rings will be visible. For plates and columns, the width of the scattering arc should be analysed. While the scattering arc's width can be used to estimate the length of a column crystal, the same can be used to evaluate the radius of a plate crystal. This is due to their orientation resulting from the atmospheric drag force as columns align with their prism facets (long axis) perpendicular to the gravitational force, but plates with their basal facets. Additional features like position and number of minima can also be analysed for a more accurate estimate. Droxtals, a variant of plates with multiple facets, show both scattering arcs as well as bright spots in their scattering pattern. Just like plates, their radius can be estimated by examining the width of the scattering arcs. Irrespective of the crystal type, a cross-like pattern is usually evident in the scattering patterns of crystals with aspect ratio close to one, implying that the crystal diameter is about equal to the crystal length (equiaxed).

A variety of ice crystals models in different orientations and aspect ratios were used to simulate the light scattering patterns using the BTM (Hesse *et al.* 2018, Taylor 2016). The simulated patterns were then compared to the AITS images to estimate the crystal shapes and sizes. Overall, the scattering patterns of model crystals presented in chapter 5 show a good agreement with the AITS patterns.

Manual analysis of scattering patterns is time consuming and laborious. Therefore, a pilot study using Deep Learning Networks has been conducted to classify the light scattering images captured by the AITS into five categories: Blank images, Columns, Plates, Patterned and Rounded. Based on Transfer learning, two pre-trained networks, GoogLeNet and ResNet-50, were used for this purpose, and their prediction accuracies are analysed to find the best network. The same training dataset consisting of 80 AITS images (16 images in each of the

five categories) was used to train both networks. The prediction accuracy of GoogLeNet was then compared with ResNet-50 using the same test dataset of 50 AIITS images. In addition, to check the re-usability of the network on images taken by another light scattering instrument, another test dataset of 140 images obtained from the PPD2 was used to test both networks. On testing both networks with the two test datasets, GoogLeNet performed with an average prediction accuracy of 60% while ResNet-50 scored 32%. However, the prediction accuracies for categories, 'Plates' and 'Rounded', were the lowest among other categories. Furthermore, five categories are insufficient in terms of representing the crystal varieties occurring in the cirrus clouds. By expanding the network's training set by adding more categories as well as more data in each category and re-training the network, hopefully the crystal classification can be made easier in future. However, this was outside the scope of this research due to time constraints. The current network was trained on a single CPU, but if the need arises to train the network with a large dataset, parallel processing is advisable. Although the existing network is trained specifically by the AIITS images, the results show that GoogLeNet performed equally well on PPD2 images. Hence, the network (GoogLeNet) can be used for the image classification of scattering pattern images taken by different light scattering instruments. If the image dimension, the mean values of the centre and the outer and inner radii of the image taken by other instruments are different from those of AIITS images, they can be re-calculated using Appendix 11.4. Also, the pre-processing steps in the DLN program [Appendix 11.5] re-size the image as well as convert it to RGB to make it compatible with the DLN.

In this investigation, it has been demonstrated how the crystal shape, size, edge roundness, surface texture and orientation can affect the scattering pattern. For a more accurate estimation of the crystal geometry, detection of scattering patterns both front and side view of the crystal is recommended. Since the AIITS only captures $6^\circ \leq \theta \leq 25^\circ$ of the forward scattering, the details beyond 25° are missed out. Though it is impractical to get the pattern $< 6^\circ$ because of the high intensity laser beam near the centre, detecting scattered light at larger angles ($25^\circ \leq \theta \leq 90^\circ$) would be advantageous.

Overall, through this study of light scattering patterns, crystal habits in the 1-100 μm size range were determined much more accurately compared to direct imaging. This is an important size range which is frequently observed in cirrus cloud, but often overlooked. O'Shea *et al.* (2016) state that "*Most nucleation occurs at the lowest temperatures near cloud top where the crystals are mostly small. An optical array probe observes small ice (<100 μm) at all levels in both clouds [2 flights sampling in cirrus clouds] suggesting ice nucleation at all levels. This includes regions at temperatures too high for homogeneous nucleation (>238 K).*" There are cases where smaller crystals are regarded as shattered ice or artifact due to the partial observation of miss-sized larger particles (O'Shea *et al.* 2016, Guignard *et al.* 2012), missed by the detecting instruments (Liou 1986), misclassified as quasi-spheroids (Woods *et al.* 2018, Bailey and Hallett 2009) or rejected due to quality control (like insufficient pixels) imposed on the instrument (O'Shea *et al.* 2016). Woods *et al.* (2018) mention the difficulty in accurately classifying particles <30 μm captured using CPI due to its limited resolution. They termed such particles 'quasi-spheroids' even though the category contains droxtals or other habits. Though the larger particles (>30 μm) can be readily classified by habits using direct imaging, the surface texture of the particle cannot be determined. In such cases indirect imaging can be used, however, this requires solving the indirect problem of light scattering to obtain information about the particle shape and surface. It has been shown that using a combination of both direct and indirect imaging, the accuracy of crystal classification can be improved. Future development of direct imaging instruments specifically designed for small crystal detection will also be advantageous.

Key findings from this research can be summarized as follows:

1. On investigating the images taken by the AITS during the ATTREX mission on 5th of March 2015, crystal types like quasi-spheroids (60%), columns (23%), and plates (5%) were found. There was no evidence of aggregates.
2. Over a quarter (26.6%) of the crystal population showed surface roughness. Among these, 12% are crystals with unknown shape. The rest of the crystals are rough surfaced columns, plates, and quasi-spheroids.
3. 83% of the crystals have a diameter $\leq 30\mu\text{m}$, while only 3% had a diameter $\geq 50\mu\text{m}$. These findings are in good agreement with previous studies conducted in TTL cirrus.
4. In the Speckle Analysis method, using a constant Marker value ($=0.6 \times \text{Image}$) suggested in Ulanowski *et al.* (2012) may not work accurately for crystals larger than $30\mu\text{m}$. It was found that 0.75 is the best Marker value as the predictions were comparatively better for the crystal sizes between $10\text{-}100\mu\text{m}$. However, it is recommended to use a marker value between 0.6-0.9 making sure the speckles are of same size by comparing the original image with the binary image created using the morphological reconstruction to get an accurate result.
5. A pilot study using Deep Learning Network which helps in classifying crystals based on their scattering pattern images has been undertaken. On comparing the two pre-trained networks, GoogLeNet and ResNet-50, on average the former predicted correctly with 60%, while the latter predicted correctly with only 32% accuracy. The prediction accuracy for some categories needed improvement and the five categories which the network was trained on seem insufficient in representing the crystal population found in cirrus clouds. Hence, it is recommended to re-train the network after expanding the network's training set by adding more data in each category as well as increasing the number of crystal categories. In this way crystal classification based on images taken by different light scattering instruments can be automated.
6. Overall, this study helped to determine the crystal habits in the $1\text{-}100\mu\text{m}$ size range much more accurately compared to direct imaging. In addition, surface texture of these crystals was analysed.

9. BIBLIOGRAPHY

AMS Glossary of Meteorology (2012) *Droxtal* Available at:

<<https://glossary.ametsoc.org/wiki/Droxtal#:~:text=A%20tiny%20ice%20particle%2C%20about,visibility%20reduction%20in%20ice%20fog>> [Accessed 30 October 2023].

Atlas, R.L. *et al.* (2022) 'Hallett-Mossop Rime splintering dims cumulus clouds over the Southern Ocean: New insight from nudged global storm-resolving simulations', *AGU Advances*, (2). Available at: <https://doi.org/10.1029/2021av000454>.

Baccus, J. (2014) *NASA Global Hawk Ready for 2014 ATTREX Mission*. Available at: <https://www.nasa.gov/centers/dryden/Features/globalhawk_attrex.html> [Accessed 15 February 2022].

Baran, A.J. (2012) 'From the single-scattering properties of ice crystals to climate prediction: A way forward', *Atmospheric Research*, 112, pp.45-69.

Baumgardner, D. *et al.* (2011) 'Airborne instruments to measure atmospheric aerosol particles, clouds and radiation: A cook's tour of mature and emerging technology', *Atmospheric Research*, 102, pp.10-29.

Bohren, C. and Huffman, D. (1998) *Absorption and scattering of light by small particles*. New York: Wiley, pp.3-11.

Boucher, O. *et al.* (2013) 'Clouds and Aerosols. In: Climate Change 2013: The Physical Science Basis. Contribution of Working Group I to the Fifth Assessment Report of the Intergovernmental Panel on Climate Change', *Cambridge University Press*, Cambridge, United Kingdom and New York, USA.

Carlsaw, K.S., Harrison, R.G. and Kirkby, J. (2002) 'Cosmic Rays, clouds, and climate', *Science*, 298(5599), pp. 1732–1737. Available at: <https://doi.org/10.1126/science.1076964>.

Carlsaw, K. (2009) 'Cosmic rays, clouds and climate', *Nature*, 460, 332–333. <https://doi.org/10.1038/460332a>

Chepfer *et al.* (1999) 'Observations of horizontally oriented ice crystals in cirrus clouds with POLDER-1/ADEOS-1', *Journal of Quantitative Spectroscopy and Radiative Transfer*, 63, pp.521-543.

CloudAtlas (2017) *Supplementary features and accessory clouds*. Available at: <<https://cloudatlas.wmo.int/en/supplementary-features-and-accessory-clouds-cirrus.html>> [Accessed 17 May 2023].

Conner, M., 2015 NASA and Partners begin 2015 CAST ATTREX Mission. Available at: <https://www.nasa.gov/centers/armstrong/news/NewsReleases/2015/15-03.html> [Accessed 15 February 2022].

Diedenhoven *et al.* (2020) 'Global Statistics of Ice Microphysical and Optical Properties at Tops of Optically Thick Ice Clouds', *Journal of Geophysical Research: Atmospheres*, 125(6).

Forster, L. and Mayer, B. (2022) 'Ice crystal characterization in cirrus clouds III: retrieval of ice crystal shape and roughness from observations of halo displays', *Atmospheric Chemistry and Physics*, 22, pp.15179-15205.

Fueglistaler, S. *et al.* (2009) 'Tropical tropopause layer', *Rev. Geophys.*, 47, RG1004, doi:10.1029/2008RG000267.

Giannakaki *et al.* (2007) 'Optical and geometrical characteristics of cirrus clouds over a Southern European lidar station', *Atmospheric Chemistry and Physics*, 7, pp. 5519-5530.

Glienke, S. and Mei, F. (2020) *Fast Cloud Droplet Probe (FCDP) Instrument Handbook*. Available at: <https://www.arm.gov/publications/tech_reports/handbooks/doe-sc-arm-tr-238.pdf> [Accessed 15 February 2022].

Guignard *et al.* (2012) 'Bulk microphysical properties of semi-transparent cirrus from AIRS: a six year global climatology and statistical analysis in synergy with geometrical profiling data from CloudSat-CALIPSO', *Atmospheric Chemistry and Physics*, 12, pp. 503-525.

Haralick, R.M., Shanmugam, K. and Dinstein, I. (1973) 'Textural Features for Image Classification', *IEEE Transactions on systems, man, and cybernetics*, 3(6), pp.610-621.

Hecht, E. (2002) *Optics*. San Francisco: Addison Wesley.

Hesse, E. *et al.* (2018) 'Discussion of a physical optics method and its application to absorbing smooth and slightly rough hexagonal prisms', *Journal of Quantitative Spectroscopy and Radiative Transfer*, 218, pp.54-67. DOI: 10.1016/j.jqsrt.2018.06.019

Heymsfield, A. (1975) 'Cirrus Uncinus Generating Cells and the Evolution of Cirriform Clouds. Part I: Aircraft Observations of the Growth of the Ice Phase', *Journal of Atmospheric Sciences*, 32(4), pp.799-808.

Houze, Jr. R. A. (2014) *Cloud Dynamics*. Washington: Elsevier.

Hulst, H. C. (1957) *Light scattering by small particles*. New York: Dover Publications, Inc.

Humpage, N. *et al.* (2018) 'GreenHouse gas Observations of the Stratosphere and Troposphere (GHOST): an airborne shortwave-infrared spectrometer for remote sensing of greenhouse gases', *Atmos. Meas. Tech.*, 11, 5199–5222, Available at: <<https://amt.copernicus.org/articles/11/5199/2018/amt-11-5199-2018.pdf>>

Jensen, E. and Pfister, L. (2004) 'Transport and freeze-drying in the tropical tropopause layer', *Journal of Geophysical Research: Atmospheres*, 109(D2), <https://doi.org/10.1029/2003JD004022>

Jensen, E. *et al.* (2013) *The NASA Airborne Tropical Tropopause Experiment (ATTREX)*. Available at:

https://www.researchgate.net/publication/255171619_The_NASA_Airborne_Tropical_Tropopause_EXperiment_ATTREX

Jensen, E. *et al.* (2017) 'The NASA Airborne Tropical Tropopause Experiment: High-Altitude Aircraft Measurements in the Tropical Western Pacific', *American Meteorological Society*, 98(1), pp.129-143. Available at: <https://journals.ametsoc.org/view/journals/bams/98/1/bams-d-14-00263.1.xml>

Jensen, E. *et al.* (2022) 'Homogeneous Freezing Events Sampled in the Tropical Tropopause Layer', *Journal of Geophysical Research: Atmospheres*, 127, e2022JD036535. Available at: <https://doi.org/10.1029/2022JD036535>

Karcher, B. (2018), 'Formation and radiative forcing of contrail cirrus', *Nature communications*, 9(1824), <https://doi.org/10.1038/s41467-018-04068-0>

Kaye *et al.* (2008), 'Classifying atmospheric ice crystals by spatial light scattering', *Optics Letters*, 33(13), pp.1545-1547.

Kikuchi, K., Kameda, T., Higuchi, K. and Yamashita, A. (2013) 'A global classification of snow crystals, ice crystals, and solid precipitation based on observations from middle latitudes to polar regions', *Atmospheric Research*, 132-133, pp.460-472.

Kokhanovsky, A. (2006) *Light Scattering Reviews*. Chichester: Praxis Publishing Ltd.

Konoshonkin, A. (2017) 'Problem of light scattering by atmospheric ice crystals', *Proc. SPIE 10466, 23rd International Symposium on Atmospheric and Ocean Optics: Atmospheric Physics*, 104662C; <https://doi.org/10.1117/12.2288258>

Kramer *et al.* (1999) 'Homogeneous nucleation rates of supercooled water measured in single levitated microdroplets', *Journal of chemical physics*, 111(14), pp.6521-6527.

Lawson, R. P. *et al.* (2006a) 'The 2D-S (Stereo) Probe: Design and Preliminary Tests of a New Airborne, High-Speed, High-Resolution Particle Imaging Probe', *Journal of atmospheric and oceanic technology*, 23(1), pp.1462-1477. Available at: http://www.specinc.com/sites/default/files/publications/2D-S_Paper.pdf

Lawson, R. P. *et al.* (2006b) 'In Situ Observations of the Microphysical Properties of Wave, Cirrus, and Anvil Clouds. Part II: Cirrus Clouds', *Journal of atmospheric sciences*, 63(12), pp.3186-3203.

Lawson, R. P. *et al.* (2008) 'Aircraft measurements of microphysical properties of subvisible cirrus in the tropical tropopause layer', *Atmospheric Chemistry and Physics*, 8, pp.1609-1620.

Lee, C. and Magono, C. (1966) 'Meteorological Classification of Natural Snow Crystals', *Journal of the Faculty of Science, Hokkaido University. Series 7, Geophysics*, 2(4), pp.321-335.

Lloyd, G. *et al.* (2021) 'In Situ Measurements of Cirrus Clouds on a Global Scale', *Atmosphere*, 12(1), 41, <https://doi.org/10.3390/atmos12010041>

Marsing, A. *et al.* (2023) 'Investigating the radiative effect of Arctic cirrus measured in situ during the winter 2015–2016', *Atmospheric Chemistry and Physics*, 23, pp.587-609.

Mason, B.J. and Ludlam, F.H. (1951) 'The microphysics of clouds', *Reports on Progress in Physics*, 14 (147).

Matlab R2019b, *crossentropy*, Available at:

<https://uk.mathworks.com/help/deeplearning/ref/dlarray.crossentropy.html>

Matlab R2021a, *loss*, Available at:

https://uk.mathworks.com/help/stats/classificationneuralnetwork.loss.html#mw_73dfc39-6209-47aa-9c36-2858c7e77c96

Mishchenko *et al.* (2000) *Light Scattering by Nonspherical Particles*. California: Academic Press.

Mitchell, D. and Finnegan, W. (2009) 'Modification of cirrus clouds to reduce global warming', *Environmental Research Letters*, 4 (045102), pp.1-8. Available at: <https://iopscience.iop.org/article/10.1088/1748-9326/4/4/045102/pdf>

Moilanen, J. and Gritsevich, M. (2022) 'Light scattering by airborne ice crystals – An inventory of atmospheric halos', *Journal of Quantitative Spectroscopy and Radiative Transfer*, 290(108313), pp.1-13

Muinonen, K. *et al.* (1996) 'Light scattering by gaussian random particles: Ray Optics approximation', *Journal of Quantitative Spectroscopy and Radiative Transfer*, 55(5), pp. 577-601. Available at: <https://www.sciencedirect.com/science/article/abs/pii/0022407396000039>

Murray, B.J. *et al.* (2015) 'Trigonal ice crystals in Earth's atmosphere', *American Meteorological Society*, 96(9), pp. 1519–1531.

NASA (2020) *Posidon*. Available at: <<https://espo.nasa.gov/posidon/>> [Accessed 15 February 2022].

NASA (2022) *ATTREX 2DS*. Available at:<<https://espo.nasa.gov/attrex/instrument/2DS>> [Accessed 16 February 2022].

Noel, V. and Sassen, K. (2005) 'Study of Planar Ice Crystal Orientations in Ice Clouds from Scanning Polarization Lidar Observations', *Journal of Applied Meteorology and Climatology*, 44(5), pp. 653–664.

O'Shea *et al.* (2016) 'Airborne observations of the microphysical structure of two contrasting cirrus clouds', *Journal of Geophysical Research: Atmospheres*, 121(22), pp. 13,510-13,536. Available at: <https://agupubs.onlinelibrary.wiley.com/doi/full/10.1002/2016JD025278>.

Przybylo *et al.* (2022) 'Classification of Cloud Particle Imagery from Aircraft Platforms Using Convolutional Neural Networks', *Journal of Atmospheric and Oceanic Technology*, 39(4), pp. 405-424.

Sharma *et al.* (2018) 'An Analysis of Convolutional Neural Networks For Image Classification', *Science Direct Elsevier*, 132, pp.377-384.

Sienfeld, J. and Pandis, S. (1997) *Atmospheric Chemistry and Physics: From Air Pollution to Climate Change*. New Jersey: Wiley–Blackwell.

SPECinc (2011) *Products and services for the atmospheric science community*. Available at: <http://www.specinc.com/sites/default/files/pdfs/SPEC_Brochure_0512_Rev2_.pdf> [Accessed 16 February 2022].

SPECinc (2012) *Hawkeye Combination Cloud Particle Probe*. Available at: <http://www.specinc.com/hawkeye-combination-cloud-particle_probe> [Accessed 16 February 2022].

SPECinc (2013) *Cloud Particle Imager*. Available at: <http://www.specinc.com/sites/default/files/software_and_manuals/CPI_Technical%20Manual_rev1.2_20130226.pdf> [Accessed 14 November 2023].

SPECinc (2019) *Fast Cloud Droplet Probe Technical Manual Rev. 2.0 SPECinc 2019*. Available at:

<http://www.specinc.com/sites/default/files/FCDP_Technical%20Manual_rev2.0_20190710.pdf> [Accessed 15 February 2022].

Spreitzer, E. J., Marschallik, M. P. and Spichtinger, P. (2017) 'Subvisible cirrus clouds – a dynamical system approach', *Nonlinear Processes in Geophysics*, 24(3), pp.307–328, <https://doi.org/10.5194/npg-24-307-2017>.

Stopford, C. *et al.* (2015) 'AllITS: Preliminary light scattering data from Tropical Tropopause Layer cirrus', *Composition and Transport in the Tropical Troposphere and Lower Stratosphere Meeting*, Boulder, Colorado, United States.

Strom, J. *et al.* (1997) 'In Situ Observations of the Microphysical Properties of Young Cirrus Clouds', *Journal of the Atmospheric Sciences*, 54(21), pp. 2542-2553. Available at: https://journals.ametsoc.org/view/journals/atsc/54/21/1520-0469_1997_054_2542_isootm_2.0.co_2.xml

Tape, W. (1994) *Atmospheric Halos*. Washington, DC: American Geophys. Union.

Taylor, L.C. (2016) 'A Beam Tracing Model for Electromagnetic Scattering by Atmospheric Ice Crystals', PhD thesis, University of Hertfordshire.

Tegtmeier, S. *et al.* (2021) 'Chapter 8: Tropical Tropopause Layer', *SPARC Reanalysis Intercomparison Project (S-RIP) Final Report*, pp.307-388. Available at: <https://www.sparc->

climate.org/wp-content/uploads/sites/5/2021/07/08_SRIP_Report_Ch08_EarlyOnlineRelease-2.pdf

Thornberry, T. *et al.* (2017) 'Ice water content-extinction relationships and effective diameter for TTL cirrus derived from in situ measurements during ATTREX 2014', *Journal of Geophysical Research: Atmospheres*, 122(8), pp.4494-4507. Available at:<https://agupubs.onlinelibrary.wiley.com/doi/10.1002/2016JD025948>

Thornton, J. (2016) 'Ice Particle Size and Roughness from Novel Techniques – In Situ Measurements and Validation', PhD thesis, University of Hertfordshire, 2016.

Ulanowski, Z., Hirst, E., Kaye, P. and Greenaway, R. (2012) 'Retrieving the size of particles with rough and complex surfaces from two-dimensional scattering patterns', *Journal of Quantitative Spectroscopy and Radiative Transfer*, 113(18), pp.2457-2464.

Ulanowski, Z. *et al.* (2014) 'Incidence of rough and irregular atmospheric ice particles from small ice detector 3 measurements', *Atmospheric Chemistry and Physics*, 14, pp.1649-1662.

Vincent, L. (1993) 'Morphological Grayscale Reconstruction in Image Analysis: Applications and Efficient Algorithms', *IEEE Transactions on Image Processing*, Vol. 2, No. 2, pp. 176-201.

Wendisch, M., Yang, P. and Pilewskie, P. (2007) 'Effects of ice crystal habit on thermal infrared radiative properties and forcing of cirrus', *Journal of Geophysical Research: Atmospheres*, 112(D8), <https://doi.org/10.1029/2006JD007899>

Westbrook *et al.* (2010) 'Doppler lidar measurements of oriented planar ice crystals falling from supercooled and glaciated layer clouds', *Quarterly Journal of the Royal Meteorological Society*, 136(646), pp.260-276.

Woods, S. *et al.* (2018) 'Microphysical Properties of Tropical Tropopause Layer Cirrus', *Journal of Geophysical Research: Atmospheres*, 123(11), pp.6053-6069. Available at:<https://agupubs.onlinelibrary.wiley.com/doi/full/10.1029/2017JD028068>

Wyser, K. (1998) 'The Effective Radius in Ice Clouds', *Journal of Climate*, 11(7), pp. 1793-1802.

Yang, P. *et al.* (2003) 'Single-scattering properties of droxtals', *Journal of Quantitative Spectroscopy and Radiative Transfer*, 79-80, pp.1159-1169.

Yang, P. *et al.* (2019) 'On the Convergence of Numerical Computations for Both Exact and Approximate Solutions for Electromagnetic Scattering by Nonspherical Dielectric Particles', *Electromagn Waves (Camb)*, 164, pp.27-61.

Zhang, Y., Macke, A. and Albers, F. (1999) 'Effect of crystal size spectrum and crystal shape on stratiform cirrus radiative forcing', *Atmospheric Research*, 52(1-2), pp.59-75.

10. ACRONYMS

2D-S: Two-Dimensional Stereo.

AIITS: Aerosol Ice Interface Transition Spectrometer.

ATTREX: Airborne Tropical TRopopause Experiment.

BT: Beam Tracer.

BTM: Beam Tracing Model.

CAST: Coordinated Airborne Studies in the Tropics.

CCD: Charge-Coupled Device.

CLAHE: Contrast Limited Adaptive Histogram Equalization.

CPI: Cloud Particle Imager.

3V-CPI: Three view Cloud Particle Imager.

DL: Deep Learning.

DLN: Deep Learning Network.

EF: Edge Factor.

FCDP: Fast Cloud Droplet Probe.

GHOST: Green House gas Observations in the Stratosphere and Troposphere.

GLCM: Grey-Level Co-occurrence Matrix.

IN: Ice Nuclei.

LE: Long Edge.

LIDAR: LIght Detection And Ranging.

LR: Long Radius.

NASA: National Aeronautics and Space Administration.

NERC: Natural Environmental Research Council.

NCAR: National Centre for Atmospheric Research.

NOAA: National Oceanic and Atmospheric Administration.

OLR: Outgoing Longwave Radiation.

POSIDON: Pacific Oxidants, Sulfur, Ice, Dehydration, and cONvection Experiment.

PSD: Particle Size Distribution.

PMT: Photo Multiplier Tube.

RMS: Root Mean Square.

SD: Standard Deviation.

SE: Short Edge.

SGDM: Stochastic Gradient Descent with Momentum.

TTL: Tropical Tropopause Layer.

UAV: Unmanned aerial vehicle.

UTC: Co-ordinated Universal Time.

11. APPENDIX

11.1 Speckle Analysis

```
%% Finding the particle size from speckles, based on Ulanowski et al. 2012
```

```
%% For AIITS images:
```

```
ds = imageDatastore('Test Images');%specify the path of file  
I = readimage(ds,2046); %specify the image no. in the  
datastore.
```

```
%Alternatively read the image directly by calling its name: I  
= imread('imagenamename.jpg');  
imshow(I);figure;
```

```
%applying 2 pass median filtering to reduce noise
```

```
MFilter = medfilt2(I);  
MFilter2 = medfilt2(MFilter);  
%montage({I,MFilter2});figure;
```

```
%%For AIITS: Cropping the image
```

```
B= imcrop(MFilter2,[50 19 457 457]);%xtop ytop (left),  
xbottom/width, ybottom/height (right)%cropping the image to  
eliminate background region.
```

```
Xcen = 229.8; Ycen= 229.6; %Image centre
```

```
InnerRadius =75.4180; %Inner angular region corresponding to 8  
degree %though 6degree, artefacts are visible up to 8degree  
OuterRadius =224.4; %Outer angular region corresponding to 25  
degree
```

```
[nrows,ncols]=size(B);
```

```
%Masking the regions other than 8-25 degree; %both 'masking &  
setting the bkgd to 0' and 'image subtraction' does the same.
```

```
[xx, yy] = ndgrid((1:nrows)-Ycen, (1:ncols)-Xcen); % generate  
grid with mask
```

```
mask1 = ((xx.^2 + yy.^2)>OuterRadius^2); % masking region  
outside the circle
```

```
B(mask1) = 0; %0 for black %120 for grey mask %255 white mask  
mask2 = ((xx.^2 + yy.^2)<InnerRadius^2);% masking region  
inside the circle
```

```
B(mask2) = 0; %%values 0-255 can only be assigned, NaN is not  
valid
```

```
imshow(B);figure; %cropped and masked image
```

```
% %To check whether the parameters (inner and outer angular  
region) are right
```

```
% imshow(B);
```

```
% hold on;
```

```

% viscircles([229.8,229.6],75.4180,'Color','b');
% viscircles([229.8,229.6],224.4,'Color','r');
% hold off;

InnerCircularArea =3.14*(InnerRadius^2);
%17859.92=3.14*(75.4180^2)
OuterCircularArea =3.14*(OuterRadius^2);
%158115.8=3.14*(224.4^2)
index=find(B==255);
SatPixels=length(index); %no. of saturated pixels.
numberOfPixels = numel(B);%no.of pixels in matrix B, that is
458x458=209764
[pixelCounts, grayLevels] = imhist(B);%how many no. of pixels
are in each pixel bins/gray levels;

%Greyscale reconstruction
Marker=B*0.75; %original=0.6, but only works for up to
30micron crystals. For 10-100micron crystals 0.75 worked
better during testing with both simulated and AIITS images.
%Test with 0.6 to 0.8 as marker values to find optimum value
according to data.
mask=B;
%imshow(mask);figure; %same as cropped and masked image
imshow(Marker);figure;
if Marker<=mask
J = imreconstruct(Marker,mask);%morphological greyscale
reconstruction
end
imshow(J);figure;
RGMax = imregionalmax(J); %finding regional maxima %binary
image
%imshow(RGMax); figure;

% %%Retrieve speckle properties like speckle area using the
regionprops function.
stats =
regionprops('table',RGMax,'Area','BoundingBox','Centroid','MajorAxisLength','MinorAxisLength');
stats = stats(~(stats.MajorAxisLength > 63),:); %simulated
images inner radius is 63. This condition is inserted so that
it does not detect the inner angular region as a speckle or
any speckle greater than inner angular region size. It also
prevents detecting large, merged speckles.

% %Finding speckle area and particle diameter
MedianSpeckArea=median(stats.Area) %%median of the speckle
area
Ds=2*sqrt(MedianSpeckArea/pi);%Speckle Diameter %A=pi*(d/2)^2
% equivalent circular area
InverseArea=1/MedianSpeckArea;

```

```

ParticleDiam=332.75/Ds %Particle diameter extracting from
AIITS images (Eqn.12 in article); z=491 pixels for AIITS
images. use different z value for other optical scattering
instrument.

% %Quality criterion (Q) check: according to article, Q>0.4
accept, otherwise reject the result
% %However, no correlation between Q value and predicted
particle diameter has been found.
CircularArea=OuterCircularArea-InnerCircularArea;%140255.9;
%Area between 2 rings
SumSpeckArea=sum(stats.Area);
BkgArea=CircularArea-SumSpeckArea;%sum(stats2.Area);
C=(SumSpeckArea/(SumSpeckArea+BkgArea));
Q=4*C*(1-C);

% %to highlight the speckles selected from the reconstructed
image using regionprops.
Cdiameters = median([stats.MajorAxisLength
stats.MinorAxisLength],2);%median(A,2) is a column vector
containing the median value of each row.
centers = stats.Centroid;
radii = Cdiameters/2;
imshow(RGMax);
viscircles(centers,radii);

```

11.2 Combined Roughness

```
%%Computing the roughness of crystals from an image based on
gray-level co-occurrence matrix (GLCM) or gray-level spatial
dependence matrix

clear all;
ds = imageDatastore('Test Images');
I = readimage(ds,1122);

%%Cropping and Masking the image
B1= imcrop(I,[50 19 457 457]);
Xcen = 229.8;
Ycen= 229.6;
InnerRadius =75.4180;
OuterRadius =224.4;
[nrows,ncols]=size(B1);
[xx, yy] = ndgrid((1:nrows)-Ycen, (1:ncols)-Xcen); % generate
grid with mask
mask1 = ((xx.^2 + yy.^2)>OuterRadius^2);%& ((xx.^2 +
yy.^2)>InnerRadius^2); % masking region outside the circle
mask2 = ((xx.^2 + yy.^2)<InnerRadius^2);% masking region
inside the circle
B2=B1.*cast(mask1, class(B1));%mask1&2 are of type 'double',
so converting them into class type 'unit8' as of the image B1
B3=B1.*cast(mask2, class(B1));
MI=B1-B2-B3; %458x458 uint8
%imshow(MI);figure;
index=find(MI==255);
SatPixels=length(index); %no. of saturated pixels

lo=MI(MI~=0);%%% get all non-zero elements in the
MaskedImage (MI)
mean_lo=mean(lo);%mean of non-zero elements
num =size(lo,1);%no. of non-zero elements

MI_10= round(MI*(10/mean_lo)); % scale mean image brightness
to 10 on the 0-255 scale
lo=MI_10(MI_10~=0);
mean_lo=mean(lo);
%imshow(MI_10);

[pixelCounts, grayLevels] = imhist(lo); %%% find the IMAGE
HISTOGRAM of MaskedImage(MI)
rmscheck=rms(pixelCounts); %built-in function to find rms.
meancheck = mean(pixelCounts);
sdcheck=std2(lo); %built-in function to find standard
deviation of a matrix.

%Finding the rms, std and kurtosis manually
rmstest=0;
```

```

sdtest=0;
ktest=0;
rmsc=rms(lo);
for count=1:255
    rmstest = rmstest +pixelCounts(count)*pixelCounts(count);
%summation of (individual intensity frequencies) ^2 %
pixelCounts(count) -> getting values in pixelCounts
    sdtest = sdtest+pixelCounts(count)*(count-rmsc)^2;
%(individual intensity frequencies)x(grey level intensity-mean
grey value)^2
    ktest = ktest + pixelCounts(count)*(count-rmsc)^4;
end

RMS = sqrt(rmstest/256); % Jolic eq. (8) for RMS
SD = sqrt(sdtest/(num-1)); % Jolic eq. (9) for SD
(140303=num-1; 'num' is no. of non-zero elements)
rmsBYsd = RMS/SD;
ktest = ktest/(num-1); % for kurtosis
Kurt=(ktest/SD^4);
log10K = log10(Kurt); % log10(kurtosis)

%converting 'uint8' type to 'single' image
B=im2single(MI);
B(B==0) = NaN; %uint8 can't have NaNs, only double/single
can have NaNs.
imshow(B);

% %if offset is set to 4 directions
offsets= [0 1; -1 1; -1 0; -1 -1];
[glcms,SI] =
graycomatrix(B, 'Offset',offsets, 'Symmetric',true);
SImax= max(SI);
stats = graycoprops(glcms);
AvgContrast=mean(stats.Contrast);
AvgCorrelation=mean(stats.Correlation);
AvgEnergy=mean(stats.Energy);
AvgHomogeneity=mean(stats.Homogeneity);
Combined_Roughness=0.7-((2*AvgEnergy)/3)-
(log10K)/6+rmsBYsd/4000;
%% End of code

```

11.3 Date Time UTC Conversion

Extracting the date and time from individual images or a folder of images, and converts them to UTC.

```
%% Extracting and converting time/UTC since year
1970(individual images)
fileinfo=dir('Flight150305_01_R001_0000253_P.jpg');
[Y,M,D,H,MN,S] = datevec(fileinfo.date); %datevector, a
numeric vector whose six elements represent the year, month,
day, hour, minute, and second components of t.
dt = datestr(fileinfo.date,'HH:MM:SS');
UTC=int64(1425513600+(H*60*60)+(MN*60)+S);

%% Extracting and converting time to UTC since year
1970(folder of images)
b={};
Files=dir('*jpg');
for k=1:length(Files)
FD=Files(k).date;
[Y,M,D,H,MN,S] = datevec(FD);
t =sprintf('%02.f:%02.f:%02.f',H,MN,S);%in 2 digits floating
point form.
b{k,1}=t;
UTC(k,1)=int64(1425513600+(H*60*60)+(MN*60)+S);
k=k+1;
end
```

11.4 Data pre-processing

```
%% Display the centre of BeamStop, inner & outer angular
region of images of AIITS and PPD2 images

%%Part-1: individual images%%
ds = imageDatastore('test images');%creating a datastore for
the folder
I = readimage(ds,3);%image no. 3 in the datastore
imshow(I); figure;
B= imcrop(I,[100 1 581 581]);%xtop ytop (left), xbottom/width,
ybottom/height (right)for PPD2 %%[50 19 457 457] for AIITS
imshow(B);
[BScenter, BSradii] = imfindcircles(B,[20
60], 'ObjectPolarity', 'dark');%detects beam stopper
[INcenter, INradii] = imfindcircles(B,[70
100], 'ObjectPolarity', 'bright', 'Sensitivity',0.96, 'EdgeThresho
ld',0.1);%%circle just outside beam stop %inner circle
[OCcenter, OCradii] = imfindcircles(B,[215
250], 'ObjectPolarity', 'bright', 'Sensitivity',0.99, 'EdgeThresho
ld',0.1);%%outer circle
%%EdgeThreshold 0 means all possible edge points are
considered as a possible point on a circle circumference
%% Matlab recommends the Radius of the circle should be: Rmax
< 3*Rmin and (Rmax - Rmin) < 100
    if (~isempty(BScenter) && ~isempty(OCcenter) &&
~isempty(INcenter)) || (~isempty(BScenter) &&
~isempty(OCcenter) && isempty(INcenter))
        Center = (BScenter+OCcenter)/2;    %BS&OC!=0
    elseif (isempty(BScenter) && ~isempty(OCcenter) &&
~isempty(INcenter)) || (isempty(BScenter) && ~isempty(OCcenter)
&& isempty(INcenter))
        Center = OCcenter; %BS=0,OC!=0
    elseif (~isempty(BScenter) && isempty(OCcenter) &&
~isempty(INcenter)) || (~isempty(BScenter) &&
isempty(OCcenter) && isempty(INcenter))
        Center = BScenter;    %BS!=0,OC=0
    elseif (isempty(OCcenter) && isempty(BScenter) &&
~isempty(INcenter))
        Center = INcenter; %BS=OC=0 %%INC!=0
    else
        Center = [0 0]; %blank images
    end

% viscircles(BScenter, BSradii, 'LineStyle', '--');
% viscircles(INcenter, INradii, 'LineStyle', ':', 'Color', 'b');
% viscircles(OCcenter, OCradii, 'Color', 'r');
% if ~isempty(Center)
% hold on;
% plot(Center(:,1),Center(:,2), 'mx', 'LineWidth',2);%marking x
at centre
```

```

% hold off;
% end

%To check the parameters are correct:
    Center = [290 290];% for PPD2 and[229.8 229.6] for AIITS

    viscircles(Center,
76,'LineStyle',':','Color','b');%InnerCircle=76 for PPD2 and
75.4 for AIITS
    viscircles(Center, 289,'Color','r');%OuterCircle=289 for
PPD2 and 224.4 for AIITS
    hold on;
    plot(Center(:,1),Center(:,2),'mx','LineWidth',2);%marking
x at centre
    hold off;
%%End of code of Part-1

%%Part-2: Folder of images%%
ds = imageDatastore('test images');%creating a datastore for
the folder
nFiles=numel(ds.Files); %find total no. of images
Center=[0 0];
count=0;
for k=1:nFiles
%reading images from the datastore%%
I = readimage(ds,k);
B= imcrop(I,[100 1 581 581]); % [100 1 581 581] for PPD2 and
[50 19 457 457] for AIITS
[FoundCenter, OuterRadius, InnerRadius] = checkCenter(B);
for i=k
x(i,1)=FoundCenter(1,1);%row 1 col 1; x co-ordinate
x(i,2)=FoundCenter(1,2);%row 1 col 2; y co-ordinate
ir(i,1)=InnerRadius(1,1);
or(i,1)=OuterRadius(1,1);
end

%writing the values into a file
%writematrix(x,'PPD2_Centre_CroppedImage.txt','Delimiter','tab
');
writematrix(ir,'PPD2_InnerRadius_CroppedImage.txt','Delimiter'
,'tab');
%writematrix(or,'OuterRadius_CroppedImage.txt','Delimiter','ta
b');
k=k+1;
count=count+1;
end

%%defining the function%%
function [FoundCenter, OuterRadius, InnerRadius] =
checkCenter(B)

```

```

[BScenter, BSradii] = imfindcircles(B,[20
60], 'ObjectPolarity', 'dark'); %detects beam stopper
[INcenter, INradii] = imfindcircles(B,[70
100], 'ObjectPolarity', 'bright', 'Sensitivity', 0.96, 'EdgeThresho
ld', 0.1); %%circle just outside beam stop %inner circle
[OCcenter, OCradii] = imfindcircles(B,[215
250], 'ObjectPolarity', 'bright', 'Sensitivity', 0.99, 'EdgeThresho
ld', 0.1); %%outer circle

    if (~isempty(BScenter) && ~isempty(OCcenter) &&
~isempty(INcenter)) || (~isempty(BScenter) &&
~isempty(OCcenter) && isempty(INcenter))
        Center = (BScenter+OCcenter)/2;    %BS&OC!=0
    elseif (isempty(BScenter) && ~isempty(OCcenter) &&
~isempty(INcenter)) || (isempty(BScenter) && ~isempty(OCcenter)
&& isempty(INcenter))
        Center = OCcenter; %BS=0, OC!=0
    elseif (~isempty(BScenter) && isempty(OCcenter) &&
~isempty(INcenter)) || (~isempty(BScenter) &&
isempty(OCcenter) && isempty(INcenter))
        Center = BScenter;    %BS!=0, OC=0
    elseif (isempty(OCcenter) && isempty(BScenter) &&
~isempty(INcenter))
        Center = [0 0]; %BS=OC=0 %%we dont need INcentre as
the artefact is slightly off towards left.
    else
        Center = [0 0]; %blank images
    end

    FoundCenter = Center;

    if ~isempty(OCradii)
        OuterRadius = OCradii;
    elseif isempty(OCradii)
        OuterRadius = 0;
    end

    if ~isempty(INradii)
        InnerRadius = INradii;
    elseif isempty(INradii)
        InnerRadius = 0;
    end

    if INradii<80    %%anything greater than 80 is likely to be
in a region other than around beamstop.
        InnerRadius = INradii;
    else
        InnerRadius = 0;
    end
end
%%End of Part-2 code.

```

```
%%Part-3: Finding the mean values
A = readmatrix('OuterRadius_Image.txt');
MeanOuterRadius = mean(nonzeros(A));
%End of Part-3 code.
```

11.5 Deep Learning Network

```
%%% Designing a Trained Network
%% PART-1: USING SUPERVISED LEARNING, ASSIGN THE FOLDER NAMES
AS CRYSTAL CATEGORIES. (SEE SECTION 7.3.3)
ds = imageDatastore("Crystal Category
14","IncludeSubfolders",true,"LabelSource","foldernames");
auds = augmentedImageDatastore([224
224],ds,"ColorPreprocessing","gray2rgb");
save trainedNetwork_1; %GoogLeNet
GoogLeNet=trainedNetwork_1; %rename the trained network
save GoogLeNet;
%% END OF CODE FOR PART-1.

%% PART-2: TO TEST INDIVIDUAL IMAGES
load GoogLeNet;
net=GoogLeNet;%using GoogleNet, 5 categories:plate,columns,
rounded, blank & patterned, to work on masked & cropped image
opengl('save','software');

%section for AIITS images
% Xcen=229.8;
% Ycen=229.6;
% OCradii=224.4;
% ICradii=75.4;
% a = imread('Flight150305_01_R001_0000006_P.jpg');
% C= imcrop(a,[50 19 457 457]);%xtop ytop (left),
xbottom/width, ybottom/height (right)55 16 450 450 or [54 18
456 456] or [50 19 457 457]

%section for PPD2 images
Xcen=290; % Image centre.
Ycen=290; %Image centre.
OCradii=289; %Outer angular region.
ICradii=76; %Inner angular region.
a = imread('2.bmp');
C= imcrop(a,[100 1 581 581]);%xtop ytop (left), xbottom/width,
ybottom/height (right)

%%%generating circular mask%% for both types of images
[nrows,ncols]=size(C);
[xx, yy] = ndgrid((1:nrows)-Ycen, (1:ncols)-Xcen); % generate
grid with mask
mask = ((xx.^2 + yy.^2)>OCradii^2); % masking region outside
the circle %equation of circular mask
C(mask) = 255;
mask2 = ((xx.^2 + yy.^2)<ICradii^2);% masking region inside
the circle
```

```

C(mask2) = 255; %%values 0-255 can only be assigned, NaN is
not valid.
figure('Name','Image versus Prediction','NumberTitle','off');
subplot(1,2,1);
LeftAx = subplot(1,2,1);
imshow(C);
title(LeftAx,'PPD2 image'); %%change the title according to
image type.

auds1 = augmentedImageDatastore([224
224],C,"ColorPreprocessing","gray2rgb");%converting grayscale
to RGB.
[pred,scores] = classify(net,auds1);%predicted category in
pred and the prediction score/value (0-1)in scores.
[~,idx] = sort(scores,'descend');%to show the highest probable
category first. sorting the scores in descending order along
with their index.
idx = idx(5:-1:1);%change the no. 5 to the total number of
outputs/categories.
classNamesTop = net.Layers(end).ClassNames(idx);%extracting
category names from the final layer of the Deep Network.
scoresTop = scores(idx);
subplot(1,2,2);
barh(scoresTop); %horizontal bar chart of the prediction
scores
%barchart properties
xlim([0 1]);
title('Top 5 Predictions');
xlabel('Probability');
yticklabels(classNamesTop);%category names
ytickangle(45);%to show the labels in an angle (otherwise the
labels overlap)
%% END OF CODE FOR PART-2.

%%PART-3: TO TEST IMAGE DATABASE
f = imageDatastore("Test images"); %check files are reading
sequentially
nFiles=numel(f.Files); %find total no. of images
count=0;

% %%for AIITS images
% Xcen=229.8;
% Ycen=229.6;
% OCradii=224.4;
% ICradii=75.4;

%%for PPD2 images
Xcen=290;
Ycen=290;
OCradii=289;

```

```

ICradii=76;

%%%for all images
load GoogLeNet;
net = GoogLeNet;
for j=1:nFiles
a = readimage(f,j);%reading images from the datastore%%

%Image cropping for AIITS/PPD2 images
%C= imcrop(a,[50 19 457 457]);% for AIITS images; xtop ytop
(left), xbottom/width, ybottom/height (right)
C= imcrop(a,[100 1 581 581]); % for PPD2 images;

%%%generating circular mask%% for both image types
[nrows,ncols]=size(C);
[xx, yy] = ndgrid((1:nrows)-Ycen, (1:ncols)-Xcen); % generate
grid with mask
mask = ((xx.^2 + yy.^2)>OCradii^2); % masking region outside
the circle
C(mask) = 255;
mask2 = ((xx.^2 + yy.^2)<ICradii^2);% masking region inside
the circle
C(mask2) = 255; %%values 0-255 can only be assigned, NaN is
not valid

ImD = augmentedImageDatastore([224
224],C, "ColorPreprocessing", "gray2rgb");
[pred,scores] = classify(net,ImD);
    for i=j
        s(i,1)=scores(1,1);%row 1 col 1;
        s(i,2)=scores(1,2);
        s(i,3)=scores(1,3);
        s(i,4)=scores(1,4);
        s(i,5)=scores(1,5);
        p(i,1)=pred(1,1);
    end

%%if using Excel file, write only 1 file at a time to avoid
crashing
writematrix(s,'testImages_Scores_DLN_GoogLeNet.txt','Delimite
r','tab'); %to view scores
writematrix(p,'testDataset_PPD2_GoogLeNet.xlsx'); %to view
predicted category.

j=j+1;
count=count+1;
end

```

```

summary(p); % summary of results (number of crystals in each
categories)
%% END OF CODE FOR PART-3.

%%Part-4: to display the CONFUSION MATRIX
data1= readcell('test images PPD2.xlsx','Range','A1:A140'); %
specify the data range of manual classification in the Excel
sheet.
data2= readcell('test images PPD2.xlsx','Range','C1:C140'); %
specify the data range of predicted classification in the
Excel sheet.
cm = confusionchart(data1,data2,'Title','Confusion Matrix -
ResNet','RowSummary','row-normalized');%true class vs
predicted class
%% END OF CODE FOR PART-4.

```

11.6 Poster

The following Poster was presented during the SPECS (School of Physics, Engineering and Computer Science) conference conducted at the University of Hertfordshire on 13th June 2023. The Poster outlines the summary of research undertaken in this thesis.



School of Physics,
Engineering and
Computer Science

SPECS research conference
13th June 2023

Modelling and Analysis of ice crystals in Tropical Tropopause clouds based on in-situ light scattering patterns

Elizabeth Reeja Mathen^{1*},
*Dr Evelyn Hesse*¹,
*Dr Richard S. Greenaway*¹,
*Dr Anthony J. Baran*²

¹ University of Hertfordshire, Hatfield, UK
² Met Office, UK
*em14abz@herts.ac.uk

"Clouds and aerosols continue to contribute the largest uncertainty to estimates and interpretations of the Earth's changing energy budget.... The role of thin cirrus clouds for cloud feedback is not well understood and remains a source of possible systematic bias." [1] Predicting the radiative properties of cirrus is generally challenging, since cirrus is an ice cloud composed of crystals with a wide range of size, shape and complexity. Limitation of imaging instruments and scarcity of observational data makes it even more challenging.

Research objective

- Analyze the scattering patterns of ice crystals in the Tropical Tropopause Layer (TTL) cirrus clouds.
- Find the microphysical properties like shape and size distributions, and surface properties of these ice crystals.

Outcome

- Better understanding of physical and scattering properties of ice crystals in TTL.
- Their impact on the radiative balance can be estimated [2].
- Results can be used in climate model simulations and predict climate more accurately.



Fig. 1. Global Hawk carrying ATTREX instruments [3]

Data

- The study was part of NASA's Airborne Tropical Tropopause Experiment (ATTREX) 2011-2015, to investigate the physical and chemical processes in the TTL.
- The data/images were taken during one such study on 5th March 2015 using Global Hawk (Fig. 1) over the Eastern Pacific Ocean at an altitude of 15-16km.
- A collection of 2426 2D light scattering patterns (greyscale images of 512x640 pixels) captured by the Aerosol Ice Interface Transition Spectrometer (AIITS) [4] (Fig. 2), which detects particles of size 1-100µm at the wavelength of 532nm.
- The scattering pattern image covers 6°-25° of the forward scattering hemisphere.



Fig. 2. AIITS [4]

Method

- Solve the inverse scattering problem by a combination of analysis and computational modelling techniques.
- Identify crystal morphology by analyzing the features in the 2D light scattering patterns as they vary with the ice crystal geometry. For example, the simulated patterns of a rough column crystal has both scattering arcs and speckle-like features, whereas speckles will be absent in a smooth column's case.
- Generate model crystals using specific codes for light scattering computations.
- Simulate the scattering data of the model crystals using Beam Tracing Models (BTM) [5][6] based on physical optics (examples in Fig. 3).
- By successive testing and further analysis, the crystal sizes are estimated. For rough crystals, the size is estimated using Speckle Analysis method [7], that is, extracting the regional maxima (speckles) from reconstructed greyscale image based on mask and marker values. Their roughness is measured using Combined Roughness scale [8].

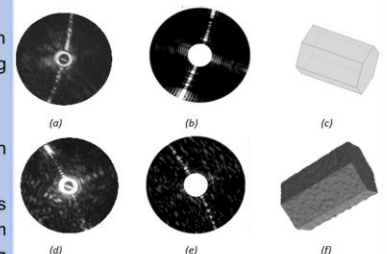


Fig. 3. (a) and (d) Two AIITS images with beam-stop in the centre; (b) and (e) respective scattering patterns simulated by BTM [5][6] from the corresponding model crystals of (c) smooth and (f) rough hexagonal column in specific orientations, shown in top and bottom row respectively.

Results and conclusion

TTL ice crystals have been classified by analyzing their scattering patterns. Only 876 out of 2426 images were used; the remaining ones are either blank or only contain artefacts and hence discarded. The crystal classification based on their size, shape, and surface texture is shown in Fig. 4 (statistics in Table 1). Results show that around 60% of the crystals (with <50 µm diameter) are quasi-spheroids and 83% crystals have crystal diameter <30 µm. This agrees with the results from 2014 ATTREX sampling, over the TTL cirrus of the Western Pacific [9], "Observed ice particles were predominantly small (<30 µm diameter) and quasi-spheroidal in shape."

Fig. 4. The crystal habit and size distribution

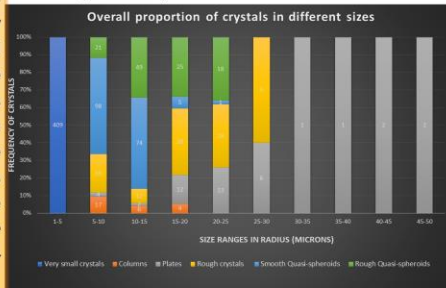


Table 1. Classification of AIITS scattering patterns (images) into different crystal types and textures.

Crystal Categories	Count	Percentage
Very small crystals (quasi-spheroids) (<10µm diameter)	237	27.05%
Columns (column-like)	172	19.63%
Columns	27	3.1%
Plates	43	4.9%
Rough crystals	106	12.1%
Quasi-spheroids	291	33.2%
Total	876	100%

REFERENCES

[1] Boucher O et al. (2013) 'Clouds and Aerosols. In: Climate Change 2013. Contribution of Working Group I to the Fifth Assessment Report of the Intergovernmental Panel on Climate Change'. Cambridge University Press, Cambridge, UK.
[2] Baran, A.J. (2012) 'From the single-scattering properties of ice crystals to climate prediction: A way forward'. Atmospheric Research, 112, pp.45-69.
[3] NASA. (2014) NASA Global Hawk Ready for 2014 ATTREX Mission. [online] Available at: <https://www.nasa.gov/centers/dryden/Features/globalhawk_attrex.html>
[4] Hirst, E., Stopford, C., Kaye, P.H., Greenaway, R.S., Dorsey, J.D. (2013) 'The Aerosol Ice Interface Transition Spectrometer - A new particle phase'. ATTREX Science Meeting, Boulder, USA.
[5] Taylor, L.C. (2016) 'A Beam Tracing Model for Electromagnetic Scattering by Atmospheric Ice Crystals'. PhD thesis, University of Hertfordshire.

[6] Hesse, E. et al. (2018) 'Discussion of a physical optics method and its application to absorbing smooth and slightly rough hexagonal prisms'. Journal of Quantitative Spectroscopy and Radiative Transfer, 218, pp.54-67.
[7] Ulanowski, Z., Hirst, E., Kaye, P. and Greenaway, R. (2012) 'Retrieving the size of particles with rough and complex surfaces from two-dimensional scattering patterns'. Journal of Quantitative Spectroscopy and Radiative Transfer, 113(18), pp.2457-2464.
[8] Ulanowski, Z. et al. (2014) 'Incidence of rough and irregular atmospheric ice particles from small ice detector. 3 measurements'. Atmospheric Chemistry and Physics, 14, pp.1649-1662.
[9] Woods, S. et al. (2018) 'Microphysical Properties of Tropical Tropopause Layer Cirrus'. Journal of Geophysical Research: Atmospheres, 123(11), pp.6053-6069.